Università di Roma *"Sapienza"*

FACOLTA DI SCIENZE MATEMATICHE FISICHE E NATURALI ‘

DOTTORATO DI RICERCA IN
MATEMATICA APPLICATA
XXXIII CICLO

2d viscous flow studied using vortex particle methods

Giannopoulou Ourania

Advisors:
Dr. Danilo Durante
Dr. Andrea Colagrossi

Tutor:
Prof. Gabriella Puppo

31 October 2020

ABSTRACT

Vortex particle methods are alternative methods to Eulerian approaches for the solution of the incompressible Navier-Stokes equations in vorticity-velocity variables. They are characterized by the inherent ability to adapt to the flow due to their Lagrangian formulation for the advection and additionally by the decoupling of the pressure from the momentum equation. In this work, we study these methods using the Lagrangian vortex particle method Diffused Vortex Hydrodynamics that uses the operator splitting in time of Chorin. Numerical results are obtained for problems containing solid boundaries in the domain for different test cases. We compare the results with a finite volume solver that discretizes the velocity-pressure formulation of Navier-Stokes and uses artificial compressibility to evolve the solution in time, also introduced by Chorin. The comparison is obtained based on local and global derived quantities. Finally, an application of the method to a physical study is presented regarding the flow past an elliptical cylinder.

RINGRAZIAMENTI

Upon the completion of my doctorate studies at the program "Vito Volterra", in Applied Mathematics of the Sapienza university of Rome at the department of Mathematics "Guido Castelnuovo", I would like to thank the people who contributed to my graduation.

Dr. Colagrossi A., of the CNR-INM, for the opportunity he gave me to be under his supervision for this thesis, for his patient work, help and valuable advices without which the accomplishment of this work would have been impossible. I would like to equally thank Dr. Durante D., of the CNR-INM for his excellent supervision during the second half of my studies and his continuous support especially during its final stages. Finally I would like to thank Prof. DiMascio A. that also contributed to this work.

I would like to thank my tutors during the years of my doctorate studies: Prof. Mascia C. as well as Prof. Puppo G. who both guided me through the writing of this thesis through valuable discussions.

I would like to thank the numerical modeling group of the department which provided the weekly seminars on diverse topics in numerical methods and especially the head of the group Prof. Falcone M.

A sincere thank you to all the people I had the opportunity to meet at CNR-INM but especially to: Alessia, Andrea, Chiara, Matteo & Salvatore.

I would like to thank my friends who supported me at different stages of this long process: Christina, Ippoliti, Marianna, Dimitris.

Finally, I would like thank my family without which the completion of this doctorate would have been impossible.

CONTENTS

I VORTEX PARTICLE METHODS

II DETAILS OF THE NUMERICAL METHODS

III VALIDATIONS AND PHYSICAL INVESTIGATIONS

1

INTRODUCTION TO THE THESIS

1.1 MOTIVATION AND BACKGROUND

Vortex Particle Methods (VPMs) are Lagrangian methods for the numerical simulation of unsteady viscous flow problems. The governing equations are the Navier Stokes Equations (NSEs) in vorticity–velocity formulation, solved by the operator splitting algorithm of Chorin introduced in Chorin (1973). For the numerical integration of the governing equation, the vorticity field is discretized with vortex particles that evolve by means of a two-step algorithm, consisting of an inviscid step, where the flow is governed by Euler's equations, followed by a diffusion step, governed by the heat equation.

The vorticity–velocity formulation, in combination with the use of Lagrangian advection of particles, possesses several advantages over the primitive variable formulation such as:

- Being vorticity the primary variable has the consequence that only the vortical regions of the computational domain are being discretized.
- The pressure is eliminated from the governing equations and therefore no solution of a Poisson equation is required.
- The Lagrangian advection step using particles removes numerical dissipation, typical of meshbased Eulerian approaches.
- The advection time-step is not limited by the Courant - Friedrichs - Lewy (CFL) condition for stability.
- For external flows, using an integral representation for the velocity field, boundary conditions at infinity are exactly satisfied.

The above characteristics render vortex methods an invaluable alternative to the mesh-based methods for performing numerical simulations.

The goal of the thesis is to study a specific vortex particle method, the method Diffused Vortex Hydrodynamics (DVH) introduced in Rossi et al. (2015a), verify its results by comparison through detailed simulations with a grid-based numerical solver based on Finite Volumes and finally leverage its multiple advantages to conduct an application to a physical study, that of the flow past an elliptical cylinder.

Regarding the vortex method DVH, its distinctive characteristic is the way in which the treatment of Lagrangian distortion is performed. This a well-known problem for all vortex methods that is caused by the depletion or clustering of the particles due to their inherent ability to adapt to the flow field. Early convergence proofs for Euler equations in the absence of boundaries, (Hald and Del Prete (1978), Hald (1979), Hald (1986), Perlman (1985)) showed that it is required that the particles are overlapping sufficiently in order for these methods to converge. A way to circumvent this problem is particle redistribution after the advection step on a regular mesh where the solution is interpolated. The introduction of a mesh also allows the solution of the Poisson equation, that links velocity and vorticity, using a mesh-based solver. However, the interpolation of quantities from the mesh to the particle nodes introduces numerical dissipation as explained in Barba et al. (2003). In the method DVH the problem is addressed by introducing a Regular Point Distribution (RPD) in the diffusion process. The RPD consists of points with no topological connection and the diffusion step is performed by diffusing the circulation of the vortex particles on the points of this RPD. After the end of the diffusion step the points of the RPD become the new vortex particles that are advected in the subsequent advection step. This procedure has the advantage of resulting in a completely meshless method removing thus the need for introduction of a mesh and the subsequent numerical diffusion following it.

Regarding the verification of the method, in this work a comparison with a well-established finite volume solver is performed that solves the velocity - pressure formulation. Two of the widely used methods for solving incompressible Navier-Stokes equations in hydrodynamic problems are: The projection method and the artificial-compressibility method both introduced by Chorin in Chorin (1968) and Chorin (1967) respectively. The projection method uses operator splitting in time where the incompressibility is enforced solving a Poisson for the pressure at the second sub-step. Instead, the artificial compressibility the pressure is coupled to the velocity through the continuity equation using a pseudo-derivative in time for the pressure. In this work all the verifications presented are performed using the latter method with the approach introduced by Broglia and Durante (2018).

After the verification of the Lagrangian vortex method DVH, an application to a physical study is presented. The motivations for using DVH specifically for the physical studies are multiple:

- First, due to the particle-based formulation, high resolutions are computationally feasible for 2d problems and permit detailed description of the near body but most importantly of the far body vorticity dynamics. This is in contrast to grid-based methods where the far field needs a very high number of cells in order to resolve adequately the vortex structures and at a reasonable computational cost.

- Secondly, it allows for Direct Numerical Simulation, since it does not use turbulence or sub-grid scale models.

- Thirdly, the discretization of only the vortical part of the flow field does not require the detailed pre-processing needed for grid - based methods.

All of the above render DVH particularly attractive to perform the long-time simulations needed for the work presented here.

The present physical study deals with the identification of the different regimes of the flow field (steady, periodic, chaotic) when three parameters are varied, namely the Reynolds number, the aspect ratio of the ellipse and its angle of incidence with the free-stream velocity of the fluid. One of the most severe issues of this study is the necessity to perform a large number of detailed simulations for long enough time in order to be confident with the identification of the different regimes. As it will be shown transients can last for considerable amount of simulation time especially when the system is near the onset of a bifurcation. To this end the above advantages for using DVH are especially desirable.

The choice of an elliptical cylinder is motivated by the fact that in contrast to circular cylinders which have been broadly researched, studies on elliptical cylinders are much less abundant. However, it is anticipated that different flow characteristics will be present given the plethora of the varying parameters. Most of the existing studies describing the dynamics of this kind of flow have been conducted mainly in the low Reynolds regime in part because of the high computational cost as for example in the numerical studies of Shintani et al. (1983) using the method of matched asymptotic expansions in order the critical Reynolds range for the transition from the steady to the unsteady regime, in Park et al. (1989) to investigate the effect of the angle of incidence on the steady regime and also in the work of Johnson et al. (2004) to study the effect of aspect ratio on the same regime.

In the framework of dynamical systems one of the pioneering works was that of Pulliam and Vastano (1993) where the transition to chaos for flow past an airfoil at fixed angle of incidence was studied while increasing the Reynolds resulting in a period doubling bifurcation to chaos. In Jackson (1987) the transition from steady to periodic solution was found for an elliptical cylinder to be established through a Hopf bifurcation for fixed Reynolds number and varying angle of attack. Studies performed recently by Kurtulus (2015), Kurtulus (2016), show the impact of thickness and angle of incidence on the wake topology for fixed Reynolds and varying angle of incidence in the case of airfoils, concluding with the existence of five different configuration for the vorticity referred to as modes. The transition among the different modes was also found to manifest through period doubling and quadrupling bifurcations before entering the chaotic regime. In the work of Rossi et al. (2018) the same modes were identified for a thinner airfoil and fixed incidence however with only period doubling bifurcations occurring while in Durante et al. (2020b) the same airfoil for fixed Reynolds and varying angle of attack showed that the transition occurs through period tripling, period-6 and period-12 bifurcations, documented for the first time.

1.2 STRUCTURE OF THE THESIS

The thesis is decomposed into three main parts. In the first part, chapter 2 presents a brief historical reference to the evolution of Vortex Particle Methods. The following chapter 3 is a detailed presentation on the state of the art of vortex methods.

The second part deals with the solution methods for the numerical approximation of incompressible Navier-Stokes equations used in this work. Both are developed by Chorin. In chapter 5, we describe the method DVH used in the simulations. This method is based on operator splitting and solves the vorticity-velocity formulation of equations. In chapter 6, numerical details are presented. In chapter 7, the velocity - pressure formulation is introduced along with the description of two popular methods for its resolution, both introduced from Chorin: the projection method introduced in Chorin (1968) and of the artificial compressibility method introduced in Chorin (1967). For the numerical simulation a finite volume solver based on artificial compressibility is used and here the approach of Broglia and Durante (2018) is used.

The third part contains verifications, numerical and physical investigations. In chapter 8, comparison of results obtained from DVH are performed with the FVM. Results are obtained for different benchmark tests regarding a cylinder in an accelerating current, flow past an elliptical and a triangular cylinder for different Reynolds numbers. The chapter 9 deals with the application of the vortex method DVH to the physical study of flow past an elliptical cylinder. The goal is to study the different regimes arising from the incompressible planar viscous flow past an elliptical cylinder. The effect of the aspect ratio and of the angle of attack on the onset of the regimes is investigated and the route to chaos is established through different tools such as the Fourier spectra, phase space maps and Poincaré sections. Long time simulations have been carried out in order to guarantee that every single regime is attained.

1.3 RESULTS

In this part, a verification and application of the vortex method DVH is presented. The results of this work are published in Giannopoulou et al. (2019a), Giannopoulou et al. (2019b) and submitted in Durante et al. (2020a).

Verification

In this part of the thesis, the numerical behavior of the vortex method DVH was carefully investigated for planar flow around three geometries, with varying Reynolds number. All the test cases considered are unsteady and are all characterized by increased complexity. The comparison shows that there is overall agreement between the two methods in terms of both global and local quantities such as the vorticity fields and the forces respectively.

Regarding the case of the circular cylinder in an unsteady current, the Reynolds number varies from 100 up to 4000. Results show that the physical characteristics of the flow are very well captured by the DVH method with respect to the boundary layer thickness, the separation and the thinner vorticity structures developing with increasing Reynolds.

For the case of flow past an elliptical cylinder, which will be used also for the physical study, the configuration is with the cylinder being inclined to the free - stream (inflow) at angle of incidence 20° while the aspect ratio is $b/a = 0.40$. The Reynolds studied are Re=200, 500, 1000. For all the cases the flow is unsteady and the flow characteristics are captured for all the values of Reynolds. The accuracy of the method is studied in terms of the recorded forces and compared to that of the finite volume method with very satisfactory results in the region close to the body which is the most important region for the evaluation of forces. Differences are noted regarding the agreement between the vorticity field obtained by the two solvers far from the body for the finite volume method. This difference is explained by the fact that the finite volume solver uses a coarser grid in this region.

Finally the case of triangular cylinder is studied through a series of simulations for Reynolds numbers Re=100 and 1000. The presence of sharp edges produces high spatial gradients and requires also a careful numerical treatment. For Re=100 the comparison with the finite volume solver is in a very good agreement in the overall quantities measured while for Re=1000 small differences are noticed. The accuracy assessment for the DVH shows that very high resolutions are required in order to obtain convergence of the forces. However, also the finite volume method exhibits the same behaviour. For both solvers this behaviour might be attributed to the singularity present at the wedge tip. Specifically for the vortex method an additional factor could be the viscous splitting algorithm that is first order in time. A further investigation about this aspect will be the subject of future research.

Application to a physical study

After the verification of the method, an application to a physical study is presented for the flow past a elliptical cylinder. The goal is to characterize the various regimes of the flow as the latter passes from a steady to a chaotic condition. The effect of the aspect ratio and of the angle of attack on the onset of the regimes is investigated and the route to chaoticity using tools from classical dynamical systems is obtained. The parameter space being too large for being covered completely, here seven test cases are selected totaling 121 simulations.

The strategy is to obtain quantities of interest from numerical simulations such as vorticity fields, lift, drag and pressure coefficients, then use as tools the power-spectra phase-space & Poincaré maps of the lift time-series, along with the evaluation the maximum Lyapunov exponents to extract information about the dynamics of the underlying flow and establish the sequence of transition from periodicity to chaos.

A deep investigation on the periodic regimes revealed several possible conditions in terms of lift time signal: monochromatic, non-monochromatic and sub-harmonics regimes. In addition, a quasi-periodic time behaviour with an underlying chaotic amplitude modulation was also found in the test matrices performed. Increasing the Reynolds number the periodic regimes are lost giving the place to a chaotic behaviour.

With respect to the aspect ratio, for small value corresponding to the case of a thin ellipse, the onset of period doubling bifurcations was discovered. Increasing the aspect ratio, the thickening of the ellipse is found to make this mechanism less dramatic. Furthermore, in some scenario, time bifurcations before the onset of the regime condition were found.

Significant differences between thin and thick ellipse chaotic regimes were documented and the presence of a pink noise behaviour of the lift time signal in the thin case was discovered.

Another important aspect of the present analysis has been the investigation in terms of the vorticity flow fields and it has been connected to the time behaviour of the lift force, where meaningful.

The present investigation may be extended to the analysis at higher Reynolds numbers at different thickness and different angles of attack. Indeed, at Re of order 10^5 turbulent transition of the boundary layer is expected affecting drag and lift forces as it is shown in Durante et al. (2017) for the case of a circular cylinder.

Part I

VORTEX PARTICLE METHODS

2

A BRIEF HISTORY OF VORTEX METHODS

The origin of Vortex Methods can be attributed to Rosenhead (1931) who driven by the problem of the evolution of a vortex sheet, performed the first simulations on the study of the Kelvin - Helmholtz instability. Discretizing a line of vorticity into segments and placing point particles on their center equal to their carrying vorticity, he performed the calculations by hand and the result was that vortex sheets indeed roll up. The problem was studied also later with the numerical simulations performed on computers. By increasing the number of vortices in order to have increased accuracy it was revealed that the solution was not converging and this was accounted to the singular nature of point vortices (Birkhoff and Fisher, 1959).

1970s

The present status of *viscous* vortex methods was initiated by Chorin's seminal work during 1970s who introduced the Random Vortex Method together with the viscous splitting algorithm (Chorin, 1973) that treated the viscous part in a non-deterministic way. Chorin removed the singularity problem by using blobs instead of point vortices.

An important addition to the viscous schemes was the Vortex in Cell method (Christiansen, 1973). Inspired by the particle-in-cell method used in plasma physics, the vortex particles were projected on a grid raising the possibility to solve the Poisson equation for the velocity on it. The use of a mesh based solver made vortex methods capable of handling very large numbers of particles even though it compromised their meshfree origins. Motivated by the treatment of boundary conditions in *viscous* vortex methods for flows containing solid boundaries, Chorin studied the generation of wall vorticity using vortex sheets (Chorin, 1978) which has led to a proper mechanism to generate and diffuse vorticity from the boundary of the body.

The upcoming interest in vortex methods was reflected on the numerous results concerning their numerical analysis. This was initiated with the work of (Hald and Del Prete, 1978) who proved the convergence of two dimensional *inviscid* vortex methods with no boundaries to Euler's equations for the random vortex method of Chorin. The result was that vortex methods converge depending on the smoothness of the flow and the choice of the cut-off functions. More specifically, the ratio of the blob size to the particle spacing had to be large enough, meaning that the blobs had to overlap sufficiently. As a conclusion in the convergence study of vortex methods the errors are introduced in two ways: First from the smoothing that is introduced to the velocity kernel and secondly from the way of discretizing the vorticity field using particles. This was one of the main reasons for the delay of vortex methods' acceptance until the introduction from Koumoutsakos (1993) of remeshed vortex methods.

1980s

In 1980s, the notion of vortex filaments was introduced as an alternative discretization to the vorticity field (Leonard, 1980). Additional convergence results were added this period were Beale and Majda (1981) proved that the rate of convergence of Chorin's viscous splitting algorithm to the Navier-Stokes equations is first order in time. Moreover, it was shown that using symmetric Strang splitting, the convergence rate can be improved to second order. Finally, in Beale and Majda (1982b), Beale and Majda (1985) it was demonstrated that for the case of no solid boundaries, for the Euler case and for smooth flows it is possible to obtain arbitrary order of accuracy both in 3D and 2D by appropriate selection of the smoothing function used to approximate the delta function. Given this function then the order of convergence to the Euler equation depends solely on the regularity of the flow. To this end, they introduced specific algebraic kernels (smoothing functions) that could provide this high order of accuracy. Finally these kernels should satisfy moment conditions, being smooth and rapidly decreasing to be consistent in the approximation of the Biot-Savart.

A major contribution to vortex methods was towards their numerical implementation with the advent of fast summation algorithms. With the introduction of the treecodes (Barnes and Hut, 1986) and the Fast Multipole Method (Greengard and Rokhlin, 1987) the complexity of evaluating the Biot-Savart integral was reduced from $O(N^2)$ to $O(N \log N)$ and $O(N)$ respectively. The resolution of the problem for the computational cost made possible simulating billion of particles and made vortex methods competitive with respect to Eulerian - Lagrangian solvers (e.g. Vortex in Cell) that were based on a Poisson solver. A new addition to the viscous schemes was introduced in (Mas-Gallic and Raviart, 1987), the Particle Strength Exchange (PSE) method.

1990s-onwards

Many other deterministic viscous schemes were added some of which will be described in the next chapter. Among them Fishelov's scheme (Fishelov, 1990) that uses Strang splitting, the Diffused Velocity Method (Ogami and Akamatsu, 1991) and also the Vortex Redistribution Method (Shankar and Van Dommelen, 1996) that was introduced as an alternative to PSE to keep the meshless characteristic of vortex methods. Additionally, Koumoutsakos and Leonard (1995) performed Direct Numerical Simulations using vortex methods combined with remeshing for the solution of the Poisson equation by using high order interpolation formulas. In Rossinelli and Koumoutsakos (2008) the first simulations on GPUs were performed, using particle-mesh operators for the interpolation of the Lagrangian quantities on the grid (and subsequently solving the diffusion on it). In the last decade vortex particle methods have been coupled with finite volume solvers as in the work of Palha et al. (2015), used as sub-grid scale models and also to study two and three dimensional turbulence with very satisfactory results as presented in Yokota et al. (2007).

3

VORTEX METHODS STATE OF THE ART

This chapter consists in presenting a literature review on vortex particle methods. The aspects that are taken into account while constructing a vortex method for viscous, incompressible flows are summarized into different sections. In section 3.1 the governing equations are provided. In section 3.2 the different discretizations chosen for the vorticity field are presented. These can be particles, filaments or sheets. In section 3.3 the velocity evaluation obtained from the Biot-Savart is described. This is usually performed through a Fast Multipole Method for the case of meshless methods or using a grid in case of particle-mesh methods. The latter performs the evaluation by solving a Poisson for velocity either using the stream-function or the vorticity. In section 3.4 solutions to the problem of Lagrangian distortion are presented. This problem can be resolved by two main main ways: redistribution of circulation for the case of grid-free methods and remeshing for the case of Poisson based computations. In section 3.5 the incorporation of viscous effects is presented. With the exception of the Random Vortex Method introduced by Chorin, the diffusion is performed in a deterministic way in all of the vortex methods present in the literature.

3.1 GOVERNING EQUATIONS

The incompressible flow in the domain D is governed by the Navier-Stokes equations:

$$\begin{cases} \frac{D\mathbf{u}}{Dt} = -\frac{\nabla p}{\rho_0} + \nu \Delta \mathbf{u} \\ \nabla \cdot \mathbf{u} = 0 \end{cases} \qquad \mathbf{x} \in D \qquad (3.1)$$

where $\mathbf{u}$ is the velocity, p is the pressure, ρ_0 is the density, ν is the kinematic viscosity of the specific fluid considered.

The problem is defined by initial condition for the velocity field, the no-slip condition along the body surface ∂D and the asymptotic behavior for the velocity in the far field $\mathbf{u}_\infty$:

$$\begin{cases} \mathbf{u}(\mathbf{x},0) & = & \mathbf{u}_0(\mathbf{x}) & \mathbf{x} \in D, \\ \mathbf{u}(\mathbf{x}_b) & = & \mathbf{u}_b & \mathbf{x} \in \partial D, \\ \mathbf{u}(\mathbf{x},t) & \to & \mathbf{u}_\infty(t) & |\mathbf{x}| \to \infty, \end{cases}$$

where $\mathbf{u}_b$ is the body velocity.

Applying the curl operator on the momentum equation (5.1) and using incompressibility constraint, leads to the Helmholtz vorticity transport equation:

$$\frac{D\boldsymbol{\omega}}{Dt} = \boldsymbol{\omega} \cdot \nabla \mathbf{u} + \nu \Delta \boldsymbol{\omega}, \tag{3.2}$$

where $\boldsymbol{\omega} = \nabla \times \mathbf{u}$ is the vorticity. In a two dimensional framework, the vorticity field is a scalar with $\boldsymbol{\omega} = \omega\, \mathbf{e}_3$, where $\mathbf{e}_3$ is the unit normal to the flow plane vector. Hence, the governing equations reduce to

$$\begin{cases} \frac{D\omega}{Dt} & = \nu \Delta \omega \\ \omega(\mathbf{x},0) & = \omega_0(\mathbf{x}) \end{cases} \qquad \mathbf{x} \in D \tag{3.3}$$

$\omega_0(\mathbf{x})$ being the initial vorticity distribution. In the context of vortex particle methods the approximation to the solution of the above equation is considered as a linear combination of Dirac distributions.

3.2 VORTICITY FIELD DISCRETIZATION

3.2.1 *Vortex Particle Methods*

Starting from the 2D point vortex methods introduced by Rosenhead in Rosenhead (1931), the vorticity field is represented by a sum of point masses δ which are the vortex elements, having a circulation Γ_i and with center of the $i-th$ vortex placed at $\mathbf{x}_i$:

$$\boldsymbol{\omega}(\mathbf{x},t) = \sum_{i=1}^{N} \boldsymbol{\Gamma}_i \delta(\mathbf{x} - \mathbf{x}_i(t)), \tag{3.4}$$

where $\boldsymbol{\Gamma} = \int_V \boldsymbol{\omega}\ dV$, which leads to the equivalent representation:

$$\boldsymbol{\omega}(\mathbf{x},t) = \sum_{i=1}^{N} \boldsymbol{\omega}(\mathbf{x}_i(t),t) \mathbf{V}_i \delta(\mathbf{x} - \mathbf{x}_i(t)). \tag{3.5}$$

The velocity induced by the point vortices in free space is given from the Biot-Savart law as:

$$\mathbf{u}(\mathbf{x},t) = \int_V \mathbf{K}(\mathbf{x}-\mathbf{y}) \boldsymbol{\omega}(\mathbf{y},t)\ d\mathbf{y}, \tag{3.6}$$

where $\boldsymbol{\omega} = \omega$ in 2D, thus vorticity becomes a scalar in 2D. The kernel $\mathbf{K}$ is the Biot Savart kernel given by the rotational counterpart of the Green function for the Laplace operator in 2D:

$$\mathbf{K}(\mathbf{x}) = \nabla^{\perp} G(\mathbf{x}) = -\frac{1}{2\pi|\mathbf{x}|^2} \begin{pmatrix} x_2 \\ -x_1 \end{pmatrix}. \tag{3.7}$$

Thus the corresponding representations for the velocity induced is:

$$\mathbf{u}(\mathbf{x}, t) = -\frac{1}{2\pi} \int \frac{(\mathbf{x} - \mathbf{y}) \times \omega(\mathbf{y}, t)\mathbf{k}}{|\mathbf{x} - \mathbf{y}|^2} \, d\mathbf{y}. \tag{3.8}$$

and the discretized versions of the velocity will be:

$$\mathbf{u}(\mathbf{x}_i, t) = -\frac{1}{2\pi} \sum_{j=1}^{N} \Gamma_j(t) \frac{\mathbf{k} \times (\mathbf{x}_i - \mathbf{x}_j)}{|\mathbf{x}_i - \mathbf{x}_j|^2}. \tag{3.9}$$

The singularity of the kernel for the case of point particles coming too close, can lead to unbounded velocity fields and subsequently in numerical instabilities with the ultimate result that the method does not converge. To avoid this, Chorin (1973) introduced the vortex blobs where the point vortices are substituted by finite core vortices with core size ϵ, leading to a desingularization of the kernel. To this end, the δ function is convoluted with a smoothing kernel and the representation (3.4) becomes:

$$\boldsymbol{\omega}(\mathbf{x}) = \sum_{i=1}^{N} \boldsymbol{\Gamma}_i \zeta_{\epsilon}(\mathbf{x} - \mathbf{x}_i), \tag{3.10}$$

where ζ_ϵ is the characteristic distribution of vorticity or cut - off function, ϵ is the core size. In vortex methods the first is usually chosen a Gaussian distribution.

Finally, the vorticity field is obtained by advecting the vortex particles:

$$\frac{d\mathbf{x}_i}{dt} = \mathbf{u}(\mathbf{x}_i, t). \tag{3.11}$$

3.2.2 *Vortex Sheet Methods*

Another representation of the vorticity for the case of 2D methods, is the discretization into vortex sheets. Their were initially used by Rosenhead (1931) while Krasny (1986b), Krasny (1986a) used desingularized vortex sheets avoiding the singularity formation. Their 3D analog are the vortex filaments as we will see in the next paragraph. Vortex sheets are used for the case when the flow is concentrated on a surface. A vortex sheet in a 3D incompressible flow is a 2D surface across which the tangential component of the velocity is discontinuous. The magnitude of the jump represents the intensity of discontinuity. One can imagine a vortex sheet occurring behind an obstacle with a sharp trailing or using it as an approximation of a thin shear layer.

Following, Agishtein and Migdal (1989) and Kaneda (1990), assume a vortex sheet in $\mathbb{R}^3$ is represented by a surface S. A vortex sheet can be described by a parametrization of the surface S as:

$$\mathbf{x}_\gamma(\mathbf{a}, t), \quad \mathbf{a} = (a_1, a_2) \in \mathbb{R}^2, \tag{3.12}$$

$$\gamma = \gamma(\mathbf{a}, t), \tag{3.13}$$

where $\gamma = \mathbf{n} \times [\mathbf{u}]$ and $[\mathbf{u}] = \mathbf{u}_1 - \mathbf{u}_2$ represents the jump in the tangential velocity. Then its Lagrangian motion is described by:

$$\frac{\partial \mathbf{x}_\gamma}{\partial t}(a_1, a_2, t) = \mathbf{u}(a_1, a_2, t). \tag{3.14}$$

Using Biot-Savart law $\mathbf{u}(\mathbf{x}) = \int \boldsymbol{\omega}(\mathbf{y}) \times \nabla G(\mathbf{x} - \mathbf{y})\ d\mathbf{y}$ and since for a vortex sheet: $\boldsymbol{\omega}(\mathbf{x}) = \boldsymbol{\gamma}(\mathbf{x})\delta_S(\mathbf{x})$, then the velocity induced away from it will be:

$$\mathbf{u}(\mathbf{x}) \overset{3D}{=} \frac{1}{4\pi} \int_S \boldsymbol{\gamma}(\mathbf{y}) \times \frac{\mathbf{x} - \mathbf{y}}{|\mathbf{x} - \mathbf{y}|^3}\ dS(\mathbf{y}), \tag{3.15}$$

while on the sheet, using Plemelj formulas, leads to the Cauchy principal value integrals:

$$\mathbf{u}_\pm(\mathbf{x}) = \pm\frac{1}{2}\boldsymbol{\gamma}(\mathbf{x}) \times \mathbf{n}(\mathbf{x}) + \frac{1}{4\pi}\mathrm{PV}\int_S \boldsymbol{\gamma}(\mathbf{y}) \times \frac{\mathbf{x} - \mathbf{y}}{|\mathbf{x} - \mathbf{y}|^3}\ dS(\mathbf{y}), \quad \mathbf{x} \in S. \tag{3.16}$$

The strength of the vortex sheet can be found for the case were the flow outside the vortex sheet region is considered irrotational. In this case the velocities are given by the potential functions $\mathbf{u}_1 = \nabla\phi_1$, $\mathbf{u}_2 = \nabla\phi_2$ thus:

$$\boldsymbol{\gamma} = \mathbf{n} \times (\mathbf{u}_1 - \mathbf{u}_2) = \mathbf{n} \times (\nabla\phi_1 - \nabla\phi_2) = \mathbf{n} \times \nabla_T\Phi, \tag{3.17}$$

where $\Phi = \phi_1 - \phi_2$, $\mathbf{x} \in S$ and ∇_T is the gradient along S, i.e.:

$$\nabla_T\Phi = \nabla\Phi - (\mathbf{n} \cdot \nabla\Phi) \cdot \mathbf{n}. \tag{3.18}$$

Then the vortex sheet will evolve according to Kaneda (1990):

$$\frac{\partial \mathbf{x}_\gamma}{\partial t} = -\frac{1}{4\pi}\mathrm{PV}\int_S (\mathbf{u}(\mathbf{y}) \times \nabla_T\Phi(\mathbf{y})) \times \frac{\mathbf{x}_\gamma(\mathbf{x}) - \mathbf{x}_\gamma(\mathbf{y})}{|\mathbf{x}_\gamma(\mathbf{x}) - \mathbf{x}_\gamma(\mathbf{y})|^3}\ ds(\mathbf{x}_\gamma(\mathbf{y})). \tag{3.19}$$

3.2.3 *Vortex Filament Methods*

Vortex filaments methods can be considered the 3D generalization of 2D vortex particle methods. Introduced in the works of Leonard (1975) and Rehbach (1978) for 3D flow simulations, Vortex Filament Methods are based on the alternative discretization of the vorticity field into filaments. Vortex filaments are spatial curves that induce rotary flow around them. For inviscid flows it follows form Kelvins theorem that just as particles, they have a constant circulation Γ.

Following Leonard (1980) a filament i with circulation Γ_i is defined by parameterizing at time t the curve i as $\mathbf{r}_i(s,t)$, where s is a parameter along the curve. The vorticity field induced by a set of N vortex filaments is:

$$\boldsymbol{\omega}(\mathbf{x},t) = \sum_{i=1}^{N} \Gamma_i \int W_\epsilon(\mathbf{x} - \mathbf{r}_i(s,t)) \frac{\partial \mathbf{r}}{\partial s}\, ds, \tag{3.20}$$

where:

$$\int W_\epsilon(\mathbf{x})\, d\mathbf{x} = 1, \tag{3.21}$$

$$W_\epsilon(\mathbf{x} - \mathbf{r}_i) = \frac{1}{\epsilon^3} W\left(\frac{|\mathbf{x} - \mathbf{r}_i|}{\epsilon}\right), \tag{3.22}$$

is a smoothed function for the 3D Dirac delta function. The velocity field induced by this collection of vortex filaments is given by the Biot-Savart law:

$$\mathbf{u}(\mathbf{x},t) = -\frac{1}{4\pi} \int \frac{(\mathbf{x} - \mathbf{y}) \times \boldsymbol{\omega}(\mathbf{y},t)}{|\mathbf{x} - \mathbf{y}|}\, d\mathbf{y}. \tag{3.23}$$

Then each filament is discretized into a finite number of Lagrangian markers $\mathbf{x}_i$, connected with an appropriate interpolation function in order to reconstruct the vortex filaments at each time step. Rehbach (1978) used for interpolating functions piecewise linear functions while higher order approximations can be used using splines while in Ashurst and Meiburg (1988) 3rd order splines where used.

Finally inserting 3.20 into 3.23 the velocity induced by the N collection of vortex filaments is:

$$\mathbf{u}(\mathbf{x},t) = -\frac{1}{4\pi} \sum_{i=1}^{N} \Gamma_i \int \frac{|\mathbf{x} - \mathbf{r}_j(s,t)| \times \left(\frac{\partial \mathbf{r}_j}{\partial s}\right) q\left(\frac{|\mathbf{x} - \mathbf{r}_j|}{\epsilon}\right)}{|\mathbf{x} - \mathbf{r}_j(s,t)|^3}\, ds, \tag{3.24}$$

where:

$$q(y) = 4\pi \int_0^y f(z) z^2\, dz. \tag{3.25}$$

The main drawback of the filament discretization is that in regions where vorticity is very large, there is singularity formation (in finite time) caused by the thinning of the filaments due to stretching of vorticity (see *e.g.* Sakajo (2001)). For these reason remeshing techniques are used, as for the case of particle methods, with the main of these described in 3.4.

3.3 VELOCITY EVALUATION

The evaluation of the velocity field induced from the vorticity field of N vortex particles constitutes an N-body problem since it requires $\mathcal{O}(N^2)$ computations. In order to avoid the quadratic computational cost of the direct evaluation, two different classes of methods are used: Hybrid and direct methods.

3.3.1 *Hybrid methods*

Hybrid methods are used in particle-mesh vortex methods. The first vortex method to make use of them was the Vortex in cell (VIC) method introduced by Christiansen (1973). The main characteristic of the method is that a grid is used for the evaluation of the velocity field resulting in a Lagrangian - Eulerian formulation. At a first stage vorticity is discretized into vortex particles and the strength of the particles is interpolated onto the nodes of an underlying grid upon which the following Poisson is solved:

$$\Delta\mathbf{u} = -\nabla \times \boldsymbol{\omega}, \tag{3.26}$$

with $\boldsymbol{\omega} = (\omega_1, \omega_2, \omega_3)$ in 3D and $\boldsymbol{\omega} = \omega k$ in 2D. The velocities are then interpolated from the grid back to the particles which are advected according to:

$$\frac{d\mathbf{x}_i}{dt} = \mathbf{u}_i. \tag{3.27}$$

The advantage of the VIC, is that the convection term is again not discretized explicitly, thus it is not subjected to a CFL condition. However, the drawback is coming from the introduction of error due to the solution of the Poisson and the interpolation procedure.

3.3.2 *Direct methods*

In the case of direct methods the velocity evaluation is performed by subdividing the set of N vortices into groups/clusters and approximating their velocity influence to other particles or clusters through a truncated (Laurent or Taylor) series expansion. The organization of the particles into clusters is performed in a hierarchical manner where the computational domain is successively subdivided into subdomains. This hierarchical process is accompanied by the introduction of a tree-data structure (quad-tree in 2D and oct-tree in 3D) in order to provide criteria for when the direct or the approximate evaluation of the velocity will take place.

The method introduced by Greengard and Rokhlin (1987) is the Fast Multipole Method (FMM) and results in a $\mathcal{O}(N)$ total computational cost. This is achieved by considering, particle-cluster interactions and additionally cluster-cluster interactions by recasting the velocity into a Taylor series expansion.

Another approach was introduced in the vortex method of Van Dommelen and Rundensteiner (1989) based on the tree-data structure of Appel (1985) resulting in a total computational cost of $\mathcal{O}(N \log N)$. In this case only particle-cluster interactions are considered and the approximations are recast as Laurent series expansions.

3.4 TREATMENT OF LAGRANGIAN DISTORTION

The automatic adaptivity of particle methods to the flow field is among the most powerful advantages with respect to the finite difference or finite volume methods. However the Lagrangian formulation is inherited with particle distortion caused by the strain of the flow. If the field of particles becomes too distorted then the overlap criterion (or equivalently the criterion of regular distribution) that is necessary for vortex methods to converge (see *e.g.* Hald (1979), Beale and Majda (1982a)) is violated. To overcome this problem, researchers follow different strategies and in the following a brief description of the main methods used will be listed.

One way to treat the Lagrangian distortion is through the frequent redistribution of vorticity, and more especially of the circulation. Following Cottet and Koumoutsakos (2000), redistribution refers to the *processing of circulation* as a way to control the effect of distortion. For a given velocity discretization:

$$\mathbf{u}(\mathbf{x}_i, t) = \sum_{j=1}^{N} \Gamma_j(t)\mathbf{K}_\epsilon(\mathbf{x}_i - \mathbf{x}_j) \tag{3.28}$$

$$= \sum_{j=1}^{N} \boldsymbol{\omega}(\mathbf{x}_j, t)V_j\mathbf{K}_\epsilon(\mathbf{x}_i, \mathbf{x}_j), \tag{3.29}$$

where using $\boldsymbol{\Gamma} = \int_V \boldsymbol{\omega}\ dV$, each particle is assigned a circulation vector $\boldsymbol{\Gamma}_j = \boldsymbol{\omega}_j V_j$, which corresponds to its quadrature weight. Then at each step it is possible to evaluate the corrected circulation values $\boldsymbol{\Gamma}_j^{cor}$ that recover the vorticity from the domain which leads to:

$$\boldsymbol{\omega}_j = \sum_{j=1} \boldsymbol{\Gamma}_j^{cor}\zeta_\epsilon(\mathbf{x}_i - \mathbf{x}_j) \tag{3.30}$$

$$\Rightarrow \boldsymbol{\Gamma}_j = \sum_{j=1} \boldsymbol{\Gamma}_j^{cor}\zeta_\epsilon(\mathbf{x}_i - \mathbf{x}_j)V_j \tag{3.31}$$

$$\Rightarrow \boldsymbol{\Gamma} = \mathbf{A}\boldsymbol{\Gamma}^{cor}. \tag{3.32}$$

Thus in order to evaluate the corrected circulations, the inversion of the sparse, $N \times N$ matrix $\mathbf{A}$ needs to be performed at each time step. Since direct inversion is inefficient, indirect and fast techniques are used (see *e.g.* Marshall and Grant (1996)).

Another method to treat Lagrangian distortion is using remeshing which is realized by reinitializing the particles on a grid in order to avoid distortion. As such, remeshing schemes resolve the problem of distortion by processing the location of the particles. Remeshing consists in using a mesh M overlayed with the particles P and interpolating the particles strength $\boldsymbol{\Gamma}$ on the mesh as shown in figure 3.1.

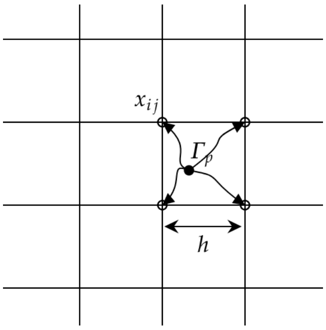

Figure 3.1: A particle with circulation Γ_p and the adjacent mesh node $\mathbf{x}_{ij}$ on which its circulation is interpolated

This is achieved by evaluating the discretized vorticity on the grid locations:

$$\boldsymbol{\omega}(\mathbf{x}_{ij}) = \sum_{N} \boldsymbol{\Gamma}_p \zeta^h(\mathbf{x}_{ij} - \mathbf{x}_p), \tag{3.33}$$

where $\mathbf{x}_{ij}$ are the grid nodes, $\mathbf{x}_p$ is the position of the particle and h is the mesh width. The remeshing is performed periodically in order to avoid large distortions of the particles. The interpolation rule has the form:

$$\boldsymbol{\Gamma}_{ij} = \sum_{p} \boldsymbol{\Gamma}_p W\left(\frac{\mathbf{x}_{ij} - \mathbf{x}_p}{h}\right), \tag{3.34}$$

where $\boldsymbol{\Gamma}_{ij}$ is the unknown circulation on the grid nodes. Thus on node $\mathbf{x}_{ij}$ with circulation unknown, we interpolate the circulations for p particles inside a radius given by the smoothing radius of the kernel W as it can be seen in figure 3.2. The interpolation kernel is crucial to the quality of the interpolation because it can introduce numerical diffusion. For this reason it is chosen so as to satisfy high-order moment properties for the conservation of higher order vorticity moments. Usual choices for the interpolation function are the M_4' kernel (Koumoutsakos et al. (2008)) which can preserve moments of vorticity up to second order. It is also smooth

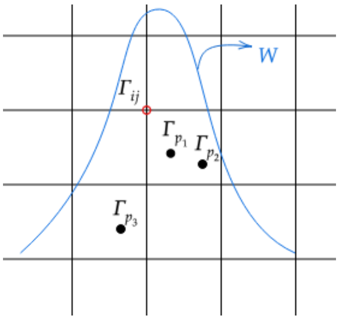

Figure 3.2: The unknown circulation at the mesh node $\boldsymbol{\Gamma}_{ij}$ is found by interpolating the circulations of all particles p that are within the radius of the kernel W

enough which allows for less frequent remeshing. Other choice is that of the Radial Basis Functions (see *e.g.* Barba et al. (2003)). However remeshing methods in order to completely avoid distortions need to be performed at every step.

3.5 VISCOUS EFFECTS

3.5.1 *Random Vortex Method*

The Random Vortex Method originally introduced by Chorin (1973) was the prototype of viscous vortex methods. The method is based on operator splitting between advection and diffusion steps. The diffusion of vorticity is performed by vortex blob particles that undergo Brownian motion. Under this assumption the i-th particle position is updated using:

$$\mathbf{x}_i^{n+1} = \mathbf{x}_i^n + \xi_i^n, \tag{3.35}$$

where ξ_i^n are Gaussian independent random variables with probability distribution:

$$G\left(\mathbf{x}, \frac{\epsilon}{2}\right) = \frac{1}{\left(\sqrt{2\pi\epsilon}\right)^d} \exp\left(-\frac{\mathbf{x}^2}{2\epsilon}\right), \tag{3.36}$$

with zero mean, where $\epsilon = \sqrt{2\nu\delta t}$ is the variance and d the spatial dimension.

Although the implementation of the method is rather simple, the main disadvantage is that the convergence is slow thus requiring a large number of particles for increasing Reynolds number to reach an accurate result (see *e.g* Leonard (1980), Milinazzo and Saffman (1977)).

3.5.2 *Core Spreading*

Introduced by Kuwahara and Takami (1973) for the case of planar flows, the Core Spreading method is the first deterministic vortex method. It uses the exact solution of the diffusion equation and is not implemented using an operator splitting i.e. it solves:

$$\frac{D\omega}{Dt} = \nu\Delta\omega. \tag{3.37}$$

Following Rossi (1996) the vorticity field is represented by Gaussian blobs as:

$$\omega(\mathbf{x}) = \sum_{i=1}^{N} \frac{\Gamma_i}{4\pi\sigma_i^2} \exp\left(-\frac{|\mathbf{x}-\mathbf{x}_i|^2}{4\sigma_i^2}\right), \tag{3.38}$$

where $\mathbf{x}_i$ is the center of the blob i. The original method proceeded by changing the size of each blob to match the analytical solution of the heat equation, while keeping their circulation constant. For solving the unsplit equation, the blobs need to convect and diffuse which leads to the system:

$$\frac{d\mathbf{x}_i}{dt} = \begin{pmatrix} 0 & -1 \\ 1 & 0 \end{pmatrix} \sum_{i=1}^{N} \frac{\Gamma_i}{2\pi} \frac{\mathbf{x}_i - \mathbf{x}_j}{|\mathbf{x}_i - \mathbf{x}_j|^2} \left(1 - \exp\left(-\frac{|\mathbf{x}_i - \mathbf{x}_j|^2}{4\sigma_j^2}\right)\right) \tag{3.39}$$

$$\frac{d\sigma_i^2}{dt} = \nu. \tag{3.40}$$

The first equation reveals that the whole blob will move with the vorticity of the center. The second equation shows that each Gaussian blob will expand to satisfy the analytical solution of the diffusion equation, thus the core size can grow unbounded. This problem was highlighted from Greengard (1985) and was addressed by Rossi (1996) by applying vortex splitting to blobs that exceeded a threshold radius. Overall, the Core Spreading method is completely meshfree and very simple to model diffusive effects.

3.5.3 *Particle Strength Exchange*

In Particle Strength Exchange, presented originally in Mas-Gallic (1987), the Laplace operator is substituted by an integral operator. Since vortex methods are inherently quadrature methods, the integral representation of operators is considered well suited to their structure. This operator is realized as:

$$\Delta_\epsilon \boldsymbol{\omega}(\mathbf{x}) = \frac{1}{\epsilon^d} \int (\boldsymbol{\omega}(\mathbf{x}) - \boldsymbol{\omega}(\mathbf{y}))\, \eta_\epsilon(\mathbf{x} - \mathbf{y})\, d\mathbf{y}, \tag{3.41}$$

where η_ϵ is the smoothed Green function for the Laplace equation. The smoothing/cut-off function:

$$\eta_\epsilon(\mathbf{x}) = \frac{1}{\epsilon^d} \eta\left(\frac{\mathbf{x}}{\epsilon}\right), \quad d = 2, 3, \tag{3.42}$$

is symmetric with compact support and satisfies 2nd order moment conditions. These assumptions are based on the fact PSE methods are exchanging vorticity/circulation between particles and thus are minimum assumptions for conservation properties to be respected.

Using this approximation for the diffusion of vorticity then during advection the vorticity field is discretized into particles. Using the location and the volume of these particles as nodes and weights respectively, the quadrature points for the integral representation of the Laplacian are obtained. Then the method consists in solving a system that gives the position, volume and strength of each particle.

In general, PSE is a meshless method however it is sensitive to particle locations since the Laplace operator is discretized on these locations. This led to the introduction of a mesh in order to control the regularity of the particle field resulting in the Remeshed Vortex Method described in subsection 3.5.5.

3.5.4 *Diffused Velocity Method*

A different approach to account for the viscous diffusion is the Diffused Velocity Method (DVM) (Ogami and Akamatsu, 1991) which modifies the velocity instead of the core radius or the circulation. In DVM the diffusion term is written as advective term which gives the diffusive velocity. Consider the transport equation for the scalar field of vorticity in 2D:

$$\frac{\partial \omega}{\partial t} + \nabla \cdot (\mathbf{u}\omega) = \nabla \cdot (\nu \nabla \omega). \tag{3.43}$$

Setting:

$$\mathbf{u}_d(\mathbf{x}, t) = -\nu \frac{\nabla \omega}{\omega}, \tag{3.44}$$

the advection equation can be written in a purely convective form:

$$\frac{\partial \omega}{\partial t} + \nabla \cdot ((\mathbf{u} + \mathbf{u}_d)\omega) = 0. \tag{3.45}$$

Then each vortex i is displaced according to:

$$\frac{d\mathbf{x}_i}{dt} = \mathbf{u}(\mathbf{x}_i(t)) + \mathbf{u}_d(\mathbf{x}_i(t)), \tag{3.46}$$

where $\mathbf{u}_d$ is the diffusion velocity and $\mathbf{u}$ is the fluid velocity which is evaluated using the Biot-Savart formula.

Though the method is completely meshless it suffers from two main problems. The first is the Lagrangian distortion that is treated with remeshing (re-initializing) the particles. The second is that the diffusion velocity can be assigned an unreasonable large or singular value when the vorticity is close or equal to zero respectively. To overcome this Ogami (2000) evaluates separately the $\mathbf{u}_d$ of vortices with negative and positive circulation. Nevertheless, the method needs a large number of overlapping vortices for accurate simulations due to the large variations in the diffusion velocity in different regions of the flow. Alternatively, to treat the singularity of very large gradients of $\mathbf{u}_d$ Mycek et al. (2013) uses a hybrid DVM-PSE method where when $\mathbf{u}_d$ is nonsingular a regularized version of DVM is used (see Mas-Gallic (2002)), while when it is singular the PSE scheme is used. A similar method is Viscous Vortex Domains (VVD) (Dynnikova, 2004), which is based on DVM method but it differs at the discrete formulas used for the evaluation of the diffusion velocity.

3.5.5 *Remeshed Vortex Method*

Following Koumoutsakos and Leonard (1995) the convective part in the Remeshed Vortex Method (RVM) is solved using vortex blobs where the induced velocity is evaluated using the Biot-Savart combined with a Fast Multipole Method while the diffusive part is solved using the PSE scheme. The Lagrangian distortion is dealt through remeshing: The distorted locations of the particles are remeshed onto a uniform grid and the old vorticity is interpolated on the new particle locations. Denoting by Γ_i and $(\mathbf{x}_i, \mathbf{y}_i)$ the circulation and location of the old vortex respectively, then its circulation contribution $\Delta\Gamma_{j,i}$ to the new mesh point $\left(\tilde{\mathbf{x}}_i, \tilde{\mathbf{y}}_j\right)$ is dictated by the tensor product:

$$\Delta\Gamma_{j,i} = \Gamma_i W\left(\frac{\tilde{\mathbf{x}}_j - \mathbf{x}_i}{h}\right) W\left(\frac{\tilde{\mathbf{y}}_j - \mathbf{y}_i}{h}\right), \tag{3.47}$$

where h is the grid spacing. The interpolation kernel W is chosen in order to conserve circulation, linear and angular momentum and is given by:

$$W(u) = \begin{cases} 1 - u^2, & 0 \leqslant |u| < \frac{1}{2} \\ \frac{1}{2}(1-u)(2-u), & \frac{1}{2} \leqslant |u| < \frac{3}{2} \\ 0, & otherwise. \end{cases} \tag{3.48}$$

The choice of the kernel function is of importance since interpolation is prone to numerical diffusion (se e.g. Barba et al. (2003)). This in turn can be reduced if the kernel function is chosen so as to conserve vorticity moments up to the desired order. Example of higher order interpolation function are found in Monaghan and Lattanzio (1985) such as the M_4' kernel used in the work of Eldredge (2007).

A crucial point is the frequency of remeshing. Hieber and Koumoutsakos (2005) introduced a measure of distortion of the field based on which remeshing is performed. This measure is based on the fact that the weight sum $H(t)$ over all particles must be equal to unity in a regularized particle map:

$$H(t) = \sum_j u_j W_\epsilon(\mathbf{x}_i(t) - \mathbf{x}_j(t)), \tag{3.49}$$

$$H(0) = H_0 = 1. \tag{3.50}$$

The average change of $H(t)$ over all particles is a measure for their distortion:

$$\Delta H = \frac{1}{N} \sum_j \frac{|H_j(t) - H_{0,j}|}{H_{0,j}}, \tag{3.51}$$

where N is the number of particles and the remeshing is performed when the function ΔH exceeds a specified threshold.

3.5.6 *Vorticity Redistribution Method*

The method was presented in Shankar and Van Dommelen (1996) and it is also based on the redistribution of the strength of vortex particles like the PSE method, but it does not require remeshing. In order to simulate diffusion of a vortex i during a time step, fractions of its circulation are distributed to the neighboring particles within a radius $h_\nu = \sqrt{\nu \Delta t}$, Δt being the diffusion step, where vortex j belongs to the neighborhood $|\mathbf{x}_i - \mathbf{x}_j| \leqslant R h_\nu$. Indicating with f_{ij} the fraction of circulation moved from i to j, the redistribution method changes the vorticity distribution:

$$\omega^n = \sum_{i=1}^{N} \Gamma_i^n \zeta_\epsilon(\mathbf{x} - \mathbf{x}_i), \tag{3.52}$$

into:

$$\omega^{n+1} = \sum_{i=1} \sum_{j=1} f_{ij}^n \Gamma_i^n \zeta_\epsilon(\mathbf{x} - \mathbf{x}_j), \tag{3.53}$$

where:

$$\zeta_\epsilon = \frac{1}{\epsilon^2} \zeta\left(\frac{\mathbf{x}}{\epsilon}\right). \tag{3.54}$$

Then in order to determine the f_{ij} contributions the method proceeds by equating the truncated Taylor expansion of the new distribution with the one of the exact solution. I.e. using the fact that in the neighborhood of the vortex i, $|\mathbf{x}_i - \mathbf{x}_j|$ is of order $\mathcal{O}\left(\sqrt{\Delta t}\right)$, the approximations of the trailing exponential terms of the corresponding Fourier transforms can be approximated by a truncated Taylor series. By equating the terms of the same order we find the relations that f_{ij} need to satisfy within the radius. These relations serve to satisfy moment conditions locally that is, in the neighborhood of the vortex i.

Thus by taking the Fourier transform of the approximated ω^{n+1}:

$$\hat{\omega}^{n+1} = \hat{\zeta}(k\epsilon) \sum_{i=1} \Gamma_i^n e^{-i\mathbf{k} \cdot \mathbf{x}_i} \sum_{j=1} f_{ij}^n e^{-i\mathbf{k} \cdot (\mathbf{x}_j - \mathbf{x}_i)}. \tag{3.55}$$

and comparing it with the one of the exact solution of the vorticity diffusion:

$$\hat{\omega}_e^{n+1} = \hat{\zeta}(k\epsilon) \sum_{i=1} \Gamma_i^n e^{-i\mathbf{k} \cdot \mathbf{x}_i} e^{-|k|^2 \nu \Delta t} \tag{3.56}$$

Though the Vortex Redistribution Method is among the truly meshless vortex methods, it is based on effective search strategy to identify the particles within a given distance from the point of interest.

4

OVERVIEW OF THE DVH METHOD

In this chapter the basic structure of the vortex method DVH is described. In section 4.1 splitting is presented and the description of each step is presented in the following. In 4.2 the solution of the advection step is presented in based on the approximation of the Euler equations and the formulation of the advection step based on characteristics. In section 4.3 the diffusion step is described based again on a particle formulation.

4.1 OPERATOR SPLITTING

When the viscous splitting algorithm is used to evolve the solution of NSEs, the vorticity evolution is splitted into substeps. To this end, the two-dimensional vorticity formulation of Navier-Stokes for a viscous fluid occupying a domain D is splitted into an Euler step and a diffusion step. In the first step the evolution in space of an inviscid fluid is considered, using the Euler equation:

$$\frac{\partial \omega}{\partial t} + \mathbf{u} \cdot \nabla \omega = 0. \tag{4.1}$$

For a two dimensional flow the stretching term of the vorticity equal to $\omega \cdot \nabla \mathbf{u}$ is null. Thus vorticity is a material quantity. The next step is governed by the heat equation that models the viscous effects:

$$\frac{\partial \omega}{\partial t} = \nu \Delta \omega. \tag{4.2}$$

The main advantage of the above splitting is that dedicated methods can be used to solve each sub-step. The operator splitting corresponds to equations that are easier to solve than the full Navier-Stokes equations. As discussed in LeVeque et al. (2002) the above splitting is first order in time. To obtain higher accuracy in time a second order splitting (symmetric Strang splitting) is possible (see *e.g.* Fishelov (1990), Ramachandran (2004)).

4.2 ADVECTION

During the first sub-step the flow is governed by the Euler equations:

$$\frac{\partial \omega}{\partial t} + \mathbf{u} \cdot \nabla \omega = 0 \tag{4.3}$$

$$\omega(\mathbf{x}, t_0) = \omega_0 \tag{4.4}$$

$$\nabla \cdot \mathbf{u} = 0 \tag{4.5}$$

$$\nabla \times \mathbf{u} = \omega \tag{4.6}$$

$$|\mathbf{u}| \to \mathbf{u}_\infty, \quad \mathbf{x} \to \infty, \tag{4.7}$$

along with the no-through condition on solid boundaries. Using the equations governing the kinematics of the flow the vorticity is coupled to the velocity through the stream-function by the Poisson equation:

$$-\Delta \psi = \omega, \tag{4.8}$$

with solution:

$$\psi = G \star \omega = \int G(\mathbf{x}, \mathbf{y}) \omega(\mathbf{y}) d\mathbf{y}, \tag{4.9}$$

where G is the fundamental solution of the Laplace equation in free space:

$$G(\mathbf{x}) = -\frac{1}{2\pi} \log(|\mathbf{x}|). \tag{4.10}$$

Applying the curl operator in (4.9) follows the representation of the velocity:

$$\mathbf{u}(\mathbf{x}, t) = \mathbf{u}_\infty + \int \mathbf{K}(\mathbf{x}, \mathbf{y}) \omega(\mathbf{y}, t) d\mathbf{y}, \tag{4.11}$$

where K is the Biot-Savart kernel and is defined as:

$$\mathbf{K}(\mathbf{x}) = \frac{1}{2\pi |\mathbf{x}|^2} [-x_2, x_1]^T. \tag{4.12}$$

To account for the body contribution to the velocity a potential term $\mathbf{u}_\phi$ is added to 4.11 leading to the velocity representation:

$$\mathbf{u}(\mathbf{x}, t) = \mathbf{u}_\infty + \int \mathbf{K}(\mathbf{x}, \mathbf{y}) \omega(\mathbf{y}, t) d\mathbf{y} + \mathbf{u}_\phi, \tag{4.13}$$

where for the representation of the velocity $\mathbf{u}_\phi$ a formulation based on Green's functions is used as it will be shown in section 5.4.

The approximation of the vorticity with particles follows from the Lagrangian nature of the Euler equations. They describe the transport of a material quantity. An immediate consequence is that in inviscid flow every closed curve will transport with the velocity of the fluid. This leads to the well-known theorem of circulation conservation due to Kelvin. This is the main idea behind the Lagrangian character of vortex methods.

Following Riccardi and Durante (2007), to construct such a numerical approximation of the fluid it is possible to subdivide the initial support of vorticity onto a number of subdomains each containing a point vortex with its initial circulation Γ_i, leading to :

$$\omega_0 = \omega(\mathbf{x}, 0) \approx \sum_{j}^{N} \Gamma_j \delta(\mathbf{x} - \mathbf{x}_j(0)). \tag{4.14}$$

Thus by Kelvin's theorem the total circulation at time $t > 0$ will be conserved leading to the following approximation for the vorticity:

$$\omega(\mathbf{x}, t) \approx \sum_{j}^{N} \Gamma_j \delta(\mathbf{x} - \mathbf{x}_j(t)), \tag{4.15}$$

where $\Gamma_j = \Gamma(\mathbf{x}_j(t))$. The realization of this procedure is done by following the trajectories of the particles along their characteristics. Denote by $\mathbf{X}(t; \mathbf{x}, t_0)$ the characteristic of the particle that at time $t = t_0$ was at the position $\mathbf{x}$. Then the solution of time $t > t_0$ will be given by the integration of the following system of ordinary differential equations for the trajectory of the particle:

$$\frac{d\mathbf{X}}{dt} = \mathbf{u}(\mathbf{X}, t) \tag{4.16}$$

$$\mathbf{X}(t_0; \mathbf{x}, t_0) = \mathbf{x}. \tag{4.17}$$

Substituting in the above equation, equation (4.11) leads to:

$$\frac{d\mathbf{X}}{dt} = \int \mathbf{K}\left[\mathbf{X}(t; \mathbf{x}, t_0) - \mathbf{Y}(t; \mathbf{y}, t_0)\right] \omega(\mathbf{y}, t) d\mathbf{y}. \tag{4.18}$$

Due to incompressibility the transformation $\mathbf{x} \to \mathbf{X}(t; \mathbf{x}, t_0)$ has Jacobian

$$J(t; \mathbf{x}, t_0) = \left| \det \frac{\partial \mathbf{X}}{\partial \mathbf{x}} \right| = 1, \tag{4.19}$$

and equation (4.18) can be written as:

$$\frac{d\mathbf{X}}{dt} = \int \mathbf{K}\left[\mathbf{X}(t; \mathbf{x}, t_0) - \mathbf{Y}(t; \mathbf{y}, t_0)\right] \omega(\mathbf{X}(t; \mathbf{y}, t_0), t) d\mathbf{y}. \tag{4.20}$$

The discretization of the above equations is done by setting $\omega = \sum_j \omega_j$ and denoting the circulation of each particle by $\Gamma_j = \int \omega_j \, dV$ leading to the following system of ordinary differential equations for the locations of the particles $\mathbf{x}_i$:

$$\frac{d\mathbf{x}_i(t)}{dt} = \mathbf{u}_i(t) = \sum_{j} \Gamma_j(t) \mathbf{K}(\mathbf{x}_i(t) - \mathbf{x}_j(t)) \tag{4.21}$$

$$\mathbf{x}_i(t_0 = 0) = \mathbf{x}. \tag{4.22}$$

Following Beale and Majda (1982b) the singularity at $\mathbf{x} = 0$ of the kernel K in the definition of the velocity representation (4.11) is removed by convolution of K with a smooth cut-off function ζ_ϵ, where ζ_ϵ needs to satisfy the following conditions:

- Normalization property:

$$\int \zeta(x)\, dx = 1. \tag{4.23}$$

- Regularization property:

$$\zeta_\epsilon(x) = \frac{1}{\epsilon^d}\zeta\left(\frac{x}{\epsilon}\right), \quad d = 2, 3, \quad \epsilon > 0, \tag{4.24}$$

- Moment conservation property up to *order* $r \in \mathbb{N}$:

$$\int \zeta(x)x^\beta = 0, \forall \quad 0 < |\beta| \leqslant r - 1 \quad \text{with multi-index} \quad \beta, \tag{4.25}$$

$$\int |\zeta(x)||x|^r \, dx < \infty. \tag{4.26}$$

The above properties follow from a Fourier analysis which shows that the order of the smoothing is equal to the number of moments conserved by the new distribution of vorticity. The property (4.23) is a normalization constraint that represents the conservation of mass, that is the conservation of total vorticity which corresponds to a moment condition of zeroth order. Following is (4.24) which is a regularization or scaling property while (4.25) - (4.26) represent the conservation of higher order moments and finite r-order moment respectively. The properties of the regularized smoothing kernel are directly connected with the convergence and conservation properties of vortex methods and higher order smoothing functions yield faster convergence depending on the choice of ϵ in the case of Euler equations (Beale and Majda, 1985).

Usually, the smoothing kernel is chosen as radially symmetric i.e. for $|\mathbf{x}| = \rho$, $\zeta = \zeta(\rho)$ for example a Gaussian. However, evaluating moments of high order Gaussian functions is computationally expensive with respect to algebraic ones, thus the latter are preferred and in this work the following even kernel introduced in Ranucci (1995) is used:

$$\zeta(\rho) = \frac{2(2-\rho^2)}{\pi(1+\rho^2)^4}. \tag{4.27}$$

(For an exhaustive presentation on algebraic kernel functions see Speck (2011)).

The use of the function (4.27) leads to the smoothed kernel function with the explicit representation:

$$K_\epsilon = K \star \zeta_\epsilon = -\frac{1}{2\pi|\mathbf{x}|^2\epsilon^2}[-x_2, x_1]^T \left(\frac{2\left(2 - \left(\frac{x}{\epsilon}\right)^2\right)}{\pi\left(1 + \left(\frac{x}{\epsilon}\right)^2\right)^4} \right). \tag{4.28}$$

4.3 DIFFUSION

The diffusion step is governed by the heat equation with initial condition for vorticity:

$$\frac{\partial \omega}{\partial t} = \nu \Delta \omega, \tag{4.29}$$

$$\omega(\mathbf{x}, t_0) = \omega_0(\mathbf{x}). \tag{4.30}$$

Its solution is expressed in integral form as:

$$\omega(\mathbf{x}, t) = \int G_\nu(\mathbf{x}, \mathbf{y}; t, t_0)\omega(\mathbf{y}, t_0)d\mathbf{y}, \quad t > t_0, \tag{4.31}$$

where G_ν is the fundamental solution for the heat equation in free space:

$$G_\nu(\mathbf{x}, \mathbf{y}, t - t_0) = \frac{1}{4\pi(t - t_0)} e^{-\frac{|\mathbf{x}-\mathbf{y}|^2}{4(t-t_0)}}. \tag{4.32}$$

The major difference now is that a parabolic equation needs to be solved treated by a formulation that was up to now tailored for hyperbolic equations. Additionally even for compactly supported vorticity information travels at infinite speeds thus it evolves into global support that decays exponentially.

However, from the integral representation of the solution of the heat equation and the superposition of its solutions the following can be obtained. The representation of the solution of the heat equation in free space using the particle approximation of vorticity leads to the following form by inserting (4.15) into (4.31):

$$\omega(\mathbf{x}, t) = \int \omega(\mathbf{y}, t_0) G_\nu(\mathbf{x}, \mathbf{y}; t - t_0) dV_y \tag{4.33}$$

$$= \int \sum_{j=1}^{N} \Gamma(\mathbf{y}_j(t_0))\delta(\mathbf{y} - \mathbf{y}_j) G_\nu(\mathbf{x}, \mathbf{y}; t - t_0) dV_y \tag{4.34}$$

$$= \sum_{j=1}^{N} \Gamma_j(t_0) G_\nu(\mathbf{x} - \mathbf{y}_j; t - t_0) \tag{4.35}$$

$$= \sum_{j=1}^{N} \frac{\Gamma_j(t_0)}{4\pi\nu(t - t_0)} e^{-\frac{|\mathbf{x}-\mathbf{y}_j|^2}{4\nu(t-t_0)}}, \quad t > t_0, \tag{4.36}$$

which gives the vorticity ω at a point $\mathbf{x}$ in space at time t as the sum of the initial vorticity contribution from all the particles at positions $\mathbf{y}_j$ at time t_0. The details of the diffusion process for the vortex particle DVH used in this work, will be given in the next chapter in section 5.6 where the diffusion is performed using a Regular Point Distribution (RPD) of nodes. This distribution of nodes is in a body-fitted configuration near the boundary of the body while far from it is Cartesian.

The solution process of the viscous splitting in the presence of solid boundaries, requires also the introduction of a procedure to enforce the boundary condition of no-slip. This is due to the fact that during the advection using the solution of equation (4.3) , the velocity field satisfies only the no-through condition (i.e. $\mathbf{u} \cdot \mathbf{n} = \mathbf{u}_b \cdot \mathbf{n}$) while the proper boundary condition of the full problem is a no-slip condition (i.e. $\mathbf{u} = \mathbf{u}_b$). The boundary condition of no-slip is restored by generating a vortex sheet on the boundary. As it will be described in subsection 5.4.2 this procedure uses the Helmholtz Hodge Decomposition for the velocity field and the enforcement of the boundary condition is performed using an Indirect Boundary Element Method (IBEM).

Part II

DETAILS OF THE NUMERICAL METHODS

5

SOLVING THE VORTICITY - VELOCITY FORMULATION WITH DVH

This chapter deals with the detailed presentation of the mathematical model used in vortex particle method DVH. Section 5.1 presents the derivation of the governing equations of the vorticity - velocity formulation for incompressible flows. Then the resolution of this formulation based on the viscous splitting method of Chorin (1973) is described. In section 5.4 the evaluation of the velocity field and the enforcement of boundary conditions in the presence of a boundary is described. This formulation is based on the Helmholtz - Hodge Decomposition (HHD) where the rotational component is assigned to the vorticity field while the gradient term is assigned to a potential arising due to the existence of the boundary. The potential term is represented by an Indirect Boundary Integral Equation. In section 5.4 the details of this formulation are presented in comparison with the direct method usually employed in vortex methods. In section 5.5 the evaluation of the velocity field using a Fast Multipole Method is described, that decreases the computational cost of the evaluation of velocity from vorticity. Section 5.6 contains the details of the diffusion process both in free space and in the presence of solid boundaries and finally in section 5.7 the equations for deriving the hydrodynamic loads are presented.

5.1 GOVERNING EQUATIONS

The incompressible flow in the domain D is governed by the Navier-Stokes equations:

$$\begin{cases} \frac{D\mathbf{u}}{Dt} = -\frac{\nabla p}{\rho_0} + \nu \Delta \mathbf{u} + \mathbf{f}, \\ \nabla \cdot \mathbf{u} = 0, \end{cases} \qquad \mathbf{x} \in D, \tag{5.1}$$

where $\mathbf{u}$ is the velocity, p is the pressure, ρ_0 is the density, ν is the kinematic viscosity of the specific fluid considered, $\mathbf{f}$ is a generic external force field; in the following, it is assumed that $\mathbf{f} = 0$. The problem is defined by initial condition for the velocity field, the no-slip condition along the body surface ∂D_B and the asymptotic behavior (radiation condition) for the velocity in the far field $\mathbf{u}_\infty$:

$$\begin{cases} \mathbf{u}(\mathbf{x},0) = \mathbf{u}_0(\mathbf{x}), & \mathbf{x} \in D, \\ \mathbf{u}(\mathbf{x}_b) = \mathbf{u}_b, & \mathbf{x} \in \partial D_B, \\ \mathbf{u}(\mathbf{x},t) \to \mathbf{u}_\infty(t) & |\mathbf{x}| \to \infty, \end{cases}$$

where $\mathbf{u}_b$ is the body velocity. Figure 5.1 shows a sketch of the problem with the convention used for the orientation of normal and tangential unit vectors on ∂D_B.

5.2 VISCOUS SPLITTING

The splitting technique used in the DVH method for the solution of Navier–Stokes relies on the Helmholtz–Hodge Decomposition (HHD) theorem, as the velocity field is split into a potential part and a rotational part, as described in the following. Applying the curl operator on the momentum equation (5.1) and using the kinematic constraint $\nabla \cdot \mathbf{u} = 0$, the vorticity–velocity formulation of the NSEs reads:

$$\frac{D\boldsymbol{\omega}}{Dt} = \boldsymbol{\omega} \cdot \nabla \mathbf{u} + \nu \Delta \boldsymbol{\omega}, \tag{5.2}$$

where $\boldsymbol{\omega} = \nabla \times \mathbf{u}$ is the vorticity. In a two dimensional framework, the vorticity field is simply $\boldsymbol{\omega} = \omega\, \mathbf{e}_3$, where $\mathbf{e}_3$ is the unit normal to the flow plane vector. Hence, the governing equations reduce to:

$$\begin{cases} \frac{D\omega}{Dt} = \nu \Delta \omega, \\ \omega(\mathbf{x},0) = \omega_0(\mathbf{x}), \end{cases} \quad \mathbf{x} \in D, \tag{5.3}$$

$\omega_0(\mathbf{x})$ being the vorticity distribution at initial time t_0.

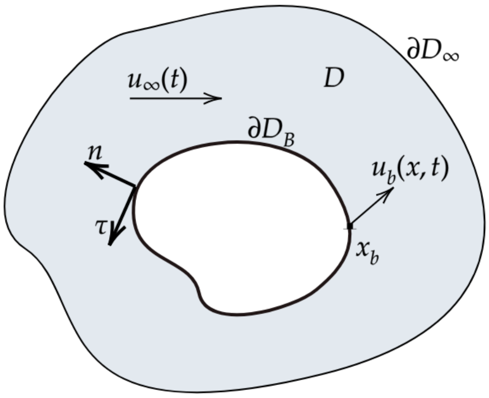

Figure 5.1: Sketch of the fluid domain with the convention used for the body surface orientation.

With an operator splitting approach, equation (5.3) can be solved in two steps. During the first step, the flow is convected with no dissipation as:

$$\frac{D\omega}{Dt} = 0, \tag{5.4}$$

$$\frac{D\mathbf{x}}{Dt} = \mathbf{u}(\mathbf{x}, t), \tag{5.5}$$

where $\mathbf{x} = \mathbf{x}(t)$ is the position of the material point at a given time t. The velocity of advection is given by the kinematics of the flow:

$$\nabla \cdot \mathbf{u} = 0, \quad \nabla \times \mathbf{u} = \boldsymbol{\omega}, \tag{5.6}$$

giving a Poisson equation that links the vorticity with the velocity field:

$$\Delta \mathbf{u} = -\nabla \times \boldsymbol{\omega}. \tag{5.7}$$

The second step consists in the diffusion of the vorticity, governed by the linear heat equation:

$$\frac{D\omega}{Dt}(\mathbf{x}, t) = \nu \Delta \omega(\mathbf{x}, t), \qquad \mathbf{x} \in D, \tag{5.8}$$

$$\nu \frac{\partial \omega}{\partial \mathbf{n}}(\mathbf{x}, t) = -\dot{\gamma}, \qquad \mathbf{x} \in \partial D_B, \tag{5.9}$$

$$\omega(\mathbf{x}, 0) = \omega_0(\mathbf{x}). \tag{5.10}$$

where γ is the circulation density on ∂D_B which is exploited to enforce the no-slip condition on the solid boundary as described in 5.4.2. The Neumann boundary condition (5.9) is exact and its derivation is described in the appendix A. Another relevant point to note is that the operator splitting of Chorin described in the above, which when referred to the vorticity formulation is the so called Chorin-Marsden formula, has been shown to converge to the solution of Navier-Stokes equations in the presence of boundaries only for the case of half space, a result obtained from Benfatto and Pulvirenti (1986). This justifies the use of the flat plate approximation used to solve the diffusion near the boundary as it will be described in section 5.6 resulting in a consistent algorithm.

The action of γ plays a crucial role, since the time derivative of this quantity is related to the formation of the boundary layer on the body surface and, consequently, with the generation and diffusion of vorticity from the surface. As shown in subsection 5.7, the time derivative $\dot{\gamma}$ is related to the tangential pressure gradient on the body; for this reason, it determines boundary layer velocity profiles and consequently possible flow separation.

5.3 PARTICLE APPROXIMATION OF THE VORTICITY FIELD

In the context of vortex methods the vorticity field ω is discretized into vorticity carrying particles. The approximation of the vorticity distribution $\boldsymbol{\omega}$ is performed by discretizing the vorticity into point-vortices:

$$\omega \approx \sum_{i=1}^{N} \Gamma_i \delta(\mathbf{x} - \mathbf{x}_i), \tag{5.11}$$

were Γ_i denotes the weights of the particles which for the case of vorticity correspond to circulations, N is the total number of particles and δ is the two-dimensional Dirac function. In order to obtain a regularized distribution the convolution with a smoothing kernel (cut-off function) ζ_ϵ is applied leading to:

$$\omega_\epsilon(\mathbf{x}) = \omega \star \zeta_\epsilon = \sum_{i=1}^{N} \Gamma_i \zeta_\epsilon(\mathbf{x} - \mathbf{x}_i). \tag{5.12}$$

The smoothing kernel is directly connected with the convergence and conservation properties of vortex methods. According to Majda and Beale (1982) this has to be selected such as:

$$\zeta_\epsilon(x) = \frac{1}{\epsilon^d} \zeta\left(\frac{x}{\epsilon}\right), \quad d = 2, 3, \quad \epsilon > 0, \tag{5.13}$$

$$\int \zeta(x)\, dx = 1, \tag{5.14}$$

$$\int \zeta(x) x^\beta = 0, \quad \forall \quad 0 < |\beta| \leqslant r - 1, \quad \text{with multi-index} \quad \beta, \tag{5.15}$$

$$\int |\zeta(x)||x|^r\, dx < \infty, \tag{5.16}$$

were d is the spacial dimension. The first condition corresponds to a scaling property while the the other properties are moment conditions.

In this method the smoothing function selected is given in Ranucci (1995):

$$\zeta_\epsilon(x) = \frac{2(2 - x^2)}{\pi(1 + x^2)^4}, \tag{5.17}$$

which is a $r = 3$rd-order even kernel.

5.4 VELOCITY EVALUATION AND BOUNDARY CONDITIONS

In the following the evaluation of the velocity field for the advection of the particles is presented along with the enforcement of boundary condition of no-slip. As it will be described the no slip condition is enforced by generating a vortex sheet on the body boundary with circulation density γ.

5.4.1 *Direct formulation*

In order to represent a velocity field it is possible to use the Helmholtz-Hodge Decomposition thus naturally splitting it into a curl-free and a divergence-free component:

$$\mathbf{u} = \mathbf{u}_\infty + \nabla\phi + \nabla \times \psi, \tag{5.18}$$

where ϕ and ψ are given as:

$$\phi(\mathbf{x}) = \int_D \nabla_\mathbf{y} \cdot \mathbf{u}(\mathbf{y}) G(\mathbf{x},\mathbf{y}) dV_y - \int_{\partial D_B} \mathbf{n} \cdot (\mathbf{u} - \mathbf{u}_\infty)(\mathbf{y}) G(\mathbf{x},\mathbf{y})\, dl_y, \tag{5.19}$$

$$\psi(\mathbf{x}) = \int_D \nabla_\mathbf{y} \times \mathbf{u}(\mathbf{y}) G(\mathbf{x},\mathbf{y}) dV_y - \int_{\partial D_B} \mathbf{n} \times (\mathbf{u} - \mathbf{u}_\infty)(\mathbf{y}) G(\mathbf{x},\mathbf{y})\, dl_y, \tag{5.20}$$

where $\mathbf{x} \in D$, $\mathbf{n}$ is the outer normal vector from the fluid, ∂D_B is the body boundary, where:

$$(\mathbf{u} - \mathbf{u}_\infty) = \mathcal{O}\left(\frac{1}{|\mathbf{x}|^{d-1}}\right), \quad d = 2, \tag{5.21}$$

where d is the space dimension, with the vanishing condition at infinity for the integrals to converge and $G(\mathbf{x},\mathbf{y})$ is the Green function for a fluid with domain $D = \mathbb{R}^2$

$$G(\mathbf{x},\mathbf{y}) = \frac{1}{2\pi} \log(|\mathbf{x} - \mathbf{y}|). \tag{5.22}$$

Substituting in equations (5.19), (5.20) the equations governing the kinematics of the flow (5.6) leads to the representation:

$$\phi(\mathbf{x}) = -\int_{\partial D_B} \mathbf{n} \cdot (\mathbf{u} - \mathbf{u}_\infty)(\mathbf{y}) G(\mathbf{x},\mathbf{y})\, dl_y, \tag{5.23}$$

$$\psi(\mathbf{x}) = \int_D \boldsymbol{\omega}(\mathbf{y}) G(\mathbf{x},\mathbf{y}) dV_y - \int_{\partial D_B} \mathbf{n} \times (\mathbf{u} - \mathbf{u}_\infty)(\mathbf{y}) G(\mathbf{x},\mathbf{y})\, dl_y, \tag{5.24}$$

and substituting back in (5.18) the HHD representation of the velocity is obtained:

$$\begin{aligned} \mathbf{u} - \mathbf{u}_\infty = -\nabla \int_{\partial D_B} \mathbf{n} \cdot (\mathbf{u} - \mathbf{u}_\infty)(\mathbf{y}) G(\mathbf{x},\mathbf{y})\, dl_y + \nabla \times \int_D \boldsymbol{\omega}(\mathbf{y}) G(\mathbf{x},\mathbf{y}) dV_y \\ - \nabla \times \int_{\partial D_B} \mathbf{n} \times (\mathbf{u} - \mathbf{u}_\infty)(\mathbf{y}) G(\mathbf{x},\mathbf{y})\, dl_y, \end{aligned} \tag{5.25}$$

From this formulation an explicit representation for the velocity field $\mathbf{u}$ is obtained that is naturally split into a volume, boundary and a far-field (free-stream) term:

$$\mathbf{u} = \mathbf{u}_\omega + \mathbf{u}_\phi + \mathbf{u}_\infty. \tag{5.26}$$

The velocity field $\mathbf{u}$ needs to satisfy the no-through condition. To this end the velocity field $\mathbf{u} - \mathbf{u}_\infty$ needs to satisfy:

$$(\mathbf{u} - \mathbf{u}_\infty) \cdot \mathbf{n} = -\mathbf{u}_\infty \cdot \mathbf{n}. \tag{5.27}$$

Thus substituting into the normal component of (5.25) reads:

$$\begin{aligned}\mathbf{u} - \mathbf{u}_\infty = \int_{\partial D_B} \mathbf{n} \cdot \mathbf{u}_\infty(\mathbf{y}) \nabla G(\mathbf{x}, \mathbf{y}) \, dl_y + \int_D \omega(\mathbf{y}) \nabla \times (\mathbf{k}G)(\mathbf{x}, \mathbf{y}) dV_y \\ - \int_{\partial D_B} \mathbf{n} \times (\mathbf{u} - \mathbf{u}_\infty)(\mathbf{y}) \nabla \times (\mathbf{k}G)(\mathbf{x}, \mathbf{y}) \, dl_y.\end{aligned} \tag{5.28}$$

In a 2D framework $\mathbf{n} \times (\mathbf{u} - \mathbf{u}_\infty) = -(\mathbf{u} - \mathbf{u}_\infty) \cdot \tau$ and:

$$\nabla \times (\mathbf{k}G) = \frac{\partial G}{\partial \tau}\mathbf{n} - \frac{\partial G}{\partial n}\tau, \tag{5.29}$$

thus the last term in (5.28) can be written as:

$$\begin{aligned}-\int_{\partial D_B} \mathbf{n} \times (\mathbf{u} - \mathbf{u}_\infty)(\mathbf{y}) \nabla \times (\mathbf{k}G)(\mathbf{x}, \mathbf{y}) \, dl_y \\ = \int_{\partial D_B} (\mathbf{u} - \mathbf{u}_\infty)(\mathbf{y}) \cdot \tau \left(\frac{\partial G}{\partial \tau}\mathbf{n} - \frac{\partial G}{\partial n}\tau \right) dl_y \\ = -\int_{\partial D_B} (\mathbf{u} - \mathbf{u}_\infty)(\mathbf{y}) \cdot \mathbf{n} \nabla G,\end{aligned} \tag{5.30}$$

and inserting (5.30) into (5.28) the terms containing $\mathbf{u}_\infty$ cancel out leading to:

$$\mathbf{u} - \mathbf{u}_\infty = \int_D \omega(\mathbf{y}) \nabla \times (\mathbf{k}G)(\mathbf{x}, \mathbf{y}) dV_y + \int_{\partial D_B} \tau \cdot \mathbf{u}(\mathbf{y}) \nabla \times G(\mathbf{x}, \mathbf{y}) \, dl_y. \tag{5.31}$$

The first term on the rhs of the above equation is the vorticity induced velocity in the domain that is rewritten as:

$$\mathbf{u} - \mathbf{u}_\infty - \mathbf{u}_\omega = \int_{\partial D_B} \tau \cdot \mathbf{u}(\mathbf{y}) \nabla \times G(\mathbf{x}, \mathbf{y}) \, dl_y. \tag{5.32}$$

Limiting on the boundary using the jump property of the double layer potential for $\mathbf{x} \to \mathbf{y}$ and $\mathbf{x}, \mathbf{y} \in \partial D$ for the singular boundary term reads:

$$\mathbf{u} - \mathbf{u}_\infty - \mathbf{u}_\omega = -\frac{\tau \cdot \mathbf{u}(\mathbf{x})}{2} \times \mathbf{n} + \text{P.V.} \int_{\partial D_B} \tau \cdot \mathbf{u}(\mathbf{y}) \nabla \times (\mathbf{k}G)(\mathbf{x}, \mathbf{y}) \, dl_y, \tag{5.33}$$

where $\mathbf{x}, \mathbf{y} \in \partial D$ and (-) since the boundary is approached from the outside and P.V denotes the principal value of the integral. To enforce the no-slip condition on the velocity field $\mathbf{u}$, it is imposed that:

$$\mathbf{u} \cdot \tau = \mathbf{u}_b \cdot \tau. \tag{5.34}$$

Thus multiplying (5.33) with τ and using (5.29) reads:

$$\frac{\tau(\mathbf{x})\cdot\mathbf{u}(\mathbf{x})}{2}+\text{P.V.}\int_{\partial D_B}\tau(\mathbf{y})\cdot\mathbf{u}(\mathbf{y})\frac{\partial G}{\partial n}(\mathbf{x},\mathbf{y})\,dl_y=(\mathbf{u}_\infty+\mathbf{u}_\omega-\mathbf{u}_b)\cdot\tau(\mathbf{x}), \tag{5.35}$$

where $\mathbf{x}\in\partial D$. Equation (5.35) is a Fredholm integral equation of the second kind. By discretizing it on the body boundary and solving the resulting dense linear system, follows the evaluation of the tangential velocity $\mathbf{u}\cdot\tau$ that is generated in order to enforce the no-slip condition.

However, it is possible to prove using the Fredholm alternative theorem (see *e.g* Kress et al. (1989)) that (5.35) is singular since in multi-connected domains (such as a 2d cylinder in an external flow) it has not a unique solution.

As demonstrated in Koumoutsakos and Leonard (1993) a unique solution can be obtained by assigning an integral constraint on the strength of the vortex sheet that can be found using Kelvin's theorem.

The addition of this constraint augments the number of equations leading to an overdetermined system after the discretization of the boundary integral equation. Such systems can be solved for example using the Least - Square method (see for example Eldredge (2007) for vortex methods), the Singular Value Decomposition method (SVD) or eliminating an equation. SVD is considered very demanding computationally and in DVH an indirect method is used to evaluate the velocity. In Koumoutsakos and Leonard (1993) the problem of the overdetermined system is addressed using spectral decomposition of the kernel to remove the additional equation. However following this technique an additional eigenvalue problem needs to be solved for each boundary curve in the domain.

5.4.2 *Indirect boundary element method*

The representation of the vector field is performed using the Helmholtz - Hodge Decomposition. In this way the velocity field is split into a curl-free and a divergence-free component:

$$\mathbf{u}(\mathbf{x},t)=\nabla\phi+\nabla\times\boldsymbol{\psi}\;=\;\mathbf{u}_\infty(t)+\mathbf{u}_\phi(\mathbf{x},t)+\mathbf{u}_\omega(\mathbf{x},t), \tag{5.36}$$

The curl–free component represents the potential flow part, $\mathbf{u}_\phi$, to which the velocity due to the free stream $\mathbf{u}_\infty(t)$ is added.

In the present work, the free stream velocity is always constant in space, and therefore its integral on any closed loop, and in particular on ∂D_∞, is zero:

$$\Gamma_\infty(t):=\oint_{\partial D_\infty}\mathbf{u}_\infty(t)\cdot d\mathbf{l}\;=\;0, \tag{5.37}$$

The divergence–free component is the rotational part $\mathbf{u}_\omega$ related to the vorticity in the domain D by the solution of the Poisson equation (5.7):

$$\Delta \mathbf{u} = -\nabla \times \boldsymbol{\omega}, \tag{5.38}$$

which for two-dimensional inviscid flow in unbounded space is given by the Biot-Savart law:

$$\mathbf{u}_\omega(\mathbf{x}, t) \; = \int_D \mathbf{K}(\mathbf{x}, \mathbf{y})\omega(\mathbf{y}, t)\, d\mathbf{y}, \qquad \mathbf{K} = \nabla \times (\mathbf{k}G), \tag{5.39}$$

where G is the free–space Green function for the Laplace operator:

$$G(\mathbf{x}, \mathbf{y}) = \frac{1}{2\pi} \log(|\mathbf{x} - \mathbf{y}|), \quad \mathbf{x} \in D = \mathbb{R}^2. \tag{5.40}$$

Eq. (5.39) is the solution of the Poisson equation (5.38) thus the far–field conditions are automatically satisfied, but not the boundary conditions on ∂D.

The term $\mathbf{u}_\phi$ corresponds to the irrotational part and can be expressed through an Indirect Boundary Integral Equation (IBIE) formulation. The boundary condition on ∂D is enforced by means of this velocity component, as explained in the following.

The body surface is represented by a distribution of elementary sources σ and circulation densities γ. Then $\mathbf{u}_\phi$ is evaluated as:

$$\mathbf{u}_\phi(\mathbf{x}, t) \; = - \int_{\partial D_B} \sigma(\mathbf{y}, t) \nabla G(\mathbf{x}, \mathbf{y}) \; dl_y + \int_{\partial D_B} \gamma(\mathbf{y}, t) \mathbf{K}(\mathbf{x}, \mathbf{y}) \; dl_y. \tag{5.41}$$

The distribution of circulation density is linked to the total circulation Γ given by the vorticity in D:

$$\Gamma(t) = \int_D \omega(\mathbf{y}, t)\, d\mathbf{y} \; = -\oint_{\partial D_B} \gamma(\mathbf{y}, t)\, dl_y \; + \Gamma_\infty(t) \tag{5.42}$$

In equation (5.41) the sources and the circulation density distribution are both unknown. In order to evaluated them separately, in the first step the distribution of γ is assumed constant and equal to

$$\gamma(\mathbf{y}, t) = \hat{\gamma}(t) \; = -\left[\Gamma(t) - \Gamma_\infty(t)\right] / \mathcal{P}, \tag{5.43}$$

where $\mathcal{P}$ is the perimeter of the body. Thus $\hat{\gamma}$ is the instantaneous circulation around the body contour. Substituting the above relation in (5.41) we obtain:

$$\mathbf{u}'_\phi(\mathbf{x}, t) \; = - \int_{\partial D_B} \sigma(\mathbf{y}, t) \nabla G(\mathbf{x}, \mathbf{y})\, dl_y \; + \hat{\gamma}(t) \int_{\partial D_B} \mathbf{K}(\mathbf{x}, \mathbf{y})\, dl_y. \tag{5.44}$$

The no-through condition on the body surface is enforced by considering the following condition:

$$\mathbf{u} \cdot \mathbf{n} = \mathbf{u}_b \cdot \mathbf{n}. \tag{5.45}$$

By enforcing it on the body surface with the velocity decomposition given by the HHD in (5.36), the projection of $\mathbf{u}'_\phi$ along the normal on ∂D_B reads:

$$\mathbf{u}'_\phi \cdot \mathbf{n} \;=\; \left(\mathbf{u}_b - \mathbf{u}_\infty - \mathbf{u}_\omega\right) \cdot \mathbf{n}. \tag{5.46}$$

The expression of $\mathbf{u}'_\phi \cdot \mathbf{n}$ on the boundary is evaluated by taking the projection of 5.44 along the normal direction to the body:

$$\mathbf{u}'_\phi(\mathbf{x}, t) \cdot \mathbf{n} = -\int_{\partial D_B} \sigma(\mathbf{y}, t)\mathbf{n}(\mathbf{y})\nabla G(\mathbf{x}, \mathbf{y})\, dl_y \;+\; \hat{\gamma}(t) \int_{\partial D_B} \mathbf{n}(\mathbf{y})\mathbf{K}(\mathbf{x}, \mathbf{y})\, dl_y. \tag{5.47}$$

The kernel $\mathbf{K}$ in 2D can be written as:

$$\mathbf{K} = \nabla^\perp G = \nabla \times (\mathbf{k}G) = \frac{\partial G}{\partial \tau}\mathbf{n} - \frac{\partial G}{\partial n}\boldsymbol{\tau}, \tag{5.48}$$

thus 5.47 becomes

$$\mathbf{u}'_\phi(\mathbf{x}, t) \cdot \mathbf{n} = -\int_{\partial D_B} \sigma(\mathbf{y}, t)\mathbf{n}(\mathbf{y})\nabla G(\mathbf{x}, \mathbf{y})\, dl_y \;+\; \hat{\gamma}(t) \int_{\partial D_B} \mathbf{n}(\mathbf{y})\mathbf{K}(\mathbf{x}, \mathbf{y})\, dl_y \tag{5.49}$$

$$= -\int_{\partial D_B} \sigma(\mathbf{y}, t)\mathbf{n}(\mathbf{y})\nabla G(\mathbf{x}, \mathbf{y})\, dl_y \;+\; \hat{\gamma}(t) \int_{\partial D_B} \mathbf{n}(\mathbf{y}) \left[\frac{\partial G}{\partial \tau}\mathbf{n} - \frac{\partial G}{\partial n}\tau\right] dl_y \tag{5.50}$$

$$= -\int_{\partial D_B} \sigma(\mathbf{y}, t)\mathbf{n}(\mathbf{y})\nabla G(\mathbf{x}, \mathbf{y})\, dl_y \;+\; \hat{\gamma}(t) \int_{\partial D_B} \boldsymbol{\tau}(\mathbf{y})\nabla G(\mathbf{x}, \mathbf{y})\, dl_y. \tag{5.51}$$

In order to obtain an expression on the boundary a limiting procedure needs to be considered for $\mathbf{x} \to \mathbf{y}$ thus:

$$\mathbf{u}'_\phi(\mathbf{x}, t) \cdot \mathbf{n} = -\lim_{\mathbf{x}\to\mathbf{y}} \left(\int_{\partial D_B} \sigma(\mathbf{y}, t)\mathbf{n}(\mathbf{y})\nabla G(\mathbf{x}, \mathbf{y})\, dl_y\right) + \lim_{\mathbf{x}\to\mathbf{y}} \left(\hat{\gamma}(t) \int_{\partial D_B} \boldsymbol{\tau}(\mathbf{y})\nabla G(\mathbf{x}, \mathbf{y})\, dl_y\right). \tag{5.52}$$

The integral kernels become singular for $\mathbf{x} \to \mathbf{y}$ when both $\mathbf{x}, \mathbf{y} \in \partial D_B$. In particular the terms to be considered are:

$$\mathbf{n}(\mathbf{y})\nabla G(\mathbf{x}, \mathbf{y}) = \frac{\partial G}{\partial n}(\mathbf{x}, \mathbf{y}) = \frac{1}{2\pi}\frac{(\mathbf{x} - \mathbf{y}) \cdot \mathbf{n}}{|\mathbf{x} - \mathbf{y}|^2}, \tag{5.53}$$

$$\boldsymbol{\tau}(\mathbf{y})\nabla G(\mathbf{x}, \mathbf{y}) = \frac{\partial G}{\partial \tau}(\mathbf{x}, \mathbf{y}) = \frac{1}{2\pi}\frac{(\mathbf{x} - \mathbf{y}) \cdot \boldsymbol{\tau}}{|\mathbf{x} - \mathbf{y}|^2}, \tag{5.54}$$

which hold for $\mathbf{x} \in D$, $\mathbf{y} \in \partial D_B$, while when $\mathbf{x} \to \mathbf{y}$ with $\mathbf{x}$, $\mathbf{y} \in \partial D_B$ they become singular. The singularity can be treated using the following jump properties (see *e.g.* Mikhlin (2014)):

$$\lim_{\mathbf{x}\to\mathbf{y}} \left(\int_{\partial D_B} \sigma(\mathbf{y}, t)\mathbf{n}(\mathbf{y})\nabla G(\mathbf{x}, \mathbf{y})\, dl_y\right) = \frac{\sigma(\mathbf{x}, t)}{2} + \text{P.V.}\int_{\partial D_B} \sigma(\mathbf{y}, t)\mathbf{n}(\mathbf{y})\nabla G(\mathbf{x}, \mathbf{y})\, dl_y, \tag{5.55}$$

$$\lim_{\mathbf{x}\to\mathbf{y}}\left(\hat{\gamma}(t)\int_{\partial D_B}\boldsymbol{\tau}(\mathbf{y})\nabla G(\mathbf{x},\mathbf{y})\,dl_y\right) = \hat{\gamma}(t)\,\text{P.V.}\int_{\partial D_B}\boldsymbol{\tau}(\mathbf{y})\nabla G(\mathbf{x},\mathbf{y})\,dl_y, \quad (5.56)$$

where the integrals on the rhs are understood in the sense of the Cauchy principal value denoted with P.V. Inserting equations (5.55), (5.56) into (5.52) results in:

$$\begin{aligned}\mathbf{u}'_\phi(\mathbf{x},t)\cdot\mathbf{n} = -\frac{\sigma(\mathbf{x},t)}{2} - \text{P.V.}\int_{\partial D_B}\sigma(\mathbf{y},t)\mathbf{n}(\mathbf{y})\nabla G(\mathbf{x},\mathbf{y})\,dl_y + \\ \hat{\gamma}(t)\,\text{P.V.}\int_{\partial D_B}\boldsymbol{\tau}(\mathbf{y})\nabla G(\mathbf{x},\mathbf{y})\,dl_y, \quad \text{on} \quad \partial D_B. \quad (5.57)\end{aligned}$$

Finally, the no-through condition is enforced on the body boundary by inserting (5.57) into (5.46) leading to the following Fredholm integral equation of the second kind:

$$\begin{aligned}\frac{\sigma(\mathbf{x},t)}{2} + \text{P.V.}\int_{\partial D_B}\sigma(\mathbf{y},t)\mathbf{n}(\mathbf{y})\nabla G(\mathbf{x},\mathbf{y})\,dl_y = \\ \hat{\gamma}(t)\,\text{P.V.}\int_{\partial D_B}\boldsymbol{\tau}(\mathbf{y})\nabla G(\mathbf{x},\mathbf{y})\,dl_y - [(\mathbf{u}_b - \mathbf{u}_\infty - \mathbf{u}_\omega)(\mathbf{x},t)]\cdot\mathbf{n}(\mathbf{x}). \quad (5.58)\end{aligned}$$

Solving the above equation provides the distribution of sources on the boundary for which the no-through condition is satisfied. Then the velocity field satisfying only the no-through condition is obtained:

$$\begin{aligned}\mathbf{u}(\mathbf{x},t) &= \mathbf{u}_\infty(t) - \mathbf{u}'_\phi(\mathbf{x},t) + \mathbf{u}_\omega(\mathbf{x},t), && (5.59)\\ &= \mathbf{u}_\infty(t) - \int_{\partial D_B}\sigma(\mathbf{y})\nabla G(\mathbf{x},\mathbf{y})\,dl_y + \hat{\gamma}(t)\int_{\partial D_B}\mathbf{K}(\mathbf{x},\mathbf{y})\,dl_y + \mathbf{u}_\omega(\mathbf{x},t). && (5.60)\end{aligned}$$

After the computation of the sources, the γ distribution is computed by enforcing the no-slip condition following the procedure in Chorin (1978) as follows.

The non-satisfaction of the full no slip condition by the total velocity field on the boundary will create, due to the existence of viscosity, a slip velocity. This will be equal to the jump of the tangential velocity from its value in the interior of the fluid $\mathbf{u}$ given by (5.60) to its value on the boundary $\mathbf{u}_b$. To cancel this slip velocity a vortex sheet of the same intensity needs to be created on the boundary with circulation density γ. This vortex sheet will be discretized into vortex particles on the body boundary canceling the slip velocity.

Thus we are interested in evaluating the quantity:

$$\begin{aligned}\gamma &= \mathbf{u}_b\cdot\boldsymbol{\tau} - \mathbf{u}\cdot\boldsymbol{\tau} && (5.61)\\ &= \mathbf{u}_b\cdot\boldsymbol{\tau} - \left(\mathbf{u}_\infty + \mathbf{u}'_\phi + \mathbf{u}_\omega\right)\cdot\boldsymbol{\tau}, \quad \text{on} \quad \partial D_B && (5.62)\end{aligned}$$

with $\mathbf{u}$ given by (5.60). The expression for the term $\mathbf{u}'_\phi \cdot \boldsymbol{\tau}$ in the above equation (5.62) can be found as follows. By taking the projection of equation (5.41) along the tangential direction to the body:

$$\mathbf{u}'_\phi(\mathbf{x},t)\cdot\boldsymbol{\tau} = -\int_{\partial D_B} \sigma(\mathbf{y},t)\boldsymbol{\tau}(\mathbf{y})\nabla G(\mathbf{x},\mathbf{y})\, dl_y + \hat{\gamma}(t)\int_{\partial D_B} \boldsymbol{\tau}(\mathbf{y})\mathbf{K}(\mathbf{x},\mathbf{y})\, dl_y, \quad (5.63)$$

and using relation (5.48) we obtain:

$$\mathbf{u}'_\phi(\mathbf{x},t)\cdot\boldsymbol{\tau} = -\int_{\partial D_B} \sigma(\mathbf{y},t)\boldsymbol{\tau}(\mathbf{y})\nabla G(\mathbf{x},\mathbf{y})\, dl_y - \hat{\gamma}(t)\int_{\partial D_B} \mathbf{n}(\mathbf{y})\nabla G(\mathbf{x},\mathbf{y})\, dl_y. \quad (5.64)$$

Again the integral kernels become singular for points on the boundary thus using the analogous expressions of the equations (5.55) and (5.56) we obtain:

$$\begin{aligned}\mathbf{u}'_\phi(\mathbf{x},t)\cdot\boldsymbol{\tau} = -\text{P.V.}\int_{\partial D_B} &\sigma(\mathbf{y})\boldsymbol{\tau}(\mathbf{y})\nabla G(\mathbf{x},\mathbf{y})\, dl_y \\ &-\frac{\hat{\gamma}(t)}{2} - \hat{\gamma}(t)\,\text{P.V.}\int_{\partial D_B} \mathbf{n}(\mathbf{y})\nabla G(\mathbf{x},\mathbf{y})\, dl_y. \quad (5.65)\end{aligned}$$

Finally inserting (5.65) into (5.62) it is possible to obtain the following expression for the unknown circulation density:

$$\begin{aligned}\gamma = \frac{\hat{\gamma}(\mathbf{y})}{2} + \text{P.V.}\int_{\partial D_B} &\hat{\gamma}(\mathbf{y})\mathbf{n}(\mathbf{y})\nabla G(\mathbf{x},\mathbf{y})\, dl_y \\ +\text{P.V.}\int_{\partial D_B} &\sigma(\mathbf{y})\boldsymbol{\tau}(\mathbf{y})\nabla G(\mathbf{x},\mathbf{y})\, dl_y - (\mathbf{u}_b - \mathbf{u}_\infty - \mathbf{u}_\omega)(\mathbf{x})\cdot\boldsymbol{\tau}(\mathbf{x}). \quad (5.66)\end{aligned}$$

The solution to the equations (5.58) and (5.66) is carried out by a Boundary Element Method (BEM), the body boundary ∂D_B being discretised by panels. For example the body can be subdivided in N_b panels the σ distribution can be assumed to be constant on each of them. Therefore, eq. (5.58) can be rewritten as an algebraic system:

$$\mathbb{A}_{ij}\,\sigma_j = [\mathbf{u}_{bj} - \mathbf{u}_\infty]\cdot\mathbf{n}_j - \mathbf{u}_{\omega j}\cdot\mathbf{n}_j + \mathbb{B}_{ij}\,\hat{\gamma}_j, \quad (5.67)$$

where $\mathbb{A}$ and $\mathbb{B}$ are matrices $N_b \times N_b$. The unknown vector σ_j can be evaluated by the system (5.67) while $\hat{\gamma}_j$ is a vector where all the N_b elements are equal to $\hat{\gamma}$ evaluated with (5.43). The $N_p \times N_p$ linear system is solved using LDU decomposition and provides σ.

Similarly using a BEM the equation (5.66) can be rewritten after the discretization in panels as:

$$\gamma_j = [\mathbf{u}_{bj} - \mathbf{u}_\infty]\cdot\boldsymbol{\tau}_j - \mathbf{u}_{\omega j}\cdot\boldsymbol{\tau}_j + \mathbb{A}_{ij}\hat{\gamma}_j + \mathbb{B}_{ij}\,\sigma_j\,. \quad (5.68)$$

The integrals are discretized by the Nyström method with the generalized trapezoidal rule (for details see Rossi et al. (2015a)).

Once source and circulation densities are computed, $\mathbf{u}_\phi$ is evaluated by equation (5.41) and the velocity field $\mathbf{u}(\mathbf{x}, t)$ is calculated as:

$$\mathbf{u}(\mathbf{x}, t) = \mathbf{u}_\infty(t) + \int_{\partial D_B} \Big[\mathbf{K}(\mathbf{x}, \mathbf{y})\gamma(\mathbf{y}) - \mathbf{k} \times \mathbf{K}(\mathbf{x}, \mathbf{y})\sigma(\mathbf{y})\Big] \, dl_y + \int_D \mathbf{K}(\mathbf{x}, \mathbf{y})\omega(\mathbf{y}) \, d\mathbf{y} \,. \tag{5.69}$$

Vorticity is then advected with the computed velocity field.

5.5 FAST MULTIPOLE METHOD FOR THE VELOCITY

The evaluation of the velocity field in order to advect the particles given by (5.69) requires $\mathcal{O}(N_v^2)$ multiplications for the domain integral, where N_v is the number of vortex particles. The matrices resulting from the discretization lead to a dense linear system. To avoid the quadratic cost of the evaluation of the domain integral, the evaluation of the velocity from the vorticity is performed using a Fast Multipole Method (FMM). In the DVH method, the FMM proposed in Ranucci (1995) is used which results in a $\mathcal{O}(N \log N)$ algorithm, using a Barnes - Hut tree code.

Considering the rotational part of the velocity field in (5.69), induced by vorticity:

$$\mathbf{u}_\omega(\mathbf{x}, t) = \int_D \mathbf{K}(\mathbf{x}, \mathbf{y})\omega(\mathbf{y}) \, d\mathbf{y}, \tag{5.70}$$

it is written in a discrete form for N-vortices as:

$$\mathbf{u}_\omega(\mathbf{x}_i, t) = \sum_{j=1}^{N} \Gamma_j \mathbf{K}_\epsilon(\mathbf{x}_i, \mathbf{y}_i), \tag{5.71}$$

this can be recast in complex variables as:

$$V(z) = \frac{1}{2\pi i} \sum_{j=1}^{N} \frac{\Gamma_j}{z - z_j}, \tag{5.72}$$

where $z = x + iy$, $V = \mathbf{u} - i\mathbf{v}$.

This computation will be $\mathcal{O}(N^2)$. To avoid this the spacial distribution of the vortices is taken into account. To this end, vortices that are close together and thus forming a group/cluster need not to be computed in a direct way w.r.t. a particle. Instead, their contribution can be approximated by a finite number of multipole expansions obtained by rewriting (5.72) as a Laurent series expansion around a particle located at z_0 or a cluster of particles with center of mass at z_G.

5.5.1 *Particle to multipole*

Denote with z_G the location of the center of the group of particles. Then adding and subtracting z_G from the denominator of (5.72) this can be rewritten as:

$$V(z) = \frac{1}{2\pi i}\sum_{j=1}^{N} \frac{\Gamma_j}{z - z_G + z_G - z_j} = \frac{1}{2\pi i(z - z_G)}\sum_{j=1}^{N} \frac{\Gamma_j}{1 - \frac{z_j - z_G}{z - z_G}}, \tag{5.73}$$

which is the velocity induced by the cluster located at z_G. It is known that for $|x| < 1$ the geometric series $\sum_{k=0}^{\infty} x^k$ is absolutely convergent and it can thus be written as:

$$\sum_{k=0}^{\infty} x^k = \frac{1}{1-x}. \tag{5.74}$$

Thus (5.73) for $|\frac{z_j - z_G}{z - z_G}| < 1$ can be expanded as a Laurent series in the following way:

$$\begin{aligned} V(z) &= \frac{1}{2\pi i(z - z_G)}\sum_{j=1}^{N} \frac{\Gamma_j}{1 - \frac{z_j - z_G}{z - z_G}} \\ &= \frac{1}{2\pi i(z - z_G)}\sum_{j=1}^{N}\sum_{k=0}^{\infty} \Gamma_j \left(\frac{z_j - z_G}{z - z_G}\right)^k \\ &= \frac{1}{2\pi i(z - z_G)}\sum_{k=0}^{\infty} \frac{\sum_{j=1}^{N} \Gamma_j (z_j - z_G)^k}{(z - z_G)^k} \\ &= \frac{1}{2\pi i(z - z_G)}\sum_{k=0}^{\infty} \frac{c_k}{(z - z_G)^k}, \end{aligned} \tag{5.75}$$

where $c_k = \sum_{j=1}^{N} \Gamma_j (z_j - z_G)^k$ are the moments of vorticity for the current cluster. Truncating the expansion at order $k = k_{max}$ leads finally to the desired approximation and in DVH method $k_{max} = 20$ as suggested in Rossi (2014).

There is the possibility that particles can belong to a cluster (child) and that cluster itself to a greater cluster (parent) etc. Then the k-moments of a particle w.r.t. the two clusters which correspond to the coefficients c_k, should be evaluated 2 times (one for each cluster or more if more clusters exist). This could render the above procedure to reduce the computational cost, inefficient. As a solution, the coefficients evaluated for the child cluster can be used to evaluate the coefficients of the parent cluster. This is achieved by translating the center of the multipole expansion of the child cluster to that of the parent cluster as follows.

5.5.2 *Translation - Child to parent*

Let z_{G_c} and z_{G_p} be the centres of the child and parent clusters respectively. The translation is performed by expanding the expression (5.75) for the child cluster

z_{G_c} into a Taylor series centered at the parent cluster center z_{G_p}. Starting from (5.75) we have that:

$$
\begin{aligned}
V(z) &= \frac{1}{2\pi i(z - z_{G_p})} \sum_{k=0}^{\infty} \frac{c_k}{(z - z_{G_p})^k} \\
&= \frac{1}{2\pi i} \sum_{k=0}^{\infty} \frac{c_k}{(z - z_{G_p})^{k+1}} \\
&= \frac{1}{2\pi i} \sum_{k=0}^{\infty} \frac{c_k}{(z - z_{G_p} + z_{G_c} - z_{G_c})^{k+1}} \\
&= \frac{1}{2\pi i(z - z_{G_c})} \sum_{k=0}^{\infty} \frac{c_k}{\left(1 - \frac{z_{G_p} - z_{G_c}}{z - z_{G_c}}\right)^{k+1}}.
\end{aligned}
\tag{5.76}
$$

For the term $\left(1 - \frac{z_{G_p} - z_{G_c}}{z - z_{G_c}}\right)^{-(k+1)}$ the following expression can be used, possible to obtain using the binomial theorem:

$$
\frac{1}{(x - x_0)^k} = \sum_{m=k}^{\infty} \binom{m-1}{k-1} \frac{x_0^{m-k}}{x^m}.
\tag{5.77}
$$

Using expression (5.77) into (5.76) leads to:

$$
V(z) = \frac{1}{2\pi i(z - z_{G_c})} \sum_{k=0}^{\infty} c_k \sum_{m=k}^{\infty} \binom{m}{k} \frac{\left(z_{G_p} - z_{G_c}\right)^{m-k}}{(z - z_{G_c})^m}.
\tag{5.78}
$$

Using the property of the binomial coefficients $\binom{m}{k} = 0$ for every $k > m$ the inner summation can start at $k = 0$ and then due to the fact that the series is convergent the order of summation can be changed leading to:

$$
\begin{aligned}
V(z) &= \frac{1}{2\pi i(z - z_{G_c})} \sum_{k=0}^{\infty} c_k \sum_{m=k}^{\infty} \binom{m}{k} \frac{\left(z_{G_p} - z_{G_c}\right)^{m-k}}{(z - z_{G_c})^m} \\
&= \frac{1}{2\pi i(z - z_{G_c})} \sum_{m=0}^{\infty} c_k \sum_{k=0}^{\infty} \binom{m}{k} \frac{\left(z_{G_p} - z_{G_c}\right)^{m-k}}{(z - z_{G_c})^m}.
\end{aligned}
\tag{5.79}
$$

Finally, using again the binomial coefficient property the inner sum can be truncated at $k = m$ giving thus:

$$
\begin{aligned}
V(z) &= \frac{1}{2\pi i(z - z_{G_c})} \sum_{m=0}^{\infty} c_k \sum_{k=0}^{m} \binom{m}{k} \frac{\left(z_{G_p} - z_{G_c}\right)^{m-k}}{(z - z_{G_c})^m} \\
&= \frac{1}{2\pi i(z - z_{G_c})} \sum_{m=0}^{\infty} \frac{c_{k_p}}{(z - z_{G_c})^m},
\end{aligned}
\tag{5.80}
$$

where the coefficients are given as:

$$c_{k_p} = \sum_{k=0}^{m} c_k \binom{m}{k} (z_{G_p} - z_{G_c})^{m-k}. \tag{5.81}$$

Thus the coefficients c_{k_p} can be evaluated exactly from the coefficients c_k.

The final step for the construction of the above fast multipole algorithm is to couple the above procedure with a tree-data structure for the particles and the clusters, in order to provide a criterion of when the expansions or the direct computation of the velocity should be used. The tree-data structure is created by sub-dividing the computational domain into sub-domains forming a quad-tree in 2D or an oct-tree in 3D. At the lowest level of division, the tree corresponds to the whole computational domain while its leaves correspond to the subdomains.

5.6 DIFFUSION

Operator splitting allows treating diffusion in a separate way from advection. Here a deterministic approach is followed based on the exact solution of the diffusion equation for the vorticity ω with initial conditions for a fluid confined in space D:

$$\omega_t = \nu \Delta \omega, \quad \text{in} \quad D \times [0, t], \tag{5.82}$$

$$\omega(\mathbf{x}, 0) = \omega_0(\mathbf{x}), \quad \text{in} \quad D. \tag{5.83}$$

For the case of diffusion in free space this is performed by considering the diffusion of one vortex particle using the analytical solution of the heat equation:

$$\omega(\mathbf{x}, t) = \Gamma G_\nu(\mathbf{x}, \mathbf{y}; t, s) = \frac{1}{4\pi\nu(t - t_0)} \exp\left(-\frac{|\mathbf{x} - \mathbf{y}|^2}{4\nu(t - t_0)}\right). \tag{5.84}$$

The Gaussian distribution results in a infinite support for the vorticity. This requires the introduction of a finite support for numerical computations, within which diffusion is performed. This is achieved by the introduction of a *diffusive radius* R_d and thus the discrete approximations take the following form:

$$\omega(\mathbf{x}, t_0 + \Delta t_d) = \begin{cases} \Gamma_i \frac{1}{4\pi\nu\Delta t_d} \exp\left(-\frac{|\mathbf{x} - \mathbf{x}_i|^2}{4\nu\Delta t_d}\right), & |\mathbf{x} - \mathbf{x}_i| \leqslant R_d, \\ 0, & |\mathbf{x} - \mathbf{x}_i| > R_d, \end{cases} \tag{5.85}$$

for the approximation in free space where Δt_d is the diffusion time step. This truncation introduces an error in the conservation of the circulation equal to:

$$\xi = \left| \frac{\Gamma(t_0 + \Delta t_d) - \Gamma_0}{\Gamma_0} \right| = \exp\left(-\frac{R_d^2}{4\nu\Delta t_d}\right), \tag{5.86}$$

and thus a redistribution procedure of circulation is performed to conserve it.

For the case of diffusion near a boundary the general solution of the heat equation can be expressed in integral form (see *e.g* Morse and Feshbach (1953)):

$$\omega(\mathbf{x},t) = -\nu \int_{t_0}^{t} \int_{\partial D_B} \left[G_\nu(\mathbf{x},\mathbf{y};t,s) \frac{\partial \omega}{\partial \mathbf{n}}(\mathbf{y},t) - \omega(\mathbf{y},t) \frac{\partial G_\nu}{\partial \mathbf{n}}(\mathbf{x},\mathbf{y};t,s) \right] d\mathbf{y}ds + \int_D \omega(\mathbf{y},t_0) G_\nu(\mathbf{x},\mathbf{y};t,t_0) d\mathbf{y}, \quad (5.87)$$

where G_ν is the heat kernel:

$$G_\nu(\mathbf{x},\mathbf{y};t,s) = \frac{1}{(4\pi\nu(t-s))} \exp\left(-\frac{|\mathbf{x}-\mathbf{y}|^2}{4\nu(t-s)} \right), \quad \text{for} \quad t > s. \quad (5.88)$$

Following Ranucci (1995), enforcing a homogeneous Neumann boundary condition in equation (5.87), which expresses the reflection of the vorticity near the boundary into the domain, the solution can be reduced in the form:

$$\omega(\mathbf{x},t) = \nu \int_{t_0}^{t} \int_{\partial D_B} \omega(\mathbf{y},t) \frac{\partial G_\nu}{\partial \mathbf{n}}(\mathbf{x},\mathbf{y};t,s) d\mathbf{y}ds + \int_D \omega(\mathbf{y},t_0) G_\nu(\mathbf{x},\mathbf{y};t,t_0) d\mathbf{y}. \quad (5.89)$$

By limiting on the boundary equation (5.89) and using the jump property of the double layer potential (see Kress et al. (1989)) we get the following integral equation for the unknown value of the ω on ∂D:

$$\frac{1}{2}\omega(\mathbf{x},t) = \int_{t_0}^{t} \int_{\partial D_B} \omega(\mathbf{y},t) \frac{\partial G_\nu}{\partial \mathbf{n}}(\mathbf{x},\mathbf{y};t,s) d\mathbf{y}ds + \int_D \omega(\mathbf{y},t_0) G_\nu(\mathbf{x},\mathbf{y};t,t_0) d\mathbf{y}, \quad \text{for} \quad \mathbf{x} \in \partial D. \quad (5.90)$$

Thus in order to find the value of ω on the boundary, a boundary integral equation needs to be solved for the unknown vorticity on ∂D. This approach requires taking local approximations of the boundary curve, can be computationally expensive and less accurate for vanishing viscosity (see for example Ranucci (1995) or Koumoutsakos et al. (1994)). To avoid such problems, an alternative evaluation to (5.89) can be found by selecting a Green function that satisfies a homogeneous Neumann boundary condition:

$$\frac{\partial G_\nu}{\partial \mathbf{n}} = 0, \quad (5.91)$$

thus equation (5.89) becomes:

$$\omega(\mathbf{x},t) = \int_D \omega(\mathbf{y},t_0) G_\nu^D(\mathbf{x},\mathbf{y};t,t_0) d\mathbf{y}, \quad (5.92)$$

where G_ν^D is the domain dependent heat kernel. Having done this selection, the problem now is to determine the domain dependent Green function G_ν^D. It is known that Green functions have a closed form only for very few cases if some spatial symmetries are taken into account. In this work the domain is considered to be the half-space, thus the boundary is taken into account by a flat plate approximation and the solution is obtained using the image method. Then, following the principle of the superposition of the solutions of the heat equation, the diffusion of a vortex in the presence of a flat plate can be taken into account by placing a vortex symmetrically to it w.r.t. the boundary. Thus the diffusion of a vortex particle near the boundary will be the superposition of the diffusion in free space of two symmetrically placed vortex particles resulting in the Green function G_ν^D being:

$$\begin{aligned} G_\nu^D(\mathbf{x},\mathbf{y};t,s) &= G_\nu(\mathbf{x},\mathbf{y};t,s) + G_\nu(\mathbf{x},\mathbf{y}^{im};t,s) \\ &= \frac{1}{4\pi\nu(t-s)}\exp\left(-\frac{|\mathbf{x}-\mathbf{y}|^2}{4\nu(t-s)}\right) + \frac{1}{4\pi\nu(t-s)}\exp\left(-\frac{|\mathbf{x}-\mathbf{y}^{im}|^2}{4\nu(t-s)}\right). \end{aligned} \tag{5.93}$$

By applying the procedure described above, the diffusion of a vortex particle close to the boundary at position $\mathbf{x}$ and with circulation Γ is performed by placing an image vortex symmetrically to it w.r.t. the boundary. By introducing again the diffusive radius R_d, equation (5.93) is written as:

$$\begin{aligned} &\boldsymbol{\omega}(\mathbf{x},t_0+\Delta t_d) = \\ &\begin{cases} \Gamma_i\dfrac{1}{4\pi\nu\Delta t_d}\left[\exp\left(-\dfrac{|\mathbf{x}-\mathbf{x}_i|^2}{4\nu\Delta t_d}\right)+\exp\left(-\dfrac{|\mathbf{x}-\mathbf{x}_i^{im}|^2}{4\nu\Delta t_d}\right)\right], & |\mathbf{x}-\mathbf{x}_i|\leqslant R_d, \\ 0, & |\mathbf{x}-\mathbf{x}_i| > R_d, \end{cases} \end{aligned} \tag{5.94}$$

5.6.1 *Treatment of Lagrangian Distortion during Diffusion*

In the vortex method DVH the problem of Lagrangian distortion is addressed during the diffusion step. To prevent particle clustering and depletion, the diffusion of each vortex is performed on a Regular Point Distribution (RPD). This RPD is a set of equidistantly distributed nodes. Close to the boundary, they are placed in a body-fitted configuration, generated by an algorithm introduced in Colagrossi et al. (2012). Far from the boundary these nodes are placed in a Cartesian configuration.

Consider only the diffusion of one vortex particle. Then according to the process of the diffusion discussed in the previous section, the diffusion is performed using the fundamental solution of the heat equation with initial condition a single particle that at initial time t_0 has circulation Γ_i and is at position $\mathbf{x}_i$, then:

$$\omega(\mathbf{x},t) = \Gamma_i\frac{1}{4\pi\nu(t-t_0)}\exp\left(-\frac{|\mathbf{x}-\mathbf{x}_i|^2}{4\nu(t-t_0)}\right). \tag{5.95}$$

To proceed with the diffusion, the points within $|x-x_i|\leqslant R_d$ are found according to (5.85). Then circulation is diffused on the nodes of the RPD using this approximate solution of the heat equation. After this process of diffusion in order

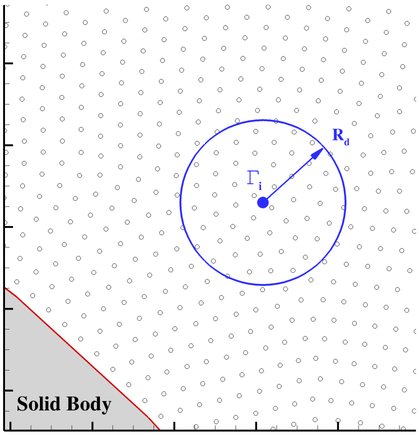

Figure 5.2: Diffusion of a vortex particle with circulation Γ_i within the diffusion radius R_d. The blue dot is the vortex particle, the grey nodes correspond to the Regular Point Distribution.

to conserve circulation a redistribution of circulation follows. After the diffusion is done for every particle then the nodes of the RPD will become the new vortices. In this way a regular vortex particle distribution is always provided in order to prevent the Lagrangian distortion.

Due to the linearity of the diffusion equation the diffusion is concluded by the superposition of the contributions of N_ν vortices with circulation Γ_i, $i = 1, \cdots N_\nu$.

5.6.2 *Diffusion near geometric singularities*

In the presence of geometrical singularities on the boundary, the flat plate approximation is not valid. A solution to this problem is the use of the so called *visibility mask*. Details on the algorithm can be found in Rossi et al. (2016).

When a vortex particle is close to an edge of the body, it diffuses only in the area less or equal to the diffusive radius R_d, with the exception of the shaded region. The shaded region is defined by the line that connects the center of the vortex with the edge as it can be seen in figure 5.3a.

Let $\mathbf{x}_i$ be the position of the vortex with circulation Γ_i, then the set of the RPD points selected by the visibility mask will be the set $B^{vis}_{\mathbf{x}_i}$. As previously described, the diffusion close to the boundary is performed by placing an image vortex symmetrically to the vortex with respect to the boundary. The definition of the $B^{vis}_{\mathbf{x}_i}$ set depends on the distance of the vortex from the singularity and from this follows also the relative position of the image vortex.

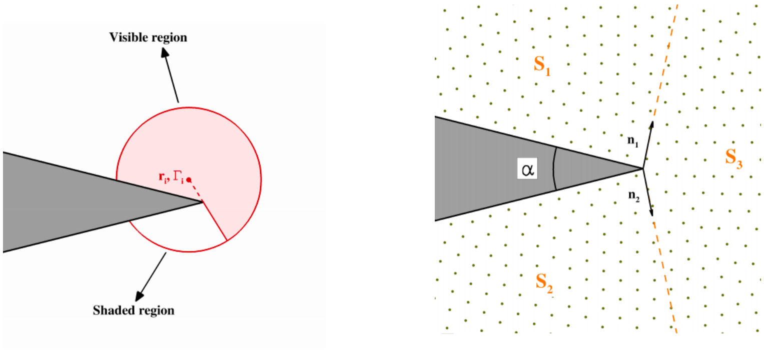

(a) The visible and shaded region used in the visibility mask algorithm (Rossi et al., 2016).

(b) Definition of the regions S_1, S_2 ,S_3 in which the computational domain is divided in the vicinity of singularity (Rossi et al., 2016).

Figure 5.3: Description of the visibility mask.

To this end the computational domain near the singularity is divided into three regions S_1, S_2, S_3. These regions are defined by the unit, normal to the body boundary vectors $\mathbf{n}_1$, $\mathbf{n}_2$ as it can be seen in figure 5.3b.

The possible configurations of the vortex and the image vortex in these regions are depicted in figure 5.4. As it can be seen in this figure, the diffusive support of the vortex $B^{vis}_{\mathbf{x}_i}$ is the red zone and is the region in which the vortex diffuses. Correspondingly, the diffusive support of the image vortex $B^{vis}_{\mathbf{x}_i^{im}}$ is the blue zone but its diffusion is performed only in the overlapping region $B^{vis}_{\mathbf{x}_i} \cap B^{vis}_{\mathbf{x}_i^{im}}$.

5.7 EVALUATION OF HYDRODYNAMIC LOADS

To evaluate the forces on the body, the pressure must be calculated on the body boundary. A suitable expression can be found by integrating the wall stress tensor (see *e.g.* Graziani and Bassanini (2002)):

$$\mathbf{F_b} = \int_{\partial D} (-p\mathbf{n} + \mu\omega\boldsymbol{\tau})\, dl, \tag{5.96}$$

while the torque with respect to the center of mass $\mathbf{x}_{cm}$ of the body is given by:

$$\mathbf{T_b} = \int_{\partial D_B} (\mathbf{x} - \mathbf{x}_{cm}) \times (-p\mathbf{n} + \mu\omega\boldsymbol{\tau})\, dl. \tag{5.97}$$

The pressure, previously eliminated from the vorticity formulation of the NSEs (eq. (5.2)), can be recovered by the projection of the velocity - pressure formulation (5.1) on the unit tangent vector. For a body moving with velocity $\mathbf{u}_b$, the tangent pressure gradient on the solid surface is related to the velocity field by:

$$\frac{1}{\rho_0}\frac{\partial p}{\partial s} = \boldsymbol{\tau}(s) \cdot [\dot{\mathbf{u}}_\infty - \dot{\mathbf{u}}_b(s)] - \nu\frac{\partial \omega}{\partial n} \quad s \in \partial D, \tag{5.98}$$

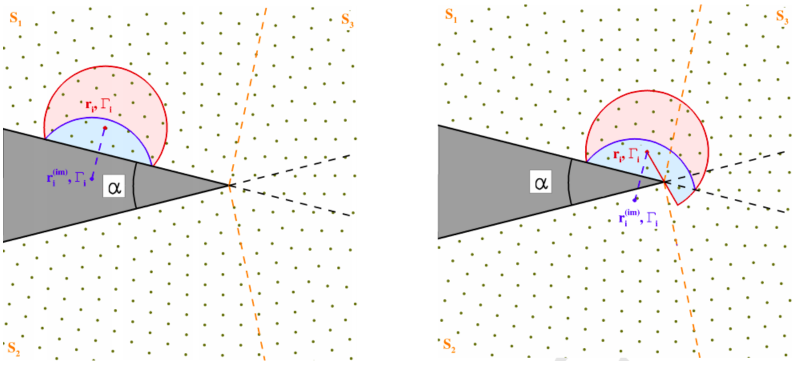

(a) Diffusion in the region S_1 at a distance larger that R_d.

(b) Diffusion in the region S_1 at a distance smaller that R_d.

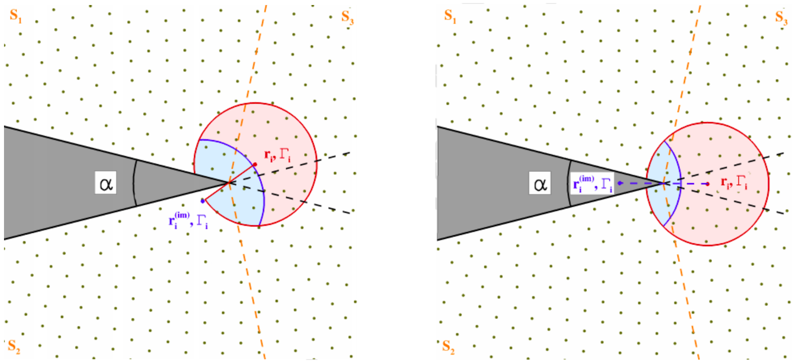

(c) Diffusion in the region S_3 at a distance smaller that R_d, case 1.

(d) Diffusion in the region S_3 at a distance smaller that R_d, case 2.

Figure 5.4: Possible configurations of the vortex and image vortex with respect to the distance of the vortex from the edge. Red zones correspond to the influence of the vortex. Blue zones to the influence of the image vortex (Rossi et al., 2016).

and, from the second equation in (5.8),

$$\frac{1}{\rho_0}\frac{\partial p}{\partial s} = \boldsymbol{\tau}(s) \cdot [\dot{\mathbf{u}}_\infty - \dot{\mathbf{u}}_b(s)] + \dot{\gamma}(s), \quad s \in \partial D_B. \tag{5.99}$$

Equation (5.99) links the tangential pressure gradient on the body with the time variation of the circulation density $\dot{\gamma}$, previously introduced in the Neumann boundary condition for the equation (5.8). It also highlights the role of $\mathbf{u}_\infty$ and $\mathbf{u}_b(s)$, that show that the relative motion between the body and the current determines vorticity on the body boundary ∂D_B.

6

NUMERICAL DETAILS

In this chapter the numerical details for the vortex particle method are given. More specifically in section 6.1 the advection step is presented and the derivation of the time step for this specific step is evaluated. Section 6.2 deals with the diffusion step based on a deterministic algorithm for diffusion followed by the derivation of the respective time step.

6.1 THE ADVECTION STEP

For the advection step, the vortex particles are convected with the velocity given by the discretized form of (5.4):

$$\begin{aligned}\mathbf{u}(\mathbf{x}_i, t) = \mathbf{u}_\infty(t) + \sum_{k=1}^{N_b} [\mathbf{K}_\epsilon(\mathbf{x}_i, \mathbf{y}_k)\gamma_k(t) - \mathbf{e}_3 \times \mathbf{K}_\epsilon(\mathbf{x}_i, \mathbf{y}_k)\sigma_k(t)]\Delta s \\ + \sum_{j=1}^{N_\nu} \Gamma_j(t)\mathbf{K}_\epsilon(\mathbf{x}_i, \mathbf{y}_j),\end{aligned} \tag{6.1}$$

where the body boundary ∂D_B is discretized into N_b flat panels with constant length Δs and K_ϵ is the convolution of the Biot-Savart kernel K with the cut-off function ζ_ϵ.

The numerical integration for the advection of the particles is performed using a fourth-order Runge-Kutta by changing their positions while keeping their circulations constant according to:

$$\frac{D\mathbf{x}_i(t)}{Dt} = \mathbf{u}(\mathbf{x}_i, t), \tag{6.2}$$

$$\frac{D\Gamma_i(t)}{Dt} = 0. \tag{6.3}$$

The time step for advection Δt_a needs to be prescribed. Since Vortex Particle Methods do not discretize explicitly the convective term of NSEs they are not restricted by the classical CFL condition for stability. They are dictated by a Lagrangian CFL that is less limiting in the choice of the time-step and has to be such that particles trajectories should not cross. Thus the particle treatment imposes an accuracy constraint on the time-step (see for example (Cottet and Koumoutsakos, 2000)) which has to be chosen small enough not to advect the generic particles j with a displacement larger than its size Δr_j, in order to avoid situations where particles move too close to each other in one time step. Therefore, the time step is normally chosen as

$$\Delta t_a = K_a \frac{\Delta r_{min}}{U}, \tag{6.4}$$

where U is the reference velocity, K_a is the Courant number which should be of order $\mathcal{O}(10^{-1})$ and Δr_{min} is the size of the smallest particle.

Another important aspect is the use of an Adaptive Particle Resolution (APR) technique (Rossi et al., 2015a) in DVH model. This permits to gradually reduce the particle size in the near-field close to ∂D_B and increase it for increasing distance from the body. As a result, the resolution in the boundary layer and in the region near the body can be high enough while it is decreased with increasing distance from the body boundary reducing the number of the particles in the far-field; this is achieved using different subdomains in D. The particles in the neighborhood of ∂D_B are those that restrict the time step in equation (6.4).

The reconstruction of the velocity field from vorticity is the most computationally intensive part of the algorithm and its direct evaluation with the Biot–Savart formula would require $\mathcal{O}(N_\nu^2)$ operations. This computational cost is mitigated with the Fast Multipole Method (FMM) described in section 5.5, that reduces the cost to $\mathcal{O}(N_\nu \log(N_\nu))$ operations. The FMM can be efficiently parallelized.

6.2 THE DIFFUSION STEP

For the diffusion step, the deterministic algorithm of Benson et al. (1989) is used; accordingly, a discrete vortex is diffused using the elementary solution of the heat equation (5.8) in the free space within time step Δt_d:

$$\omega(\mathbf{x}, t + \Delta t_d) = \begin{cases} \frac{\Gamma_i}{4\pi\nu\Delta t_d} \exp\left(-\frac{|\mathbf{x}-\mathbf{x}_i|^2}{4\nu\Delta t_d}\right) & \forall\, |\mathbf{x}-\mathbf{x}_i| \leqslant R_d, \\ 0 & \text{otherwise.} \end{cases} \tag{6.5}$$

The Gaussian distribution is truncated, for computational reason, at a distance given by the *diffusive radius* $R_d = 4\Delta r$ (this choice is motivated in Rossi et al. (2015b)).

The effect of the solid surface ∂D_B is introduced by a generalization of the method of images (developed also for geometries with vertices; details can be found in Rossi et al. (2016)).

The time step Δt_d is linked to the diffusive radius or equivalently to the size of the particle by

$$\Delta t_d = K_1 \frac{R_d^2}{\nu} = K_2 \frac{\Delta r_j^2}{\nu}, \tag{6.6}$$

where $K_1 = 0.021$, $K_2 = 0.34$ and the choice of the constants is motivated by numerical investigations regarding accuracy. The diffusion time-step is not restricted by a stability constraint since it is performed in the frame of reference of the particle using the exact solution of the diffusion equation. Differently from the advection step, each sub-domain is characterized by a specific Δt_d, and more than one advection step is performed for each diffusion step since in the case of high Reynolds flows, addressed in this work, the advection time-scale is faster than the diffusion one. Therefore, the number of advective steps per diffusion step

$$N_{\Delta t} = \left\lfloor \frac{\Delta t_d}{\Delta t_a} \right\rfloor \Rightarrow \Delta t_a = \Delta t_d / N_{\Delta t}, \tag{6.7}$$

(where $\lfloor \cdot \rfloor$ is the floor function) increases with the particle size Δr_j in each subdomain.

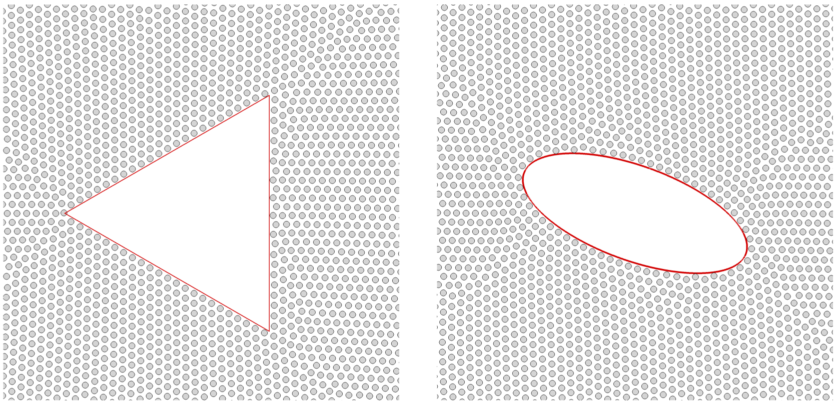

Figure 6.1: Discretization of the computational domain used for the resolution of the flow past a cylinder using the DVH method. Left: Regular Point Distribution (RPD) around a equilateral triangle. Right: Regular Point Distribution (RPD) around an ellipse

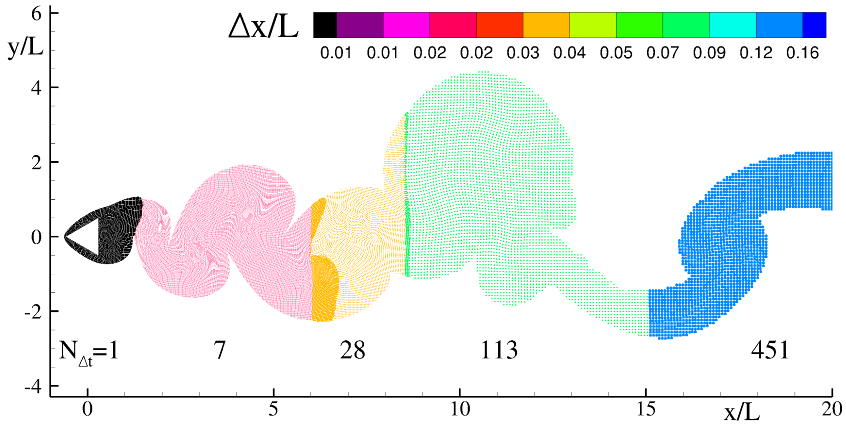

Figure 6.2: Discretization of the computational domain used for the flow past a cylinder with a triangular section using the DVH method. Fluid domain divided in subdomains each with a different particle resolution Δr_j. Each domain is characterized also by different $N_{\Delta t}$ see eq. (6.7).

To prevent undesired clustering and rarefaction during the evolution of the particles the diffusion step is performed on a Regular Point Distribution (RPD). During the diffusive step each vortex particle diffuses its circulation on the RPD; this point distribution consists of a set of points created by a Packing algorithm which automatically arranges the particle in D, in order to have both constant mutual distance Δr and comparable distance with the frontier ∂D_B (see Colagrossi et al. (2012)). The Packing algorithm is used only for the initial RPD distribution and it remains frozen and attached to ∂D_B, it being a rigid solid surface. The RPD is used only in the neighborhood of ∂D_B, while simple Cartesian lattices with different spatial resolution are used in the rest of the domain.

During the diffusion step, each vortex diffuses its circulation over the points of the RPD using eq. (6.5). These geometrical points become a new set of vortex particles for the next time steps.

7

VELOCITY - PRESSURE FORMULATION

In this chapter the procedure to solve the pressure velocity formulation with mesh-based approaches introduced by Chorin, is presented.

In section 7.1, the projection method is presented. The projection method, introduced by Chorin (1968) and Temam (1969) is based on the Helmholtz-Hodge decomposition to enforce the incompressibility condition decoupling the pressure from the momentum equation. For the projection method the solution is split into two steps: in the first, the velocity evolves without the driving force due to the pressure gradient while in the second step, the computed velocity field is projected onto the space of divergence–free vector fields and the incompressibility results from the solution of a Pressure Poisson equation (PPE).

In section 7.2, the Artificial-compressibility (AC) or pseudo-compressibility method is presented. It was initially introduced in Chorin (1967) for steady flows and extended to unsteady flows with the use of dual-time stepping. In this case the evaluation of a divergent free field is performed by the simultaneous iterative solution of both the momentum equation and the divergence equation. The pressure is coupled back to the momentum through the introduction of an artificial pressure pseudo-time derivative term. Finally, in section 7.3, a description of a full solver introduced by Broglia and Durante (2018), used later in the comparisons with the vortex methods DVH will be described, which uses artificial compressibility for time descretization and finite volumes for space descretization.

7.1 PROJECTION METHOD

Consider the Navier-Stokes equations for an incompressible fluid, in velocity - pressure formulation:

$$\frac{D\mathbf{u}}{Dt} = -\frac{\nabla p}{\rho_0} + \nu \Delta \mathbf{u}, \tag{7.1}$$

$$\nabla \cdot \mathbf{u} = 0, \tag{7.2}$$

where $\mathbf{u}$ is the velocity field and p is the pressure, while ν is the kinematic viscosity.

Applying the divergence operator in (7.1) we obtain:

$$\frac{D}{Dt}(\nabla \cdot \mathbf{u}) - \omega^2 + \nabla \mathbf{u} : \nabla \mathbf{u} = -\frac{\Delta p}{\rho_0} + \nu \Delta(\nabla \cdot \mathbf{u}), \tag{7.3}$$

Enforcing the divergence–free condition, the pressure Poisson equation is obtained:

$$\Delta p \;=\; \rho_0 \left(\omega^2 - \nabla \mathbf{u} : \nabla \mathbf{u}\right), \qquad \mathbf{x} \in D \tag{7.4}$$

$$\frac{\partial p}{\partial n} \;=\; -\mathbf{n} \cdot [\dot{\mathbf{u}}_b \;-\; \dot{\mathbf{u}}_\infty] \;+\; \nu \frac{\partial \omega}{\partial \tau}, \qquad \mathbf{x} \in \partial D_B, \tag{7.5}$$

The accompanying Neumann boundary condition comes from the projection of NSEs on the normal to ∂D_B and from the no–slip condition. The pressure field is evaluated from the solution of (7.4) - (7.5); then, the velocity field can be updated by the integration of (7.1) in time, as for example in Harlow and Welch (1965).

It is well known that equation (7.4)-(7.5) does not imply $\nabla \cdot \mathbf{u} \equiv 0$; in fact, when substituting (7.4) in (7.3) results in:

$$\frac{D}{Dt}(\nabla \cdot \mathbf{u}) \;=\; \nu \Delta(\nabla \cdot \mathbf{u}),. \tag{7.6}$$

Therefore, if $\nabla \cdot \mathbf{u}$ is not zero at the initial time in the domain or on ∂D for $t > 0$, a value $\nabla \cdot \mathbf{u} \neq 0$ can appear in D because of the initial condition or as a consequence of diffusion from the boundary.

For this reason, the projection method discussed in Chorin (1968) is preferred. In analogy to what discussed for the solution on NSEs in vorticity, this method consists in a two–step algorithm, which allows to enforce exactly the incompressibility constraint. To achieve this goal, a first step is performed by making the velocity field to evolve at any time t^n under the action of convection and diffusion on a time interval Δt disregarding the pressure. The resulting intermediate velocity $\mathbf{u}^*$ is the solution after the time evolution of the momentum equation (7.1) without the pressure i.e.:

$$\mathbf{u}^* \;=\; \mathbf{u}^n \;+\; \nu \Delta \mathbf{u}^n \, \Delta t. \tag{7.7}$$

In contrast to the velocity $\mathbf{u}^n$, that is divergent-free by hypothesis, the intermediate velocity $\mathbf{u}^*$ is not necessarily divergent-free. To enforce the solenoidal constraint, it is split using the HHD into:

$$\mathbf{u}^* \;=\; \nabla \times \boldsymbol{\Psi} \;+\; \nabla \Phi. \tag{7.8}$$

The divergence–free component is, in this case, the unknown velocity $\mathbf{u}^{n+1}$ at time $t^{n+1} \;=\; t + \Delta t$, while the potential component is expressed through the pressure gradient at t^{n+1}:

$$\nabla \times \boldsymbol{\Psi} \;=\; \mathbf{u}^{n+1}, \qquad \nabla \Phi \;=\; \left(\frac{\nabla p}{\rho_0}\right)^{n+1} \Delta t. \tag{7.9}$$

As underlined in Chorin and Marsden (2013), by the HHD theorem, this decomposition is unique. In order to get the divergence-free component at t^{n+1}, the velocity field evolves in the second step under the action of pressure that acts as correction:

$$\mathbf{u}^{n+1} = \mathbf{u}^* - \left(\frac{\nabla p}{\rho_0}\right)^{n+1} \Delta t. \tag{7.10}$$

The velocity $\mathbf{u}^{n+1}$ must satisfy the incompressibility condition thus by taking the divergence (7.10), a Poisson equation for the pressure is obtained:

$$\Delta p^{n+1} = \rho_0 \frac{(\nabla \cdot \mathbf{u}^*)}{\Delta t}. \tag{7.11}$$

After the solution of the above equation for the pressure at p^{n+1}, the velocity $\mathbf{u}^{n+1}$ is updated using (7.10) giving the required divergence–free velocity field.

In the last decades projection methods are successfully applied also to particle methods such as the Smoothed Particle Hydrodynamics (SPH) and the Moving Particle Semi-implicit (MPS) methods; more details can be found in *e.g.* (Gotoh and Khayyer, 2016; Khayyer and Gotoh, 2011; Xu et al., 2009).

7.2 ARTIFICIAL COMPRESSIBILITY METHOD

A second approach to solve the NSEs in pressure–velocity formulation and avoid the computational difficulties arising from the incompressibility is the *Artificial - Compressibility* (or Pseudo - Compressibility) method. It was originally proposed in Chorin (1967) for the solution of the steady incompressible NSEs. It can be extended to the unsteady case by a *Dual Time Stepping* approach (see for example Soh and Goodrich (1988)).

In the AC method the divergence equation is replaced by an evolution equation for the pressure in *pseudo–time* τ. For the unsteady case, the dual time stepping technique requires also the addition of a pseudo-time τ derivative in momentum equation. The resulting equations are:

$$\frac{\partial \mathbf{u}}{\partial \tau} = -\frac{D\mathbf{u}}{Dt} - \frac{\nabla p}{\rho_0} + \nu \Delta \mathbf{u}, \tag{7.12}$$

$$\frac{\partial p}{\partial \tau} + \beta \nabla \cdot \mathbf{u} = 0, \tag{7.13}$$

where τ is the local pseudo-time, ρ_0 is the density and β is the artificial compressibility parameter. The latter needs to be properly tuned in order to guarantee numerical convergence. As discussed in Ferziger et al. (2002) this parameter is usually chosen as $0.1 \leqslant \beta \leqslant 10$.

The solution of equations 7.12 - 7.13 at each physical time t, is obtained as the steady state solution in pseudo-time τ. The divergent-free constraint is enforced at each physical time step when convergence in τ is achieved. With the transient solution in τ having no physical meaning, the pseudo–time step $\Delta\tau$ can be chosen to speed-up convergence. The resulting algorithms are usually fully implicit in t which constitutes a strong advantage for these methods.

For the evolution in pseudo-time the momentum equation 7.12 and the incompressibility condition 7.13 can be descretized using , for example, implicit Euler:

$$\frac{\mathbf{u}^{m+1}-\mathbf{u}^{m}}{\Delta\tau}+\left(\mathcal{H}(\mathbf{u}^{m+1},p^{m+1})\right)=0, \tag{7.14}$$

$$\frac{p^{m+1}-p^{m}}{\Delta\tau}+\nabla\cdot\mathbf{u}^{m+1}=0. \tag{7.15}$$

where

$$\mathcal{H}(\mathbf{u},p)=\frac{\mathbf{u}-\mathbf{u}^{n}}{\Delta t}+\mathbf{u}\cdot\nabla\mathbf{u}+\frac{1}{\rho_0}\nabla p-\nu\Delta\mathbf{u}, \tag{7.16}$$

and m and n are the iterations in pseudo - time and physical time respectively. A tolerance bound is set for the m iterations as follows:

$$\beta\left|\nabla\cdot\mathbf{u}^{m+1}-\nabla\cdot\mathbf{u}^{m}\right|\leqslant\epsilon_{tol}, \tag{7.17}$$

where ϵ is usually selected to machine precision. When the difference of m iterations becomes smaller than the bound, the last iteration $m+1$ in pseudo-time becomes the next iteration in physical-time $n+1$:

$$\mathbf{u}^{n+1}\leftarrow\mathbf{u}^{m+1}. \tag{7.18}$$

The equations corresponding now to the steady state in τ are discretized in time. Selecting an implicit in time descretization such as the Crank Nicolson method (Soh and Goodrich, 1988) leads to:

$$\frac{\mathbf{u}^{n+1}-\mathbf{u}^{n}}{\Delta t}+\frac{1}{2}\left(\mathcal{F}(\mathbf{u}^{n+1},p^{n+1})-\mathcal{F}(\mathbf{u}^{n},p^{n})\right)=0, \tag{7.19}$$

$$\nabla\cdot\mathbf{u}^{n+1}=0, \tag{7.20}$$

where

$$\mathcal{F}(\mathbf{u},p)=\mathbf{u}\cdot\nabla\mathbf{u}+\frac{1}{\rho_0}\nabla p-\nu\Delta\mathbf{u}. \tag{7.21}$$

7.3 DISCRETIZATION USING THE FINITE VOLUME METHOD

In the present section a scheme based on the Finite Volume Method with Artificial compressibility is described. The solver described in the following, will be used in order to compare its numerical results with those obtained with the vortex method DVH on benchmark tests.

Following Broglia and Durante (2018), Muscari et al. (2017) and Pasquale et al. (2019) the computations are performed by discretizing the domain with a block-structured mesh with partial overlapping. The computational domain D is split into sub-domains, each discretized by a block-structured grid. The sub-domains are not disjoint, but some portions can overlap (chimera-type grid). An example of the computational grid is shown in figure 7.1. For the Finite Volume implementation, pressure and velocity are collocated on the cell centers. Each subdomain is discretized by a structured block subdivided into $N_i \times N_j$ subdomains D_{ij}, and the NSEs are written in (weak) integral form on each volume:

$$\int_{D_{ij}} \frac{\partial \mathbf{u}}{\partial t} dV + \int_{\partial D_{ij}} \mathbf{F} \cdot \mathbf{n} \, dS = 0, \tag{7.22}$$

$$\int_{\partial D_{ij}} \mathbf{u} \cdot \mathbf{n} \, dS = 0, \tag{7.23}$$

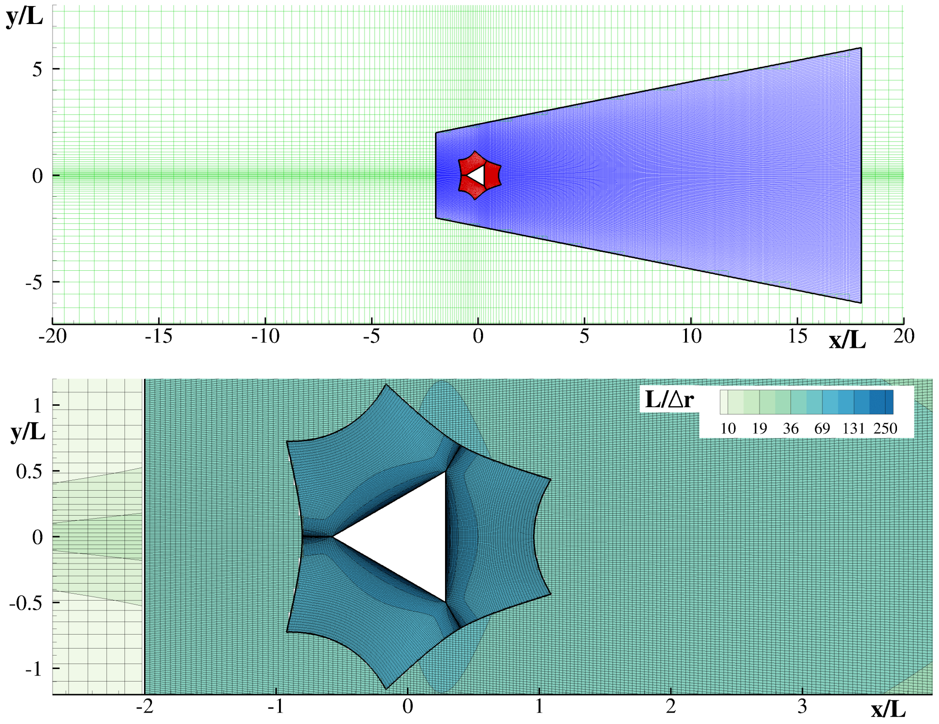

Figure 7.1: Discretization of the computational domain used for the resolution of the flow past a cylinder with a triangular section using the FV method. Top: sketch of the fluid domain from -20L to 20L; the three chimera blocks are colored with different colors. Bottom: zoomed view around the solid body; the color contour is representative of the local spatial resolution $L/\Delta r$, where Δr is the square root of the cell volume.

where $\mathbf{n}$ is the outward normal to the subdomain boundary ∂D_{ij}:

$$\mathbf{F} = \mathbf{u} \otimes \mathbf{u} + \frac{p}{\rho_0}\mathbb{I} - \mathbb{T} \qquad \text{with} \qquad \mathbb{T} = \nu\left(\nabla \mathbf{u} + \nabla^T \mathbf{u}\right), \tag{7.24}$$

$\mathbb{I}$ is the unit tensor and $\mathbb{T}$ the stress tensor. For the numerical approximation, we set:

$$\mathbf{u}_{ij} = \frac{1}{V_{ij}} \int_{D_{ij}} \mathbf{u} dV, \qquad \mathbf{F}_l = \int_{S_l} \mathbf{F} \cdot \mathbf{n}\, dS, \qquad \mathbf{U}_l = \int_{S_l} \mathbf{u} \cdot \mathbf{n}\, dS, \tag{7.25}$$

as the approximate average value of the solution in D_{ij} (V_{ij} being its measure), the average flux on the l-th interface and the average volume flux through the l-th interface respectively. The equations are then rewritten as:

$$V_{ij} \frac{d\mathbf{u}_{ij}}{dt} + \sum_{l \in L_{ij}} \mathbf{F}_l = 0, \tag{7.26}$$

$$\sum_{l \in L_{ij}} \mathbf{U}_l = 0, \tag{7.27}$$

where L_{ij} is the subset of the cell interfaces for subdomain D_{ij}. The equations are implicitly discretized in time by the Crank-Nicolson method:

$$V_{ij} \frac{\mathbf{u}_{ij}^{n+1} - \mathbf{u}_{ij}^{n}}{\Delta t} + \frac{1}{2}\left(\sum_{l \in L_{ij}} \mathbf{F}_l^{n+1} + \sum_{l \in L_{ij}} \mathbf{F}_l^{n}\right) = 0, \tag{7.28}$$

$$\sum_{l \in L_{ij}} \mathbf{U}_l^{n+1} = 0, \tag{7.29}$$

and the solution $(\mathbf{u}^{n+1}, p^{n+1})$ at each time step is computed using the dual-time stepping approach as the asymptotic solution in pseudo-time τ:

$$\frac{\partial \mathbf{u}^{n+1}}{\partial \tau} + \left[V_{ij} \frac{\mathbf{u}_{ij}^{n+1} - \mathbf{u}_{ij}^{n}}{\Delta t} + \frac{1}{2}\left(\sum_{l \in L_{ij}} \mathbf{F}_l^{n+1} + \sum_{l \in L_{ij}} \mathbf{F}_l^{n}\right)\right] = 0, \tag{7.30}$$

$$\frac{\partial p^{n+1}}{\partial \tau} + \rho_0 \beta \left(\sum_{l \in L_{ij}} \mathbf{U}_l^{n+1}\right) = 0, \tag{7.31}$$

where the terms containing $(\mathbf{u}^n, p^n)$ are known from the previous time step.

As mentioned before, the transient solution in pseudo-time has no physical meaning and thus the time-step $\Delta\tau$ can be selected so as to accelerate convergence to the steady state. The algorithms adopted to speed up convergence to the asymptotic solution in the pseudo-time are: local pseudo-time stepping, implicit iteration with approximate factorization and multi-grid (for more details see Broglia and Durante (2018) and references therein).

For the discretization of the inviscid interface flux terms (convection and pressure) a centered scheme with second order of accuracy is used and a small amount of artificial dissipation is added in the implicit operator to prevent numerical oscillations.

For the viscous interface flux terms also a standard second order centered scheme is adopted. Thus the resulting scheme is second order in space and in time.

The use of block boundaries facilitates the computations in case of complex geometry or moving boundaries. The solution at the block boundaries with no natural boundary conditions is transferred from the other blocks by cubic interpolation. In the interior cells belonging to overlapped zones the discrete equations are not removed (i.e. no holes are produced in the grid). Instead, a forcing term is added to the discrete NSEs so that the solution is driven by the solution computed on the locally finest grid. The advantages of this approach is that algorithms developed for structured grids (multi-grid, approximate factorization methods, etc.) remain unchanged.

The forcing term added to the left-hand side of the above equations is of the form:

$$\frac{K}{\min(\Delta_x, u_\infty \Delta t)}(q - q_{int})V_{ij},$$

where q is the variable of interest, q_{int} is its value interpolated from the finer grid, K is a constant with the physical dimension of a velocity $O(10 \times u_\infty)$, Δ_x is the local grid size. This term causes an exponential decay in time of q toward q_{int} with characteristic time $\min(\Delta_x, u_\infty \Delta t)/K$.

The definition of boundary conditions on solid surfaces and in the far-field for exterior flows is the following:

- Solid walls: the velocity of the fluid is set equal to the local wall velocity,
- inflow: the velocity is set to the value of the undisturbed flow,
- outflow: the velocity is extrapolated from inner points.

Part III

VALIDATIONS AND PHYSICAL INVESTIGATIONS

8

COMPARISON OF FVM AND DVH SOLUTIONS FOR BENCHMARK TESTS

In this chapter, the numerical results are presented for both DVH and FVM, and detailed comparisons are carried out for three different test cases. Section 8.1 presents the results for flow past a circular cylinder in an unsteady current for five different Reynolds numbers ranging from 100 to 4000. In section 8.2, the results are for flow past an cylinder with an elliptical section with incidence for three different Reynolds numbers 200, 500, 1000. Finally in section 8.3, the flow past a cylinder with a triangular section for two different Reynolds numbers 100 and 1000 is investigated. The test cases are of increasing complexities, but flow separation and shear-layers are always present. The results presented in this chapter were published in Giannopoulou et al. (2019a).

8.1 FLOW PAST A CIRCULAR CYLINDER IN AN UNSTEADY CURRENT

As a first test case, a simple circular cylinder of diameter D is considered. A non constant incoming current is considered $\mathbf{u}_\infty(t) = u_\infty(t)\,\mathbf{e}_1$, where $\mathbf{e}_1$ is the unit vector of the x-axes. The acceleration $a_\infty(t) = du_\infty/dt$ is null for $tU/D > 1$:

$$u_\infty(t) = \begin{cases} \dfrac{U}{2}\left[1 - \cos\left(\dfrac{\pi t}{t_r}\right)\right], & t \leqslant t_r \\ U, & t > t_r \end{cases} \quad ; \quad a_\infty(t) = \begin{cases} \dfrac{U\pi}{2\,t_r}\sin\left(\dfrac{\pi t}{t_r}\right), & t \leqslant t_r \\ 0, & t > t_r\,. \end{cases} \tag{8.1}$$

where $t_r = D/U$.

Figure 8.1 displays the vorticity field for Re=100 (top plot) and 4000 (bottom plot), $Re = U\,D/\nu$ being the Reynolds number. The size of the smallest particles in the boundary layer is indicated by Δx.

In the first stages of the flow evolution, the vorticity in the boundary layer region is anti-symmetric with respect to the x axis and the flow is completely attached. As expected, the boundary layer thickness for Re=4000 is much smaller than that for Re=100.

At the instant of maximum acceleration $tU/D = 1/2$ the flow is not very different from a potential flow, the boundary layer region excluded. Conversely, during the second stage (right plots) the flow separates in the rear and counter rotating vortices develop. At the end of the simulation $tU/D = 3$ the flow is still

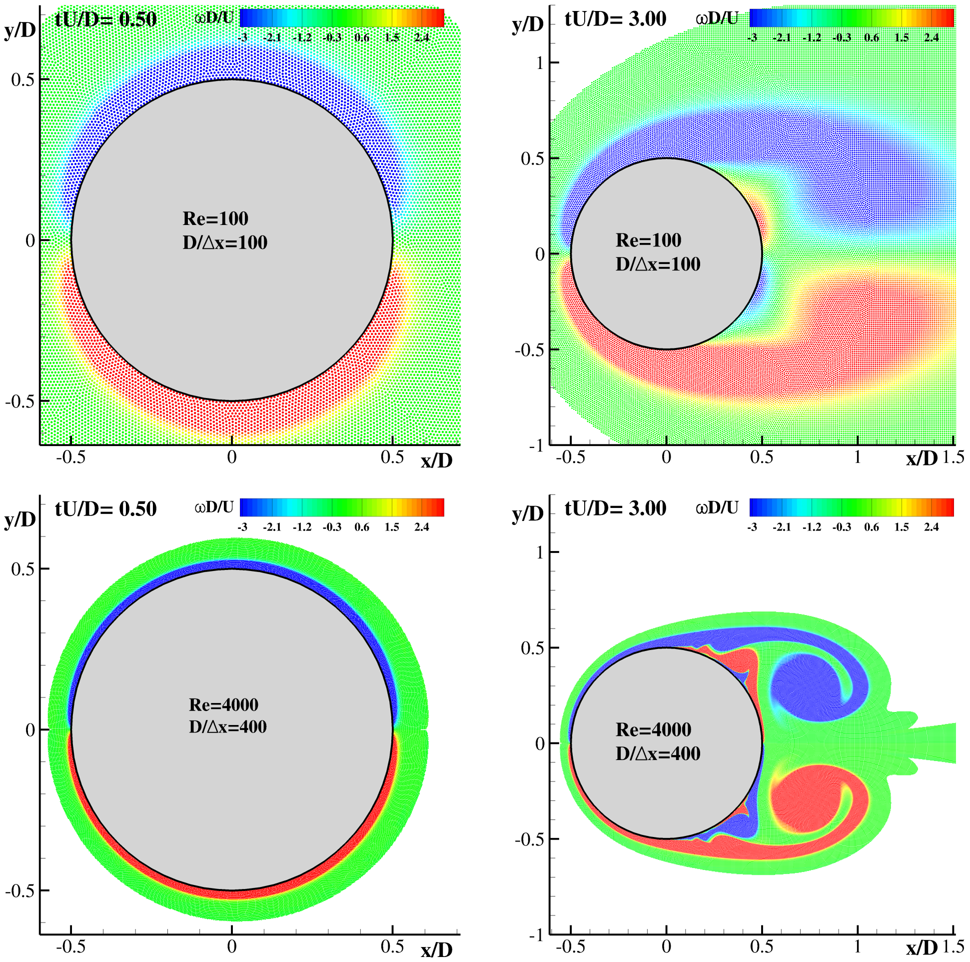

Figure 8.1: Flow past a circular cylinder in an unsteady current. Left part: Boundary layer region at maximum acceleration. Right part: diffusion of vorticity

symmetric with respect to the x axis, but the vorticity field at Re=4000 is much more complex than the one obtained at Re=100, because thinner vorticity structures appear. These smaller structures require smaller particles for a proper resolution: for this reason, $D/\Delta x$ is four times larger for Re=4000.

Figure 8.2 shows the vorticity fields at $tU/D = 3$ for Re=200, 500, 1000. From the picture is evident how the shear layers develop and grow in intensity when decreasing the viscosity. As already said, the resolution was increased with the Reynolds number to capture the thinner structures.

Figure 8.3 depicts the vorticity fields at $tU/D = 3$ evaluated with DVH (left plot) and FVM (right plot) for the highest Reynold number, i.e. Re=4000. For the FVM two overlapping meshes are shown, the one close to the body being strongly stretched to capture the high velocity gradients close to ∂D_B. The overall agreement in terms of vorticity is very satisfactory; nevertheless, some local differences can be

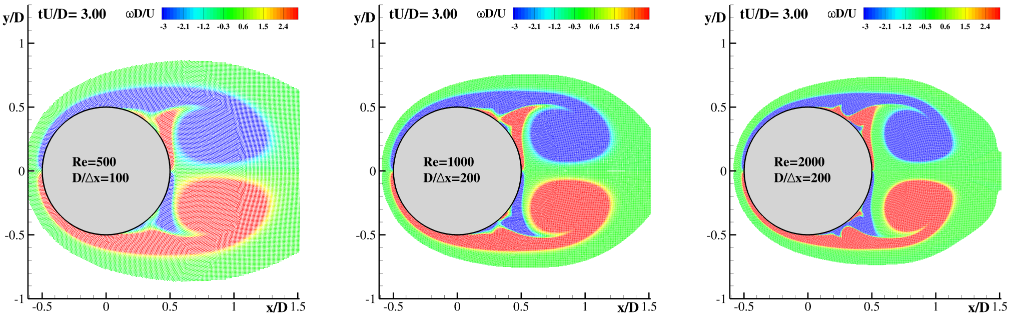

Figure 8.2: Flow past a circular cylinder in an unsteady current. Left to right: Shear layer formation for Re 500, 1000 and 2000.

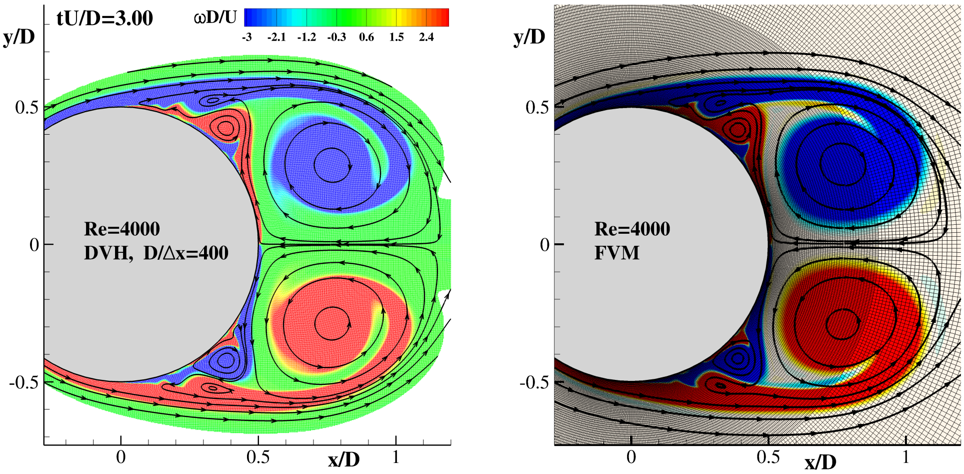

Figure 8.3: Flow past a circular cylinder in an unsteady current. Vorticity field and streamlines of the near wake for Re=4000 evaluated by the DVH model (left) and by the FVM (right).

detected. For a better comparison, also the streamlines are reported in the same figure; they show the presence of a small recirculation zone resulting from the complex interaction between the primary and the secondary shear layer.

Finally, figure 8.4 shows the time histories of the pressure and viscous drag coefficients defined as:

$$C_{Dp} = \frac{\displaystyle\int_{\partial D_B} -p\,\mathbf{n}\cdot\boldsymbol{e}_1\,ds}{\frac{1}{2}\rho\,U^2\,D}\,, \qquad C_{D\nu} = \frac{\displaystyle\int_{\partial D_B} \mu\omega\boldsymbol{\tau}\cdot\boldsymbol{e}_1\,ds}{\frac{1}{2}\rho\,U^2\,D} \tag{8.2}$$

The upper part of figure 8.4 reports the computed pressure drag coefficient C_{Dp}, and its comparison with the potential-flow solution, given in terms of drag force by:

$$F_x(t) = M_{add}\,a_\infty(t); \qquad M_{add} = \rho\,\pi\,D^2/4, \tag{8.3}$$

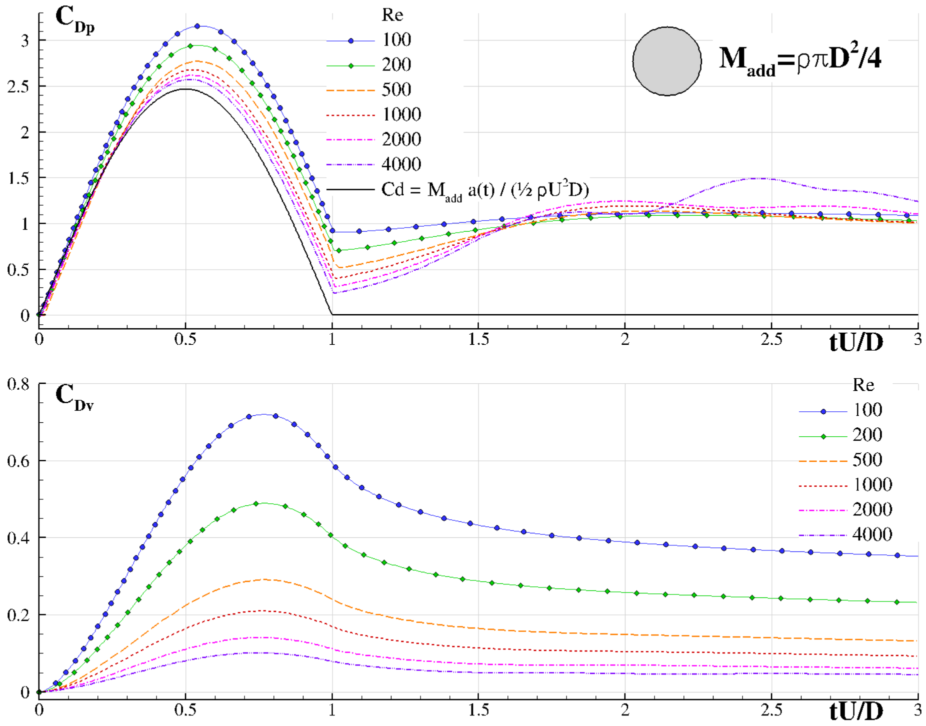

Figure 8.4: Flow past a circular cylinder in an unsteady current for increasing Reynolds number simulated with DVH. Time histories of the pressure (top) and viscous (bottom) components of the drag coefficients.

M_{add} being the so–called "added mass". It can be clearly seen that C_{Dp} tends to the potential flow solution as the Reynolds number is increased. It can also be noticed that, at $tU/D = 1$ (the time instant where the acceleration goes back to zero), C_{Dp} is characterized by a sudden change of the steepness, that increases with the Reynolds number. For $tU/D > 1$, the evolution is instead more complicated, the behavior being not monotonic. The bottom part of figure 8.4 reports the viscous drag component $C_{D\nu}$ and shows its expected reduction for decreasing viscosity. Besides, it is interesting to note that, during the second stage ($tU/D > 1$), the time history of $C_{D\nu}$ is characterized by a positive second derivatives, while at $tU/D = 1$ an inflection point can be detected.

8.2 FLOW PAST AN ELLIPTICAL CYLINDER WITH INCIDENCE

The geometry considered for this test case is an ellipse with an incidence of $\alpha = 20°$, for Reynolds number 200, 500 and 1000. The axis ratio is $b/a = 0.4$, a and b being the major and minor axis; the Reynolds number is defined as $Re = U\,a/\nu$. For all the test cases considered, the flow past the elliptical cylinder is unsteady, and the periodic regime solution exhibits the typical character of the von Kármán shedding mechanism.

Figure 8.5 shows the vorticity solution evaluated with the DVH at the end of the simulations, for the three values of the Reynolds numbers. When increasing the Re, the shear layers become thinner and their roll-up becomes more intense; however, the flow always separates upstream of $x = 0$ for all the three values of Re.

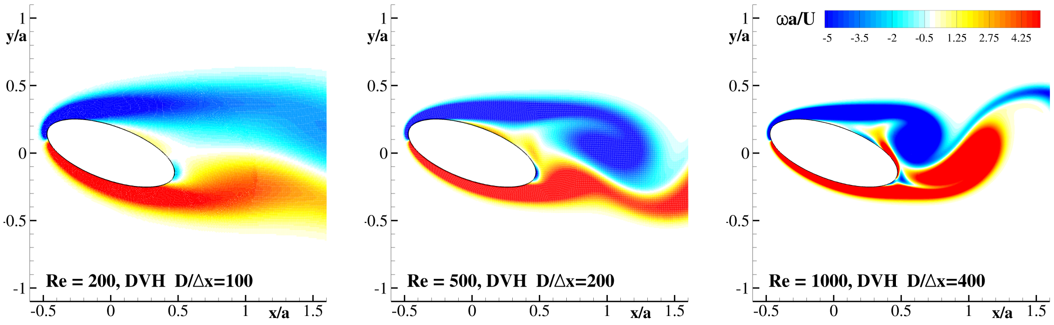

Figure 8.5: Flow past an elliptical cylinder with incidence $\alpha = 20°$. Vorticity field from DVH for Re=200, 500, 1000

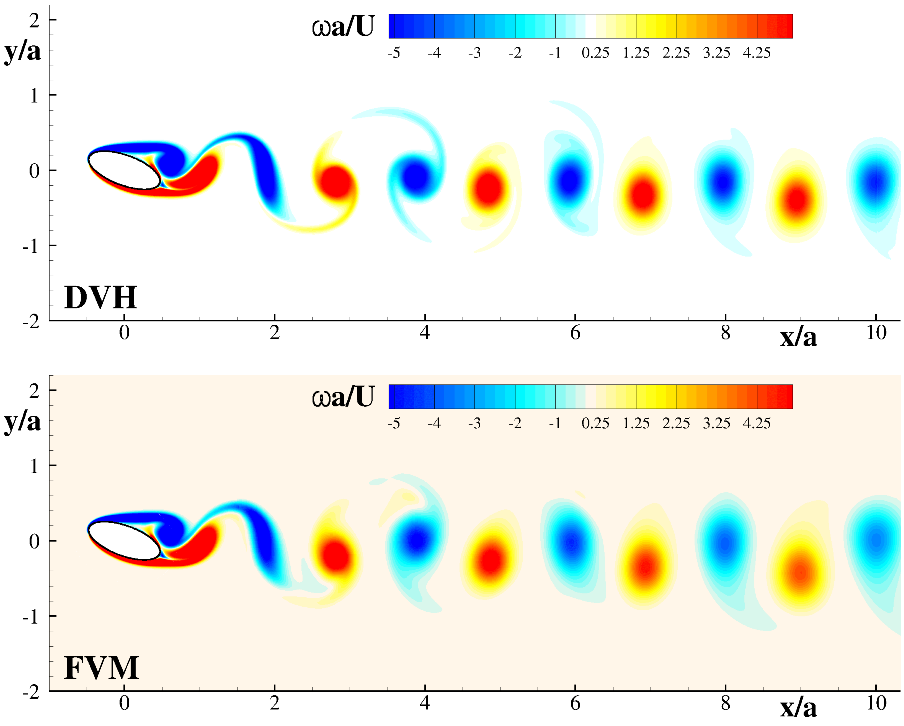

Figure 8.6: Flow past an elliptical cylinder with incidence $\alpha = 20°$ for Re=1000. Comparison of vorticity fields between DVH and FVM.

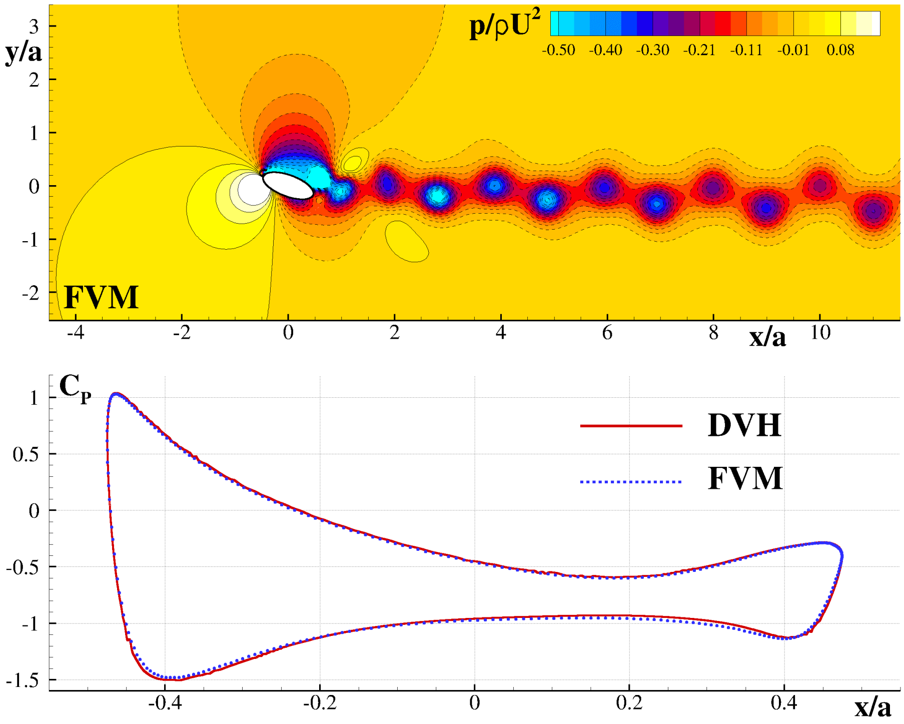

Figure 8.7: Flow past an elliptical cylinder with incidence $\alpha = 20°$ for Re=1000. Top: Pressure field evaluated at maximum lift by the FVM. Bottom: Pressure profiles of DVH and FVM for the same time instant.

Figure 8.6 shows the vorticity fields at Re=1000 evaluated with both methods. The chosen time instant is the one of maximum lift. The DVH and the FVM are in a good agreement, especially for the near field, which is the most important region for the evaluation of hydrodynamic forces. As to the far field, both solutions show the same number of vortices, with identical positions. Also the magnitude of the vorticity in the vortex cores is very similar, although in the FVM the small filament visible in the DVH solution are damped in the far wake, because of the coarser grid resolution in this region.

The plot on the top of Figure 8.7 depicts the pressure field obtained by the FVM. It is to be noticed the slow decay with the distance of pressure perturbation: this is the reason for the huge background domain (the far boundary is placed at $100a$), whose size was chosen to have negligible blockage effects. From the pressure field from the FVM, it is possible to see the large negative pressure region, developed on the suction side of the ellipse as a consequence of the flow separation. The plot on the bottom of the same figure reports the pressure coefficient:

$$C_p = \frac{(p - p_\infty)}{\frac{1}{2}\,\rho\,U^2} \tag{8.4}$$

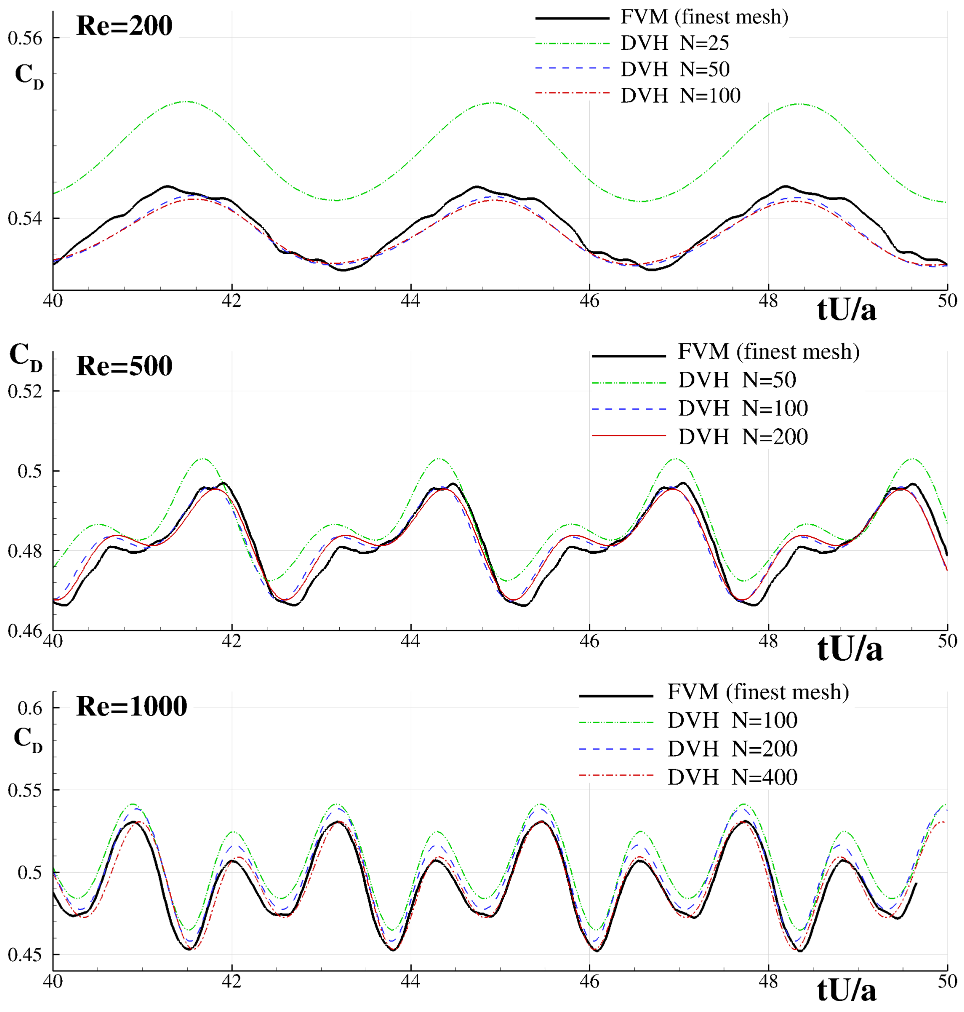

Figure 8.8: Flow past an elliptical cylinder with incidence $\alpha = 20°$. Top to bottom: Comparison of drag coefficients between DVH and FVM for Re=200, 500, 1000.

on the surface. The FVM results (dottet line) are compared with the C_p evaluated with the DVH by the integration of pressure on the boundary. The two curves are graphically superimposed, showing good agreement between the solvers also in terms of local quantities.

The last comparison between FVM and DVH for the ellipse with incidence is reported in terms of drag for the three different Reynolds numbers. For the DVH solution, three different resolution $N = D/\Delta x$ were used to check the convergence of the Vortex Particle Method. Figure 8.8 displays the time histories of the drag coefficients for three different Re for one oscillation period. The matching between FVM and the most resolved DVH is very good for all the viscosity values checked.

The convergence rate for the drag coefficient is measured in terms of L_1 norm:

$$\epsilon_{21} = \int_{t_0}^{t_f} |f_2 - f_1| \, dt, \tag{8.5}$$

where $[t_0, t_f]$ is the time interval considered, f_1 is the value computed with the finest resolution and f_2 the value computed with a particle distribution for which $D/\Delta x$ is halved. To check convergence, a third particle level with $D/\Delta x$ halved again was considered; the computed value is referred to as f_3. The convergence rate is then given by:

$$C(C_D) = \log\left(\frac{\epsilon_{32}}{\epsilon_{21}}\right) \Big/ \log(2). \tag{8.6}$$

A justification for the use of formula (8.6) can be found for example in the works of Barba (2007) and Roache (1997). Considering $t_0 = 40a/U$ and $t_f = 50a/U$ as reported in figure 8.8, the computed convergence rates are $C(C_D) = 4.1, 2.7, 2.0$ for Re=200, 500, 1000 respectively. The decrease of this rate can be justified by the fact that the increase of the Reynolds number is larger than the increase of $D/\Delta x$.

In Rossi et al. (2015b) a rate of convergence between 2 and 4 has been measured for the DVH when solving problems of free vorticity dynamic (i.e. no solid bodies are considered) if the parameter $N_{\Delta t}$ remains small, $N_{\Delta t} \leqslant 2$. The latter means that errors due to multiple advection steps are not accumulated since after each advection step the diffusion step with the combination of the RPD provides a regular distribution of vortices thus resolving the problem caused due to Lagrangian distortion. This condition is always respected for the discretizations $N = D/\Delta r_{min}$ adopted close to the body in all the simulations performed here.

Regarding the FVM method the computed convergence rates are $C(C_D) = 4.2$, 4.1, 2.4 for Re=200, 500, 1000 respectively.

8.3 FLOW PAST A CYLINDER WITH TRIANGULAR SECTION

In this section, the flow past a cylinder with a triangular section is considered for two values of the Reynolds numbers, i.e. Re=100 and Re=1000. The section is an equilateral triangle with side of length L, and the Reynolds number is defined as $Re = U L/\nu$.

The presence of sharp edges produces high spatial gradients and requires also a careful numerical treatment. To this end, the mesh close to the body for the FVM is made of three different patches, which are locally orthogonal and stretched toward the wall, as shown in figure 7.1, in order to obtain the proper resolution required. For the DVH, the complexities arise in the diffusion step because of the presence of these geometrical singularities. In Rossi et al. (2016) a solution for this problem was proposed and validated against different benchmarks.

Also for this test case, the solution reaches a periodic regime after a transient stage for both values of the Reynolds number. However, for Re=1000 irregular

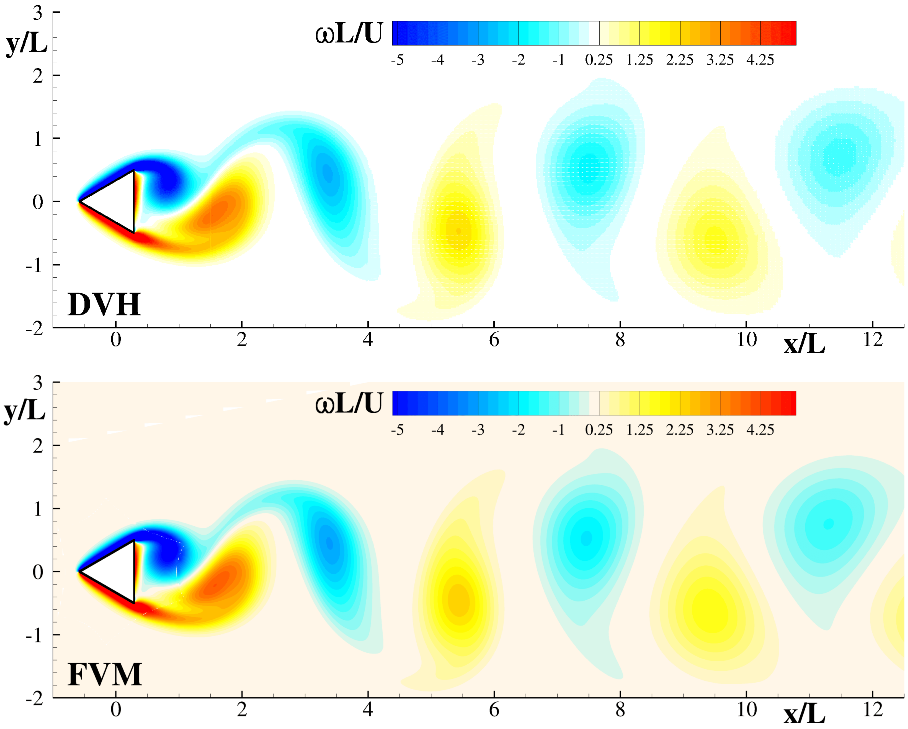

Figure 8.9: Flow around a cylinder with triangular section for Re=100. Comparison of vorticity fields between DVH and FVM in the periodic regime at maximum lift.

small amplitude low frequencies components are visible on the time records of the forces. This is a clear symptom of incipient chaotic behavior (this was not the case for the elliptical profile, for which the solution at Re=1000 is exactly periodic). Another relevant flow characteristic is that the boundary layers on the two sides are completely attached, and flow separation always takes place at the sharp edges. The latter generates two shear layers which roll-up quite close to the cylinder and give rise to the von Kármán street.

In figure 8.9, the vorticity fields in the periodic regime for Re=100 evaluated by the DVH and FVM are reported. As for the previous test case, the two solutions show the same flow characteristics in terms of number of vortices, position and shape of vorticity contours.

Figure 8.10 depicts the comparison between DVH and FVM on the time histories of the lift, drag and torque coefficients for Re=100. The torques is evaluated around the center of mass. Also for this case, a very good comparison between the solvers is observed. The time histories of the drag and lift are practically sinusoidal, while the torque exhibits a richer frequency content.

Figure 8.11 displays the whole time evolution of the drag for increasing spatial resolution $N = L/\Delta x$ =50, 100, 200, 400. The flow in the first stage $tU/L \in [0, 30]$ remains practically symmetric with respect to the x-axis. After this stage, the

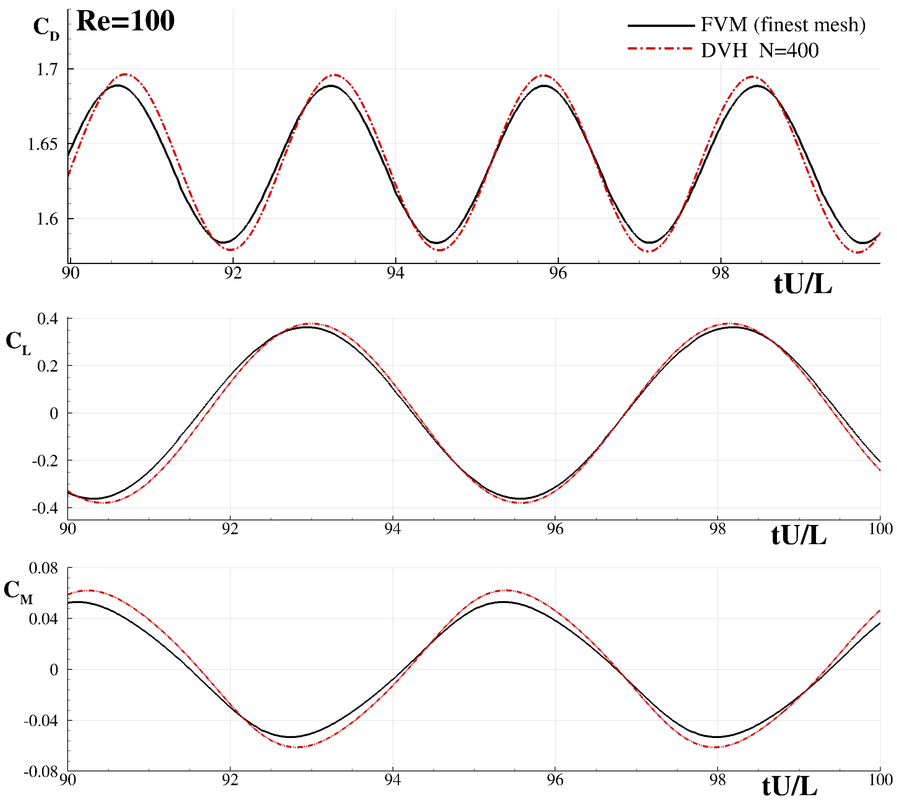

Figure 8.10: Flow around a cylinder with triangular section for Re=100. Comparison of the time histories of the drag, lift and torque coefficients between DVH and FVM in the periodic regime.

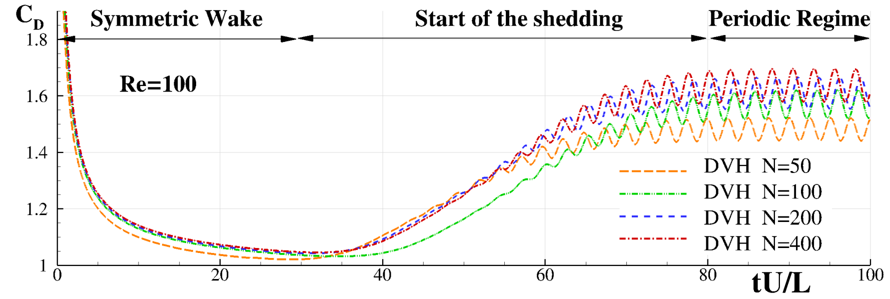

Figure 8.11: Flow around a cylinder with triangular section for Re=100; solution from DVH. Time histories of the drag coefficient with four different spatial resolutions: $L/\Delta x = 50$, 100, 200, 400.

shedding mechanism start and for $tU/L > 30$ a periodic regime is reached by the four simulations.

During the first stage the computed convergence rate for $C(C_D)$ defined by eq. (8.6) is close to 2. Conversely, it reduces to 1 during the periodic regime. This value is lower than the one observed for the elliptical profile; this is probably due to the stronger and localized gradients around the edges, that were absent in the smooth profile. Incidentally, also for the FVM during the periodic regime, the computed convergence rate $C(C_D)$ is of order 1. The factors that affect the convergence rate could be the operator splitting scheme and the singularity at the front of the triangular cylinder. This behaviour deserves a more in-depth analysis which is left for future works.

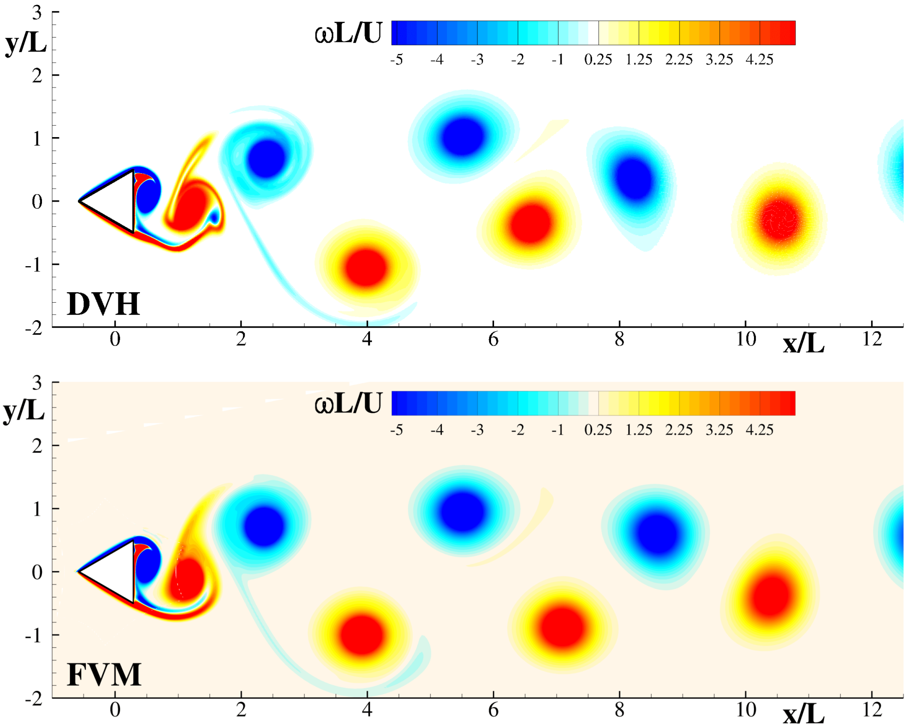

Figure 8.12: Flow around a cylinder with triangular section for Re=1000. Comparison of vorticity fields between DVH and FVM in the periodic regime at maximum lift.

Figure 8.12 depicts the vorticity fields evaluated by DVH and FVM for Re=1000 during the periodic regime. This lower viscosity level is characterized by a more complex vorticity field with intense roll-up of the shear layers. The near fields calculated by the two solvers are in a very good agreement, while differences appear in the wake region. In particular, the FVM solution is smoother and, again, this is due to the coarser resolution in this region with respect to the one used in the DVH. The number of vortices are the same but the core positions show some differences.

Figure 8.13 shows the comparison between DVH and FVM solutions for drag, lift and torque time histories for Re = 1000 in the periodic regime. As observed for the vorticity, the FVM solution for the drag appears smoother than the DVH one. Besides, differently from the case Re=100, the time behaviour showed by the two solvers is no longer sinusoidal, because of the more intense action of the shear

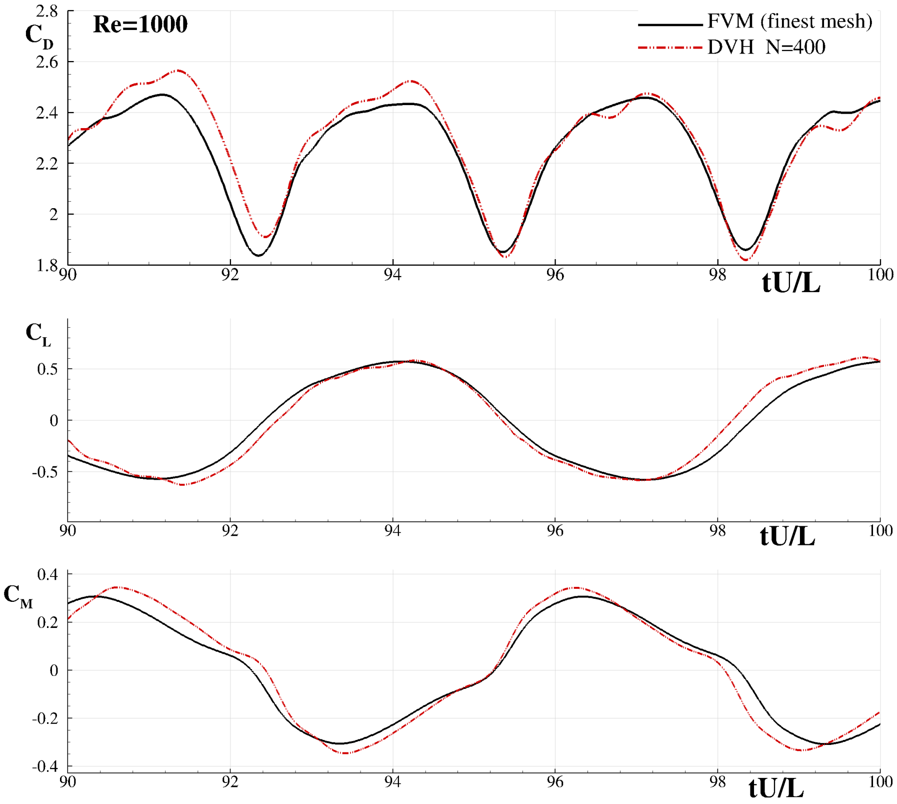

Figure 8.13: Flow around a cylinder with triangular section for Re=1000. Comparison of the drag, lift and torque coefficients between DVH and FVM in the periodic regime.

layers at Re=1000. Conversely, the lift force remains almost sinusoidal, with a better match between the two numerical solutions. As for Re=100, the torque also departs from simple sinusoidal oscillations; the agreement between DVH and FVM is again good.

Figure 8.14 shows the instantaneous pressure field for both Reynolds numbers evaluated with FVM during vortex shedding. The negative pressure field regions corresponds to the zones characterized by high vorticity. Note that the pressure scales adopted for the plot at the two Reynolds numbers are different, they being adapted to the observed pressure range that strongly depend on the deeply different vorticity fields. As for the ellipse, the decay of pressure disturbances with distance is very slow; in order to prevent blockage effects, a very large background domain (the far boundary is placed at $\approx 100L$) was used.

Figure 8.15 show the pressure coefficients around the body at the same time instant of the previous figures, for both the Reynolds numbers. The profile are non-symmetric with respect to the x-axis because the time instant chosen corresponds to the maximum of the lift. The comparison between DVH and FVM is fair, although not as good as the one observed for the elliptical profile: in particular, the largest

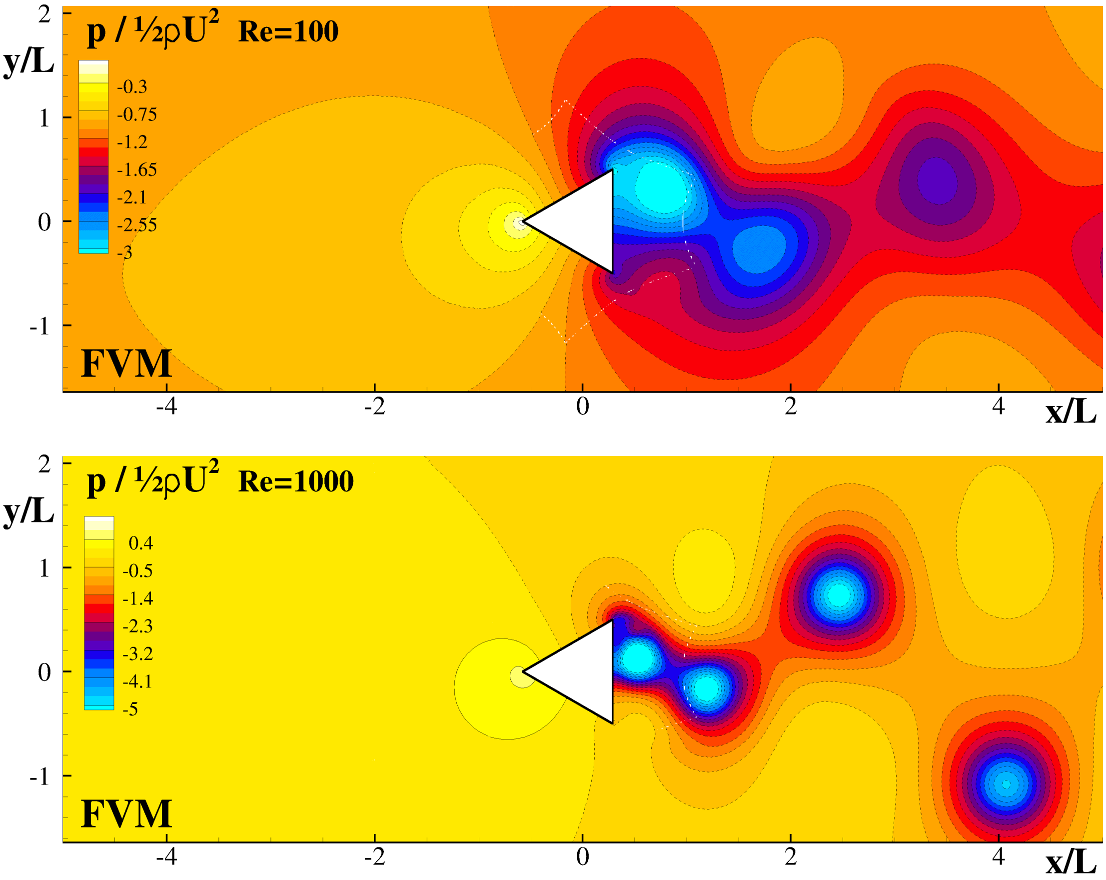

Figure 8.14: Flow around a cylinder with triangular section for Re=1000. Pressure field at maximum lift evaluated by the FVM solver; Re=100 (top), Re=1000 (bottom)

differences are in the regions close to the cylinder edges, with the DVH showing more intense pressure drops. This is probably due to the more accurate evaluation of pressure gradient around sharp corners with DVH, as observed in Rossi et al. (2016) for the flow around cylinder with rectangular section. A further investigation about this aspect will be the subject of future research.

8.4 COMPUTATIONAL RESOURCES

Table 8.1 reports the test-cases simulated with both solvers.

All the DVH and FVM simulations have been performed on a desktop PC with eight cores Xeon(R) E5-2698 v3, 2.30GHz, using a simple OpenMP parallel implementation. The maximum number of particles used is of order 10^6 and the allocated memory did not exceed 1 Gbyte. The parameter η:

$$\eta = (\text{Total CPU time} \times \text{N}^{\circ}_{\text{cores}}) \,/\, \left(\text{N}^{\circ}_{\text{iterations}} \times \text{N}^{\circ}_{\text{vortices}}\right)$$

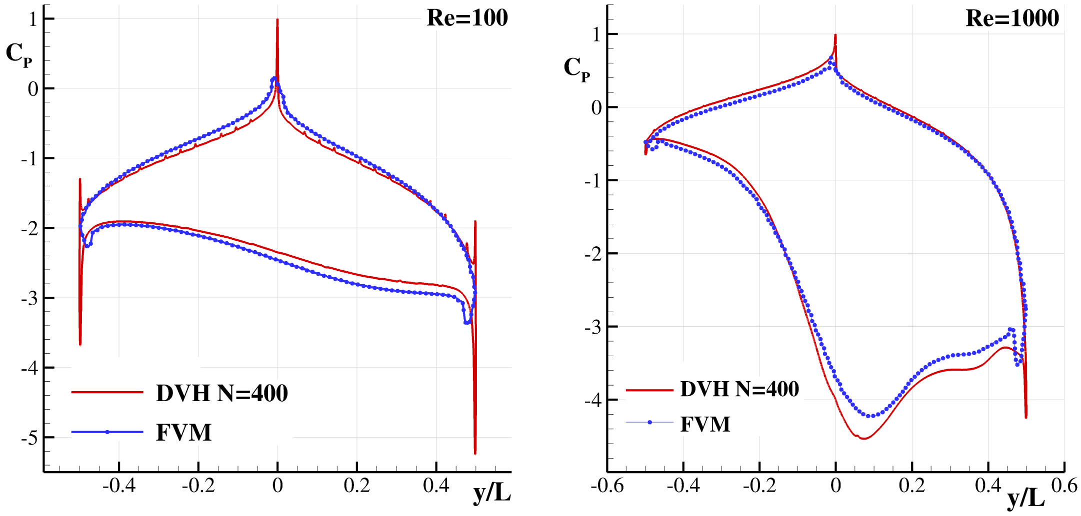

Figure 8.15: Flow around a cylinder with triangular section for Re=1000. Pressure coefficient evaluated by the FVM solver and DVH solver on the surface of the solid body at maximum lift, Re=100 (left), Re=1000 (right).

of the DVH solver is about 100µs. Even if the DVH in-house code developed is just a research code and not fully optimized, the η cost is inline with other vortex particle solvers and mainly linked to the Fast Multipole Method for the solution of the Poisson equation.

Regarding the in-house FVM solver the parameter η:

$$\eta = (\text{Total CPU time} \times N^{\circ}_{\text{cores}}) / \left(N^{\circ}_{\text{iterations}} \times N^{\circ}_{\text{cells}}\right)$$

is about $50 - 90\mu s$ (the differences are linked to the number of iterations for solving the pseudo-time, see following section. Therefore, in case we used the same time-step for the two solvers and a number of cells of the FVM comparable to the number of vortices of the DVH, the CPU costs would be comparable, as already highlighted in Rossi et al. (2016).

CPU costs of DVH are reported in Table 8.2 for four test-cases together with the main parameters. The same data are reported in Table 8.3 for the FVM solver. The CPU costs of the FVM solver are much smaller than those observed for the DVH computations. However, the comparisons between the two solvers cannot be performed in a straightforward way, since different important aspects need to be taken into account:

- First of all, the DVH requires a much smaller time step, it being explicit; on the contrary FVM is completely implicit and therefore the choice of the time step is based only on accuracy considerations. Because of the time constraint of the diffusion, low Reynolds number regimes strongly penalize the DVH with respect to the FVM as shown in Tables 8.2 and 8.3 for the test-case N°5.

- Secondly, the number of cells adopted for FVM is much smaller than the number of vortices for the DVH because the distribution of cells can be much easily controlled in the boundary layer region (i.e. $L/\Delta r$ with the FVM is grater than the DVH one, see first rows of Tables 8.2 and 8.3).
- Nevertheless, the wake region with the FVM has a lower resolution, as it was shown in figures 6.2 and 7.1. The DVH scheme has a self-adaptivity (i.e. vorticity formulation allows to discretize only the rotational region), while in the FVM the mesh must be designed in an optimum way with a-priori knowledge of the areas dominated by high velocity gradients.
- Finally, for the FVM, pre-processing for the mesh generation needs to be taken into account.

In conclusion, it can be observed that the CPU cost of DVH remains an issue for the explicit nature of the scheme. Also other particle methods, as for example the SPH, suffer of the same drawback. However, it is interesting that recently some researchers are moving in the direction of coupling the two methodologies in order to get benefits from each model. For example in the recent work of Palha *et al.* (2015) Palha et al. (2015) the FVM is used close to the solid body while a Vortex Particle Method is adopted in the wake region. This idea of coupling the Vortex

Test N°	Geometry	Re
1	Flow past a circular cylinder	4000
2	Flow past an elliptical cylinder with incidence	200
3	Flow past an elliptical cylinder with incidence	500
4	Flow past an elliptical cylinder with incidence	1000
5	Flow past a cylinder with triangular section	100
6	Flow past a cylinder with triangular section	1000

Table 8.1: The test-cases studied in the present work with both solvers DVH and FVM.

	Test N°1 Re=4000	Test N°4 Re=1000	Test N°5 Re=100	Test N°6 Re=1000
$L/\Delta r$ close to the body	400	200	100	200
N_{Max} vortices	253,000	397,000	290,000	348,250
N° iterations	600	11,300	28,400	45,390
$t_{end} U/L$	3	50	100	200
$\Delta t_a\, U/L$	$5\,10^{-3}$	$4.4\,10^{-3}$	$3.5\,10^{-3}$	$4.4\,10^{-3}$
CPU time (8 cores)	30 min	15 h	28 h	54 h
η (µs)	94	96	98	98

Table 8.2: DVH solver. CPU time costs for simulating four of the test-cases proposed in this work. Here L is the characteristic length of the problem.

	Test N°1 Re=4000	Test N°4 Re=1000	Test N°5 Re=100	Test N°6 Re=1000
$L/\Delta r$ close to the body	500	500	500	500
N_{Max} cells	262,200	290,800	188,400	188,400
N° iterations	300	5,000	10,000	40,000
$t_{end} U/L$	3	50	100	200
$\Delta t_a U/L$	10^{-2}	10^{-2}	10^{-2}	$5\,10^{-3}$
CPU time (8 cores)	15 min	3.6 h	3.4 h	24 h
η (μs)	92	71	51	92

Table 8.3: FVM solver. CPU time costs for simulating four of the test-cases proposed in this work. Here L is the characteristic length of the problem.

Particle Method with a mesh-based method was initially developed in the past by Cottet (1991) and by Ould-Salihi et al. (2001). Similarly for the SPH model the coupling with FVM has been recently developed (for more details see *e.g.* Marrone et al. (2016) and Chiron et al. (2018)).

Overall, the comparisons presented in this chapter clearly show the advantages of vortex particles methods for the simulation of unsteady viscous flows. It is important however to take into account also their disadvantages such as the difficulty to handle 3D problems where the stretching term is present in the vorticity equation and also the treatment of complex 3D geometries. Among other challenges, is their limitation to Direct numerical Simulation or their difficulty to represent highly anisotropic velocity gradients. For more information along these directions the interested reader can consult the work of Mimeau and Mortazavi (2021).

9

APPLICATION TO A PHYSICAL STUDY

The present chapter deals with the application of the method DVH to a physical study. The study presents the different regimes arising from the incompressible planar viscous flow past an elliptical cylinder. In order to highlight the effect of the different parameters on the onset of the regimes, two different aspect ratios are considered 0.10 and 0.40 and the angles of attack span from 0° to 90°, while the Reynolds number is gradually increased from 100 to 10000. The analyses are focused on the vorticity field and on the lift force acting on the ellipse. The different regimes are investigated and the route to chaos is established through different tools such as the Fourier spectra, phase space maps and Poincaré sections. The chapter is organized as follows: in section 9.1, a summary of the different test cases used is reported and the corresponding parameters are indicated; in section 9.2, an outline of the interaction mechanism between the shear layers is presented for circular and elliptical cylinders; in section 9.3, the conditions for which the steady regimes appear are discussed; in section 9.4, a wide description of the onset of different periodic regimes is carried out, pointing out the numerous natures of this behaviour (*i.e.* monochromatic, non-monochromatic and sub-harmonics); in section 9.5, the chaotic regime is presented; finally, in section 9.6, the global trends in terms of mean lift coefficients are outlined for every test matrix. The contents of this chapter were published in Giannopoulou et al. (2019b) and Durante et al. (2020a).

9.1 PROBLEM DESCRIPTION AND TEST MATRIX

The geometry considered for the test cases is an ellipse with two different aspect ratios where the Reynolds number or the angle of attack are the varying parameters. The aspect ratio AR is b/a where a and b are the major and minor axes respectively; the Reynolds number is defined with the major axis as $Re = Ua/\nu$, where U is the free stream velocity and ν is the kinematic viscosity. The Reynolds number spans an interval from 100 to 10000, while the angle of attack may vary from 0° to 90°.

The test matrix is composed by seven series, which were carried out with one parameter varying for each of them. In table 9.1, the series and their corresponding parameters are outlined while a more complete list of every simulation performed and the related regime found will be addressed in the table 9.2.

Test case	AR	α	Re
N1	0.40	0°	200 - 10000
N2	0.40	20°	100 - 10000
N3	0.10	0°	500 - 10000
N4	0.10	20°	100 - 10000
N5	0.10	30°	100 - 2000
N6	0.10	0° - 90°	2000
N7	0.10	0° - 90°	250

Table 9.1: Test matrix. The series N5 was already discussed in Rossi et al. (2018) and is here reproposed for the sake of completeness.

The 121 simulations have been carried out with DVH. The motivation for using DVH in the simulations is twofold. Firstly only the vortical part of the flow field is discretized and secondly, allows to achieve high resolution outcomes with reduced computational costs in comparison with other numerical methods.

The maximum Reynolds number was limited to 10000, because the transition to a chaotic condition appears in this range. The study of higher Reynolds numbers being at the moment out of the scope of this work, is left for future research.

In this work, the different regimes related to the variation of the incidence as well as of the Reynolds number for thick and thin ellipse will be investigated. The Reynolds numbers and the angles of attack, for which each regime was found to persist, are the maximum ones (among the simulated). For example in the table 9.2, where the overview of all the regimes is shown, the steady regime for the N1 case is found up to Re=200 while for the case N6 the steady regime is found up to $\alpha = 5°$.

The more severe issue related to the present investigations is the necessity to perform a large number of detailed simulations for very long time to be confident with the identification of the regimes. In fact, as discussed in section 9.4, a transitory condition could be attained for a significant time interval, before the onset of one or more bifurcations that move the system to a different regime. Also a detailed description of the wake field is also important in view of the regime evaluation (as stressed in the work of Durante et al. (2020b) and Kurtulus (2016)) and typical finite volume/finite differences methods suffer of severe numerical diffusion, so that the wake vorticity is hardly conserved unless very fine grids are used with a significant impact on the computational costs even in 2D frameworks. Because of the above considerations, the adoption of a VPM seems the best choice for these studies.

9.2 SHEAR LAYERS INTERACTION IN THE FLOW PAST AN ELLIPTIC CYLINDER

In a 2D framework, a strong link exists between the force time signals and the related vorticity field, when a typical flow regime is observed. The shear layers interaction at $1000 \leqslant Re \leqslant 10000$ (Re is referred to the diameter of the cylinder) point out the link between the near wake behaviour and the lift force in a simple case, where the typical parameters considered for an ellipse (*i. e.* thickness and angle of attack) are neglected.

Following Graziani and Bassanini (2002) and in Riccardi and Durante (2007) the global forces $\mathbf{F}_b$, acting on a body in steady motion, are related to the first momentum of the vorticity field:

$$\mathbf{M}(t) = \int_D d\mathbf{x}\, \mathbf{x}\, \omega(\mathbf{x}, t) \tag{9.1}$$

where D is the fluid domain. The relation with the forces $\mathbf{F}_b$ is given by:

$$\mathbf{F}_b = \rho \left[\frac{d\mathbf{M}^{\perp}}{dt} - \Gamma \mathbf{U}^{\perp} \right] \tag{9.2}$$

where Γ is the total circulation in the flow field and ρ the fluid density, while the symbol $\boldsymbol{\nu}^{\perp}$ is the perpendicular operator (*i.e.* if $\boldsymbol{\nu} = (\nu_1, \nu_2)$, then $\boldsymbol{\nu}^{\perp} = (-\nu_2, \nu_1)$). If the flow field starts form a rest condition, the circulation is zero at initial time and it remains zero for all the times, so that the straight relation holds:

$$\mathbf{F}_b = \rho \frac{d\mathbf{M}^{\perp}}{dt}\,. \tag{9.3}$$

The equation (9.3) links the vorticity field to the forces, thus, the time behaviour of $\mathbf{F}_b(t)$ is connected with the wake topology. For example, a periodic behaviour of the lift force is retractable in a well organized wake with large vortex dipoles (see *e.g.* Kurtulus (2016) and in Durante et al. (2020b)). Conversely, a chaotic behavior is associated with a chaotic distribution of vorticity in the wake. In section 9.4.3 we will discuss more in depth this point.

The dynamics in the near wake, when separation occurs, is dominated by the shear layers stability and their interaction, as pointed out by Zdravkovich (1997). Although the wake shed by an airfoil where the flow separates at the trailing edge can be investigated theoretically (see Riccardi and Durante (2007)), the general case of separated flows for the flow past bluff bodies is studied with experimental or numerical approaches. Even though some theoretical attempt started with Goldstein (1948), a convincing analytical development on this topic is still lacking, being the modeling of the shear layers and of their dynamics too complex for meaningful simplifications. However, in the recent years some effort in this sense was done by Serra and Haller (2017), and Serra et al. (2018).

Being the boundary layer over an immersed body a source of vorticity, flows past blunt bodies may be challenging to reproduce when the increase in Reynolds number induces thinning of the shed vortical structures and a severe instability of the shear layers, as visible in figure 9.1.

In figure 9.1 the shear layers are shown for Reynolds (referred to the diameter of the cylinder) from 1000 to 10000. At Re = 1000 the near wake shows large

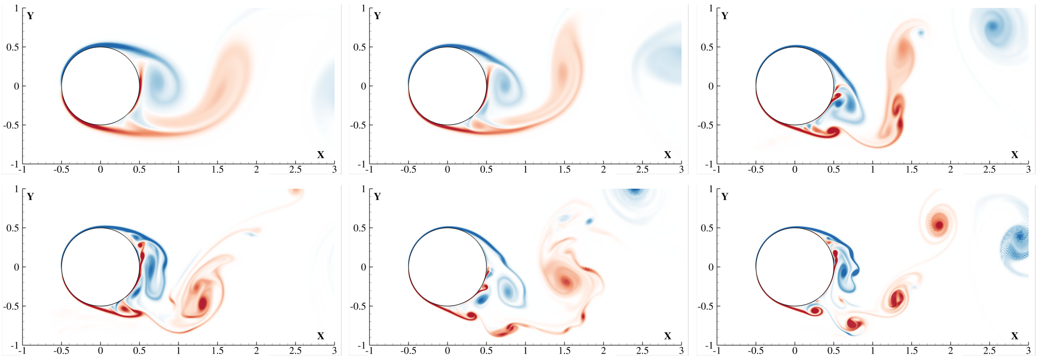

Figure 9.1: Non-dimensional near wake vorticity ω^* contours for the flow past a circular cylinder at maximum lift conditions. The contours are scaled from blue to red. From top left to bottom right: Re = 1000, 2000, 5000, 6000, 9000, 10000. For $Re = 1000$ the contour range is in ± 20, for $Re = 2000 - 6000$ in ± 25 and for $Re = 9000$ and $Re = 10000$ in ± 30. Different ranges are used to highlight the local interaction of the shear layers.

vortices with evident dissipation at just a half of diameter from the cylinder and low interaction between shear layers. Increasing the Reynolds the flow radically changes with layers roll up and transition to turbulence at $Re = 10000$. This behaviour is consistently observed in the lift force Fourier spectra in figure 9.2. The shear layers interaction at $Re = 1000$ induces a periodic behaviour and discrete spectrum (corresponding to the different harmonics of the periodic signal). Furthermore, a doubling period mechanism leads to the numerous discrete peaks of $Re = 2000$ spectrum. For higher Reynolds the complex shear layers interaction marks the transition from regular to chaotic regime, with the Fourier spectra passing from discrete to continuous.

In the left column of figure 9.3, the vorticity fields generated by a thick and a thin ellipse at $Re = 5000$ without incidence are depicted.

The proximity of the shear layers shows low interacting dynamics and the near flow field is periodic. The thick ellipse, exhibits a retarded separation with rolled layers that form a large dipoles wake and induce a periodic force time behaviour. The shape thinning at aspect ratio $b/a = 0.1$ enforces the prevention of boundary layer separation in a final laminar periodic regime (see Zdravkovich (1997)) and steady forces.

An aspect ratio different from 1 inevitably leads to add a new parameter because of the presence of the angle of attack at which the profile is set. The figure 9.3 shows in the right column both profiles at $\alpha = 20°$ and the intense shear layers interaction which induces, at the same Reynolds number, a chaotic vortex field in the wake. It should be underlined that a lower aspect ratio is characterized by higher curvature at leading and trailing edges (which became geometric singularities in the limit of a flat plate). At the leading edge the shear layer separates easier for $b/a = 0.1$, being the high curvature responsible for higher instability, as shown in the lower-right frame of figure 9.3.

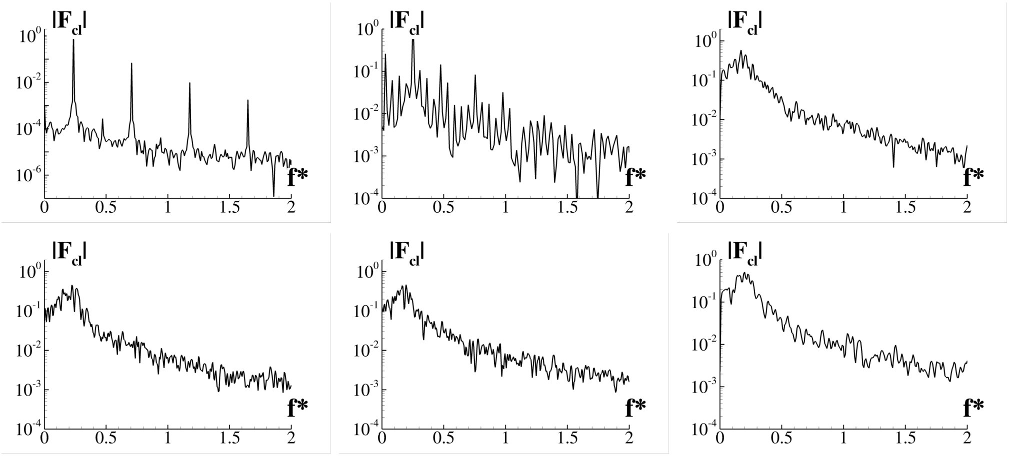

Figure 9.2: Fourier transform of the lift coefficient time signals referred to the cases in figure 9.1. From top left to bottom right: $Re = 1000, 2000, 5000, 6000, 9000, 10000$.

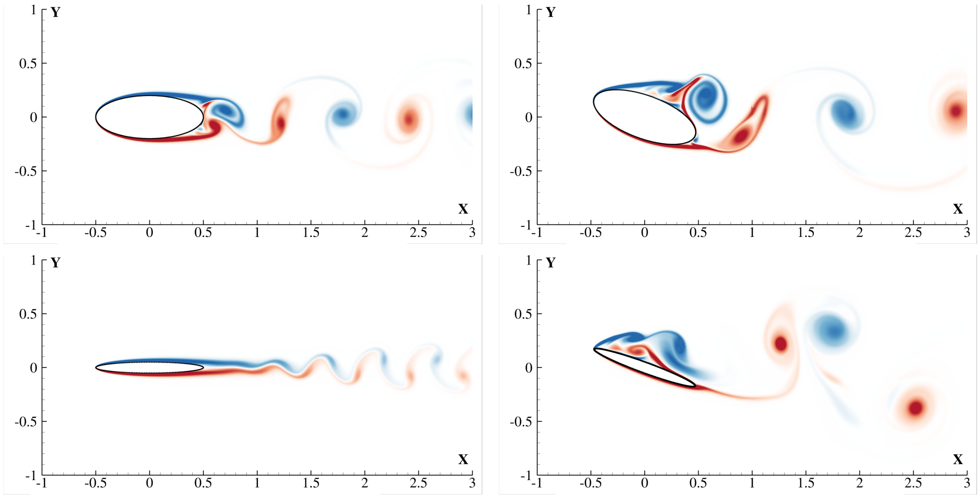

Figure 9.3: Effect of thickness and of angle of attack on the shear layers interaction. **Top-left**: $\alpha = 0^\circ$, $Re = 5000$. **Top-right**: $\alpha = 20^\circ$, $Re = 5000$. **Bottom-left**: $\alpha = 0^\circ$, $Re = 5000$ **Bottom-right**: $\alpha = 20^\circ$, $Re = 4000$. The non-dimensional vorticity contours are scaled from blue to red in the range $|\omega^*| \leqslant 20$ with the exception of the bottom-right, where $|\omega^*| \leqslant 25$.

9.3 STEADY REGIME

The steady regime of the flow past an immersed body is defined as the condition for which the forces acting on it are constant in time. For a circular cylinder (Zdravkovich, 1997), there is the *creeping flow* regime (Re<1) where the viscous forces are dominant and all disturbed regions of the flow are laminar with the flow attached to the surface. For $5 \leqslant \mathrm{Re} \leqslant 30 - 48$ a stable re-circulation region forms with two counter rotating vortices behind the cylinder. This region elongates with the increment of the Reynolds becoming unstable for $\mathrm{Re} \approx 50$ in the far wake ($\simeq 20c$), because of the instability of the confluence point. In this case, the flow is classified as steady, the forces being constant, but the Navier-Stokes equations would exhibit a periodic solution. Conversely to the potential solutions, found using conformal mapping techniques (see Batchelor (2000)), creeping flow solutions are not directly deducible, standing the Stokes paradox. The creeping flow solution is found using the Oseen approximation and the method of matched asymptotic expansions and was originally solved in Proudman and Pearson (1957). For the elliptic cylinder, the creeping flow solution was found in the pioneering work of Shintani et al. (1983) using the method of matched asymptotic expansions at $\alpha = 90°$. However, beside very few analytical works on this topic, a complete analysis of the Reynolds number range at which the transition toward the steady separation occurs still lacks.

Depending on the aspect ratio of the ellipse and on the angle of attack, increasing the Reynolds number leads to the formation of two distinct shear layers similarly to the cylinder steady separation regime. Unlike the cylinder, the existence of two parameters, make the Reynolds numbers at which the flow remains within the stable regime very wide.

In figure 9.4 four different configurations are shown. At $\alpha = 0°$ the lower the thickness, the higher the Reynolds number of steady separation. Indeed at $b/a = 0.4$ the flow remains steady at $\mathrm{Re} = 200$, but switches to periodic for slightly higher Reynolds values (at $\mathrm{Re} = 500$ the solution becomes periodic, see 9.4) while increasing the angle of incidence the steady regime is found up to Re=100.

Conversely for $b/a = 0.1$ the solution persists in this regime for up to $\mathrm{Re} \approx 3000$. However only the increment of the angle of attack ($20°$) poorly affects the maximum Reynolds number at which the steady regime persists, confining it up to to Re=200.

Thus with respect to the circular cylinder the Reynolds for which the steady regime persists is found to be very wide and the effect of the thickness is more important to suppress the flow into a steady condition.

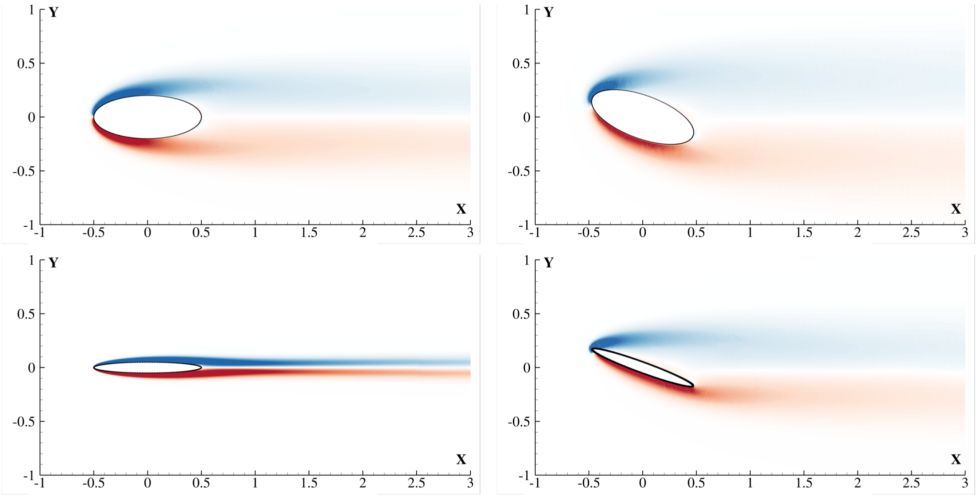

Figure 9.4: Vorticity contours (from blue to red and $|\omega^*| \leqslant 10$) for steady separation regimes in four configurations. **Top-left**: $Re = 200$, $b/a = 0.4$ and $\alpha = 0°$, **top-right**: $Re = 100$, $b/a = 0.4$ and $\alpha = 20°$. **Bottom-left**: $Re = 3000$, $b/a = 0.1$ and $\alpha = 0°$, **bottom-right**: $Re = 200$, $b/a = 0.1$ and $\alpha = 20°$.

Laminar regime

The laminar periodic wake regime, observed in the flow past a circular cylinder for $38 - 40 < Re < 180 - 200$, is here found for the thin ellipse for lower angles of attack. In figure 9.5 two cases are shown.

For the thin ellipse, at $\alpha = 20°$ the wake becomes slightly oscillating at $Re = 200$, becoming fully periodic at $Re = 300$ (as it will be discussed later). Conversely, at $\alpha = 0°$ the flow remains in steady regime up to $Re = 4000$, whereas the perturbations on the wake amplify, leading to the onset of a shedding mechanism.

For the thick ellipse, the laminar periodic regime never appears in the cases analyzed meaning either that this regime is too unstable to persist or it will for $100 < Re < 200$ at $\alpha = 20°$ and $200 < Re < 500$ at $\alpha = 0°$. However, it can be concluded that the thinning of the thickness plays a non trivial role in increasing the stability of this regime.

From the equation (9.3), in the steady regime, the first vorticity momentum is a linear function of the time being the wake dynamics determined by the linear elongation of the shear layers:

$$M_x(t) = -\frac{\bar{L}}{\rho}\, t\,, \qquad M_y(t) = \frac{\bar{D}}{\rho}\, t\,, \tag{9.4}$$

where $\bar{D}$ and $\bar{L}$ are respectively the constant drag and lift (the latter is not null when the incidence is different from zero, *i.e.*, there is not symmetry with respect to the x-axis).

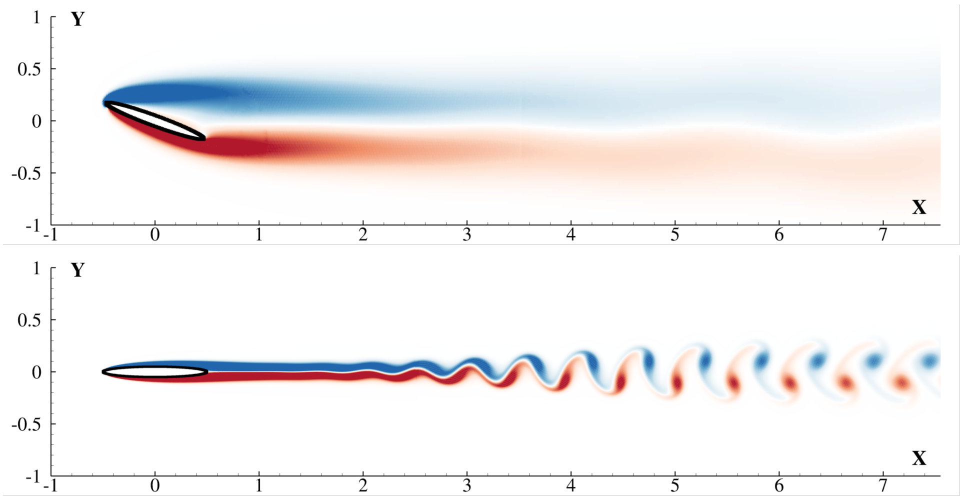

Figure 9.5: Vorticity contours (from blue to red and $|\omega^*| \leqslant 4$) for laminar periodic wake and $b/a = 0.1$ at $\alpha = 20°$ and $\mathrm{Re} = 200$ (**top**) and $\alpha = 0°$ and $\mathrm{Re} = 4000$ (**bottom**).

9.4 PERIODIC REGIME

When the incidence or the Reynolds number increase the shear layers start to interact leading to the onset of the periodic regime, known as von Kármán vortex shedding.

Depending on the ellipse thickness, as well as on the angle of attack, the periodic regime deserves a special attention because of numerous different conditions that may arise.

As shown for a NACA profile in Durante et al. (2020b) and in Rossi et al. (2018), the forces time behaviour (w.r.t. the lift force) is monochromatic, when the parameters are close to a steady condition, but evolves into a periodic non-monochromatic behaviour and may be eventually subjected to period bifurcations, as the angle of attack or the Reynolds number increases, a prelude to a chaotic transition (see also Pulliam and Vastano (1993), Kurtulus (2016)).

9.4.1 *Monochromatic signal*

Moving from the steady to the periodic regime, this is characterized initially by the regular shedding of vorticity the near wake. In some cases the periodic regime early manifests with a monochromatic behaviour of the global forces over the immersed body. For the circular cylinder, the forces time signal becomes monochromatic for $\mathrm{Re} \approx 100$ (Durante et al. (2017)), this being related to the regular shedding observed in the near wake with low interacting vortex dipoles.

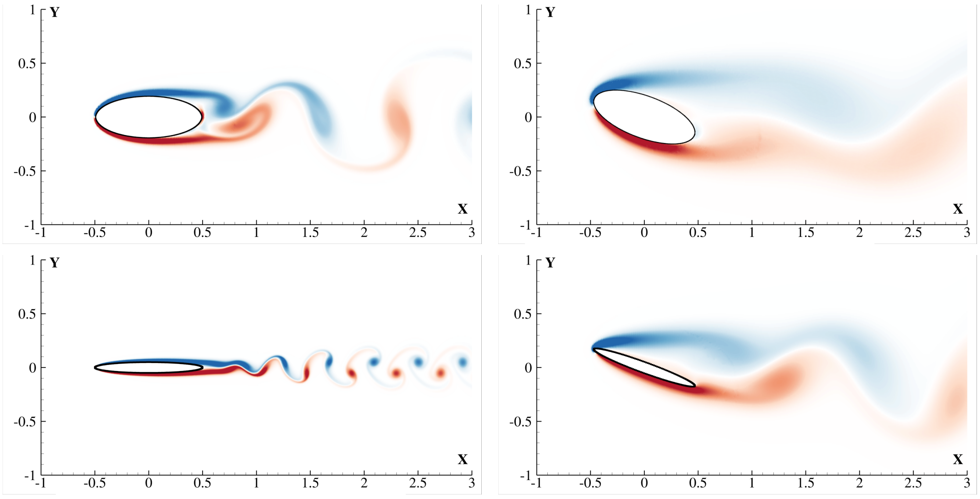

Figure 9.6: Vorticity contours (from blue to red) for monochromatic periodic regime at $\alpha = 0°$, $Re = 1500$ and $b/a = 0.4$ (**top -left** , $|\omega^*| \leqslant 15$); $\alpha = 20°$, $Re = 200$ and $b/a = 0.4$ (**top -right**, $|\omega^*| \leqslant 10$); $\alpha = 0°$, $Re = 7000$ and $b/a = 0.1$ (**bottom-left** , $|\omega^*| \leqslant 15$); $\alpha = 20°$, $Re = 300$ and $b/a = 0.1$ (**bottom-right**, $|\omega^*| \leqslant 10$)

For the ellipse similar behaviour is found in different configurations. In figure 9.6 the vorticity fields show a regular shedding, also for high Reynolds numbers when the angle of attack is zero.

Indeed, in the top-left frame the thick ellipse at $Re = 1500$ and $\alpha = 0°$ is depicted, whereas the thin one at $Re = 7000$ at the same angle of attack is shown at the bottom. Here the effect of the thickness (thinning) is to increase considerably the Reynolds number for which this regime persists, because it suppresses the vortex shedding to remain within a stable regime, in analogy to a flat plate. As it will be seen from the Fourier spectrum, this results in the global forces acting on the body being not only periodic but monochromatic.

As remarked also for the steady regime, the higher the incidence the lesser the stability of the regime. On the right column of figure 9.6, it can be seen that the shape influence on the persistence of monochromatic periodic regime is rather negligible. The maximum Reynolds numbers where it was found at 20° were $Re = 200$ for the thick and $Re = 300$ for the thin ellipse.

The corresponding Fourier transforms of the lift signals are depicted in figure 9.7, where a main signal peak, corresponding to the shedding frequency, is found.

For the circular cylinder ($b/a = 1$) the shedding frequency where the monochromatic behaviour is attained is about 0.163 at $Re = 100$ (see Durante et al. (2017); Zdravkovich (1997)). For the ellipse, from the left of figure 9.7 it results that the signal peak, corresponding to the shedding frequency, moves towards higher frequencies when the thickness is decreased, specifically for $b/a = 0.4$ it is found at $f^* = 0.59$ and for $b/a = 0.1$ to $f^* = 2.26$. This forward shifting of the maximum shedding frequency at which this regime appears, is the obvious consequence of

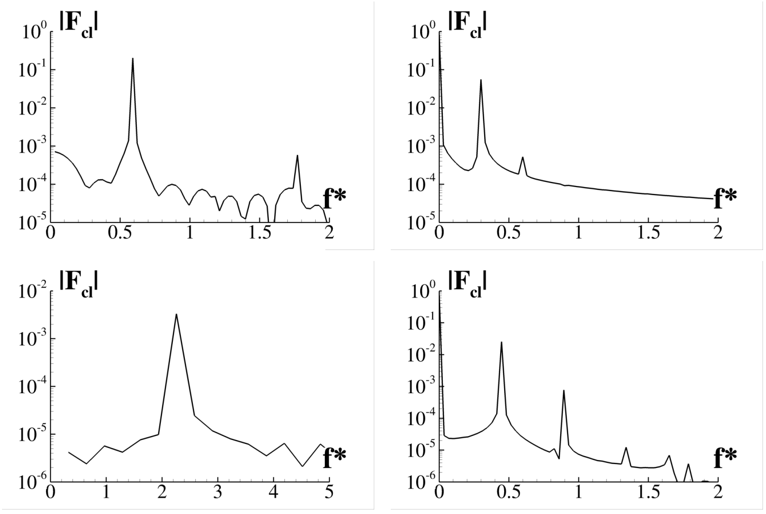

Figure 9.7: Fourier transform of the lift coefficient time signals referred to the cases in figure 9.6. $\alpha = 0°$, $Re = 1500$ and $b/a = 0.4$ (**top -left**); $\alpha = 20°$, $Re = 200$ and $b/a = 0.4$ (**top -right**); $\alpha = 0°$, $Re = 7000$ and $b/a = 0.1$ (**bottom-left**); $\alpha = 20°$, $Re = 300$ and $b/a = 0.1$ (**bottom-right**). The non-dimensional frequency is $f^* = c/(tU)$

the increasing Reynolds number at which it is found. Conversely, the amplitude lowers from 0.33 of the cylinder to 0.33×10^{-2} of the thin ellipse, this meaning that the shedding mechanism becomes faster and of lower intensity.

On the right, it can be seen that the increase of the incidence has a negligible effect on the shedding frequency: $f^* = 0.3$ for the thick ellipse and $f^* = 0.45$ for the thin one. On the log scale used for the plot of the transforms, the second peak for $f^* = 0.89$ found in the thin case, is ten times lower in amplitude, so that a monochromatic behaviour may be still assumed.

In the series N6 and N7, where the angle of attack is varied according to the table 9.1, the monochromatic behaviour was identified for $\alpha = 10°$ at $Re = 2000$ and at $\alpha = 20°$ for $Re = 250$, where the spectrum is very similar to the one depicted in the bottom-right frame of figure 9.7. This clearly confirms that the effect of the Reynolds number increasing is to lower the angle of incidence at which this regime appears. It is interesting that just at 15° of the series N6, the lift is already non-monochromatic. If the monochromatic behaviour persists over the 10°, it can within the narrow range $10° - 15°$ of incidence at $Re = 2000$.

In the periodic monochromatic regime the lift L and the drag D forces can be expressed as a simple sinusoid function:

$$L(t) = \bar{L} + L_0 \cos(2\pi f t + \phi_L), \tag{9.5}$$

$$D(t) = \bar{D} + D_0 \cos(4\pi f t + \phi_L), \tag{9.6}$$

where f is the shedding frequency, L_0 and D_0 are, respectively, the lift and drag amplitudes, and ϕ_L and ϕ_D are the corresponding phases. As well known, due to the alternating vortex wake, if the oscillations in lift force occur at the frequency f, the ones of the drag force occur at twice the frequency f.

According to equation (9.3), the first vorticity momentum is:

$$M_x(t) = -\frac{\bar{L}}{\rho}t - \frac{L_0}{2\pi f \rho}\sin(2\pi f t + \phi_L), \tag{9.7}$$

$$M_y(t) = \frac{\bar{D}}{\rho}t + \frac{D_0}{4\pi f \rho}\sin(4\pi f t + \phi_D). \tag{9.8}$$

Therefore, as in the steady regime, also in this special case an analytic expression, with few parameters, of the first order moment of the vorticity is available.

9.4.2 *Non-Monochromatic signal*

The onset of the periodic and non - monochromatic regime is characterized by the organization of the wake in a well ordered arrangement with big vortex patches emanating from the body. A similar regime was found for the cylinder at $Re = 1000$ and depicted in figure 9.1, where the alternate rolling up of the shear layers induces a local strain, which force the shed vorticity in detaching regularly, in coherent patches that form large and low interacting dipoles in the wake. The corresponding Fourier transform (figure 9.2) has a discrete-peaks spectrum, where every other peak corresponds to harmonics of the first one in a typical periodic way.

For the ellipse this behaviour is observed for the thick shape. At the top row of figure 9.8 a similar shedding mechanism is found for $\alpha = 0°$, whereas increasing the incidence ($\alpha = 20°$) results in the shear layers interacting mutually. The vorticity is shed in stretched filaments, which reorganize in large dipole structures persistent in the wake field up to 20-30 chord lengths.

The bottom row of figure 9.8 shows a shedding mechanism similar to the airfoil one observed in Rossi et al. (2018); Durante et al. (2020b), where the lower shear layer directly detaches and shed in the wake while interacting with the upper one, leading to higher stretching. This dynamics appears strikingly more regular in this case.

The lift coefficient time behaviour is depicted in the top row of figure 9.9 where, after a short transient, the regime appears with a regularly oscillating signal. Conversely, the thin ellipse depicted in the bottom row periodicity is attained after longer transients. In particular, for $\alpha = 20°$ and $Re = 1400$ the $b/a = 0.1$ shape manifests a more complex regime with a double peak in the lift signal before reaching (for $t^* > 50$) a straight periodic behaviour.

This behaviour can be understood by the corresponding vorticity field shown in figure 9.10, where the case $b/a = 0.1$, $Re = 900$ and $\alpha = 30°$ is shown. On the left frame, the time instant during the transient regime shows that vorticity consists of dipoles moving upwards and bending in the stream direction (similarly to the Mode IIIb observed for the NACA airfoil in Durante et al. (2020b)), while a different, compact arrangement is observed in the periodic regime.

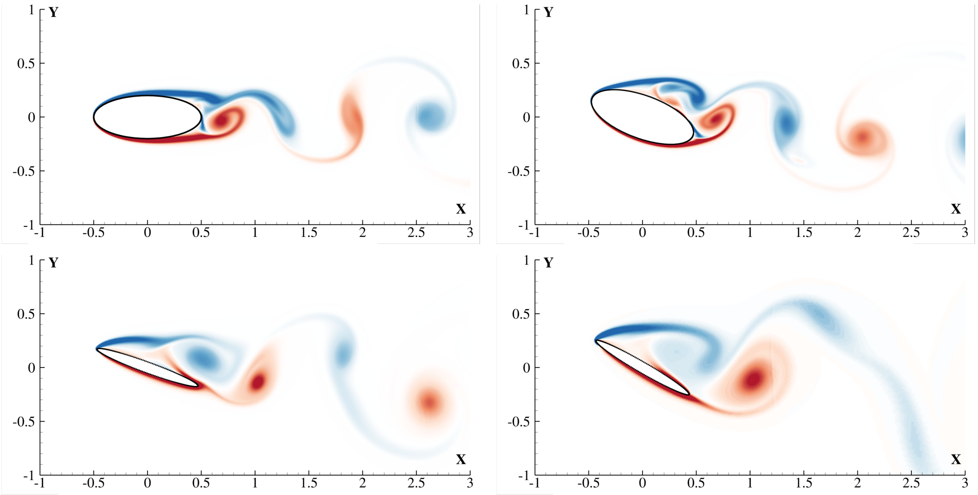

Figure 9.8: Vorticity contours for periodic regime at $\alpha = 0°$, $\mathrm{Re} = 2500$ and $b/a = 0.4$ (**top -left** , $|\omega^*| \leqslant 15$); $\alpha = 20°$, $\mathrm{Re} = 3000$ and $b/a = 0.4$ (**top -right**, $|\omega^*| \leqslant 20$); $\alpha = 20°$, $\mathrm{Re} = 1400$ and $b/a = 0.1$ (**bottom-left** , $|\omega^*| \leqslant 20$); $\alpha = 30°$, $\mathrm{Re} = 900$ and $b/a = 0.1$ (**bottom-right**, $|\omega^*| \leqslant 15$)

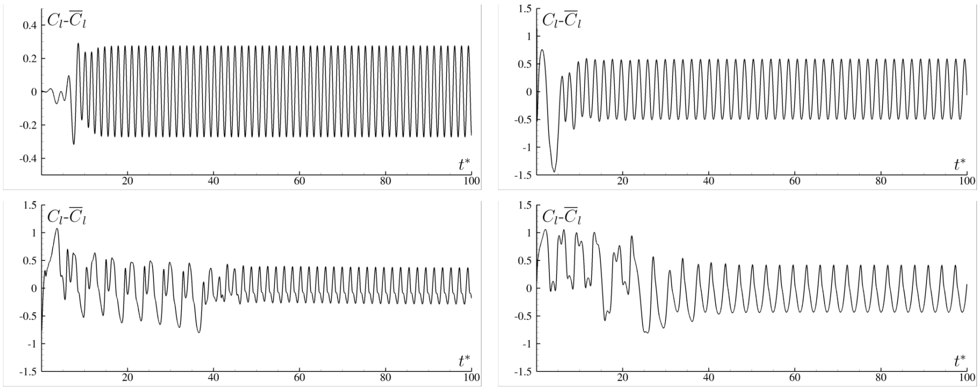

Figure 9.9: Lift coefficients time signals referred to the cases in figure 9.8. $\alpha = 0°$, $\mathrm{Re} = 2500$ and $b/a = 0.4$ (**top -left**); $\alpha = 20°$, $\mathrm{Re} = 3000$ and $b/a = 0.4$ (**top -right**); $\alpha = 20°$, $\mathrm{Re} = 1400$ and $b/a = 0.1$ (**bottom-left**); $\alpha = 30°$, $\mathrm{Re} = 900$ and $b/a = 0.1$ (**bottom-right**). The mean values have been subtracted for the sake of clearness. The non-dimensional time is $t^* = tU/c$

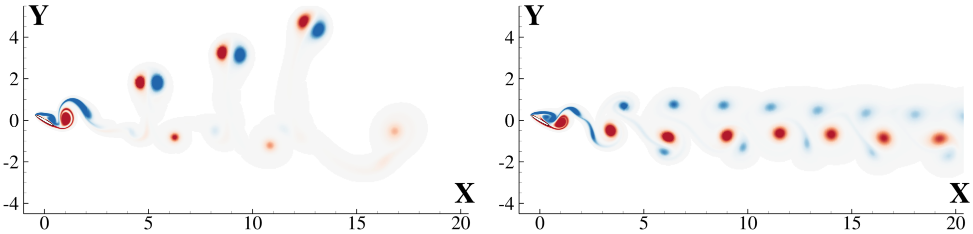

Figure 9.10: Vorticity contours ($|\omega^*| \leqslant 5$) for periodic regime at $\alpha = 30°$, $\mathrm{Re} = 900$ and $b/a = 0.1$. **left** $t^* = 32.5$, **right** $t^* = 97.25$

.

Thus the onset of a stable periodic regime is dependent on the thickness rather than the incidence. The corresponding Fourier transform in figure 9.11 depicts, coherently, the same scenario. For the thick ellipse, shown on the top, there is a principal peak related to the shedding frequency that is followed by higher harmonics of about two orders of magnitude lower indicating that, despite the high Reynolds numbers involved ($\mathrm{Re} = 2500$ for $\alpha = 0°$ and $\mathrm{Re} = 3000$ for $\alpha = 20°$), the signals are very similar to a sinusoid.

Although a nearly periodic behaviour for the thick ellipse at 0° was found up to $\mathrm{Re} = 10000$, the only case, after $\mathrm{Re} = 1500$, where a typical spectrum associated to a periodic behaviour is retractable is $\mathrm{Re} = 2500$, the other regimes show quasi-periodic nature, discussed in section 9.4.3.

Conversely for the thin ellipse, which was found to exhibit greater stability issues to reach a periodic condition, the spectrum has a discrete peak Fourier transform which however describes a periodic signal far from a sinusoid. The higher frequencies show peak amplitudes with low decay, with the second harmonics being of the same order with the first one. As it was mentioned for the thin ellipse a similar shedding mechanism is found for the case of a NACA airfoil in the works of Durante et al. (2020b) and Rossi et al. (2018) however with respect to the airfoil here the dynamics appear strikingly more regular.

The interesting conclusion of this analysis is that, conversely to the steady regime, the onset of a stable periodic regime is mainly dependent on the thickness rather than the incidence.

9.4.3 *Quasi-periodic behaviour thick ellipse* $\alpha = 0°$

The force behaviour for the thick ellipse at $\alpha = 0°$ has revealed some non trivial aspects.

Up to $\mathrm{Re} = 2500$ the flow was periodic, however in the interval $2000 \leqslant \mathrm{Re} \leqslant 10000$ the other simulations have shown clear peaks emerging from a very noisy spectrum resembling a chaotic regime, described later in section 9.5.

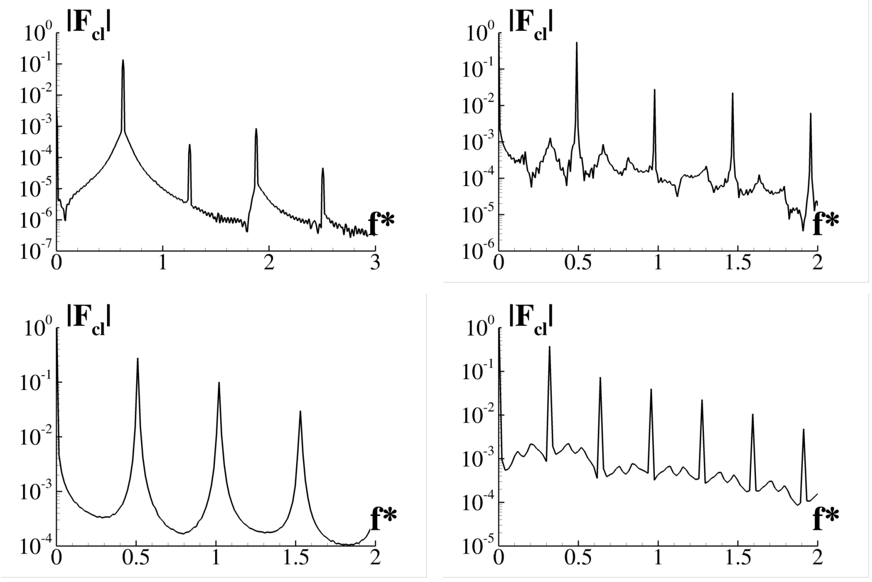

Figure 9.11: Fourier transform of the lift coefficient time signals referred to the cases in figure 9.8. $\alpha = 0°$, $Re = 2500$ and $b/a = 0.4$ (**top -left**); $\alpha = 20°$, $Re = 3000$ and $b/a = 0.4$ (**top -right**); $\alpha = 20°$, $Re = 1400$ and $b/a = 0.1$ (**bottom-left**); $\alpha = 30°$, $Re = 900$ and $b/a = 0.1$ (**bottom-right**). The non-dimensional frequency is $f^* = c/(tU)$

The spectra depicted in figure 9.12 show non-monochromatic periodic behaviour up to $Re = 2000, 3000$ and 4000. However from $Re = 5000$ and above a basic continuous spectrum can be seen and the periodic behaviour seems to be the carrier signal on which a chaotic modulation overlaps. These signals are known as *quasi-periodic*.

From the frequency ratio between the harmonic peaks, it was found that they are in a sequence 1-3-5 ... This means that the time signal is a periodic function with half-wave symmetry.

In order to show the chaotic underlying nature of the lift modulation, the case $Re = 7000$ was considered as an example. In 9.13 the vorticity field shows periodic shedding however the nonlinear local interaction of upper/lower boundary layers leads to fluctuations in the lift signal, drawn in the bottom.

By exploiting the property of half-wave symmetry, the original signal was added to the half-period shifted one and the noisy part is highlighted. With respect to the oscillation amplitude of the carrier signal, which is about $A = 0.3$, the noise is ten times lower in amplitude and possesses almost the same frequency. This means that the noise is a chaotic amplitude modulation and this finally explains why a typical periodic vortex shedding is seen. The chaotic nature is actually related to the fluctuations on the intensity of vortex patches released in the flow field and not to the shedding frequency.

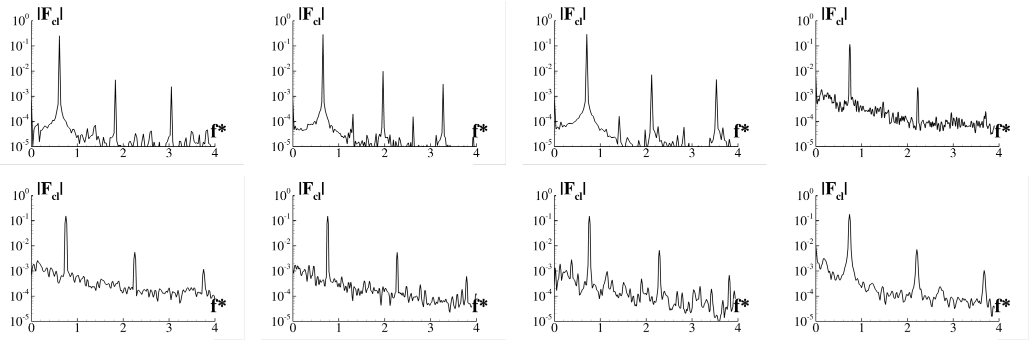

Figure 9.12: Fourier transform of the lift coefficient time signals referred to the cases $\alpha = 0°$ and $b/a = 0.4$. From left to right on **top**: $Re = 2000$, $Re = 3000$, $Re = 4000$ and $Re = 5000$. From left to right on **bottom**: $Re = 6000$, $Re = 7000$, $Re = 8000$ and $Re = 10000$. The non-dimensional frequency is $f^* = c/(tU)$

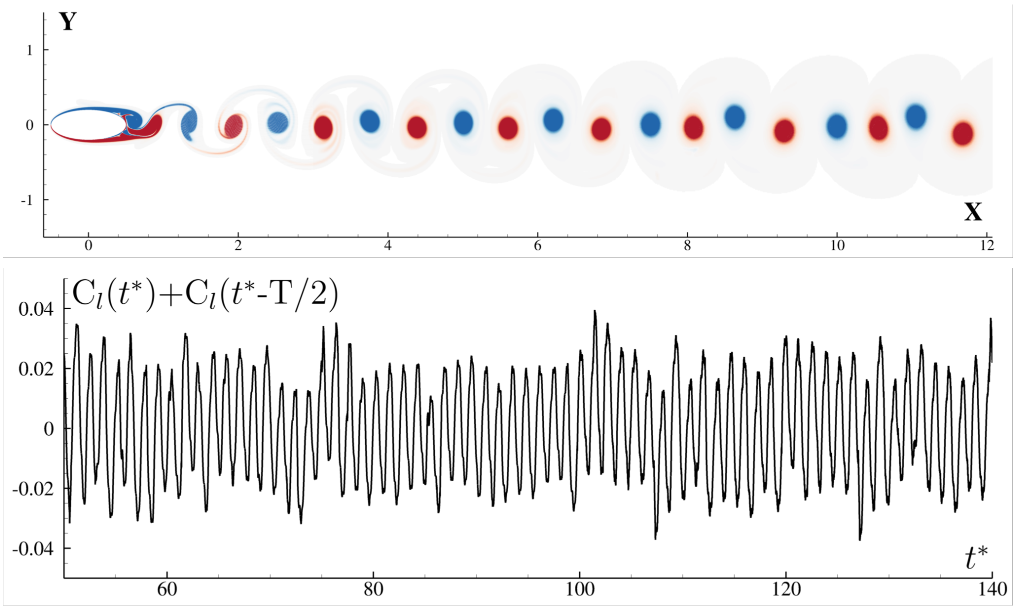

Figure 9.13: On **top**: vorticity field for $Re = 7000$, $\alpha = 0°$ and $b/a = 0.4$. The vorticity is contoured from blue to red for $|\omega^*| \leqslant 5$. On **bottom**: chaotic part of the lift signal for the same case, obtained exploiting the half-wave symmetry of C_l. The non-dimensional time is $t^* = tU/c$

This regime deserves further investigations and it will be matter of future works. Thus for this case we conclude that the system is represented by the following dynamics:

- Obtained bifurcation sequence: period-1 → quasi-periodic.

9.4.4 *Sub-harmonic modes*

Finally, the last regime before the chaotic is the sub-harmonic which is characterized by frequency modulation of the carrier harmonics.

Thin ellipse $\alpha = 20°$

This regime is first discussed for the case of the thin ellipse (*i. e.* $b/a = 0.1$) at $\alpha = 20°$ and varying Reynolds number (case N4)).

As it was shown previously (fig. 9.9 and 9.11) this case at $Re = 1400$ was periodic and the Fourier transform had a discrete peaks spectrum.

As sketched in figure 9.14, increasing the Reynolds number at $Re = 1450$, the lift signal changes abruptly and the previously discrete frequency spectrum is now characterized by numerous sub-harmonic peaks not sharp yet.

When the Reynolds number rises up to $Re = 1500$, the sub-harmonic peaks become more energetic in the spectrum, this being the effect of a radical change in the lift signal. Four peaks are visible in the lift period and this directly reflects on the spectrum shape. For every sharp peak in the spectrum of $Re = 1400$, shown in figure 9.11, four peaks appear thus this bifurcation represents a *period quadrupling*. In literature, Pulliam and Vastano (1993) observed numerous period doubling bifurcations for a NACA0012 at 20°, in particular for Reynolds number changing from 1400 to 1525, 1575 and 1580 and argued that this bifurcations were the evidence of a route to chaos. Additionally, in Durante et al. (2020b) numerous period tripling bifurcations were found before the chaos inception for a NACA0010 at varying angle of attack. To the authors' knowledge, a period quadrupling was never documented for the flow past an elliptical airfoil.

To understand better these phenomena classical tools from dynamical systems are used, such the phase - space maps and the Poincaré sections.

To construct the phase - space maps the $C_l, \dot{C}_l, \ddot{C}_l$ are used to reconstruct the phase space. Then the Poincaré sections are constructed as the intersections of the phase-space maps with the surface given by $\dot{C}_l = 0$ with $\ddot{C}_l < 0$. In this way the points on the Poincaré map are the local maxima of the lift time signal.

For visualization purposes here the phase-space maps are shown on the plane C_l-$\dot{C}_l$, however their construction is three-dimensional.

In figure 9.15 the corresponding maps for this case are shown. For $Re = 1450$ the Fourier analysis does not offer any particular insight beyond an unclear modulation. In contrast, the Poincaré section shows a period doubling identified through the two

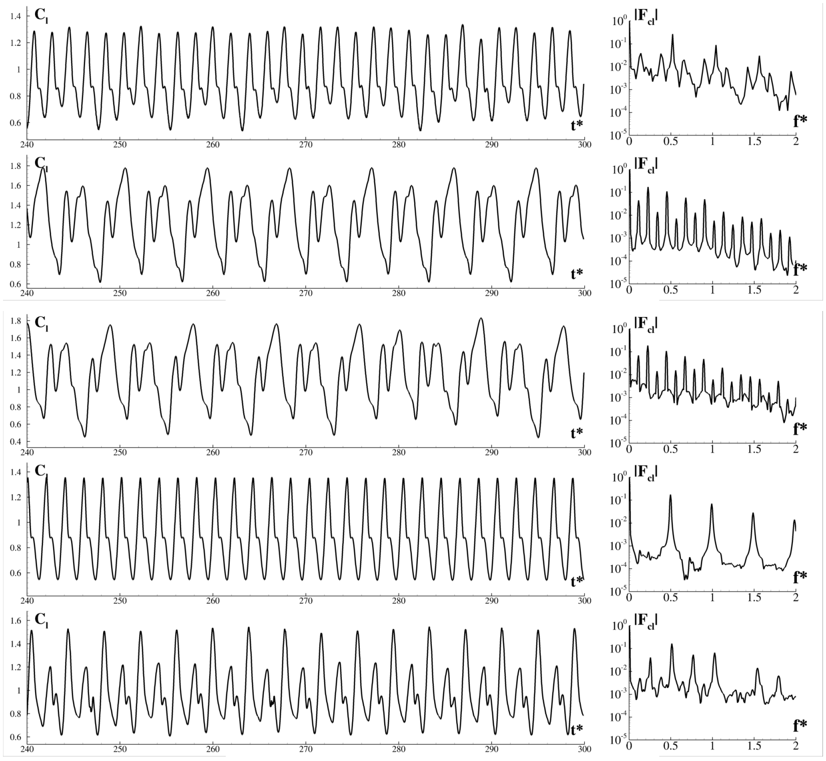

Figure 9.14: Lift signals (**left**) and corresponding Fourier transforms (**right**) for $b/a = 0.1$ and $\alpha = 20°$ at varying Reynolds number. From top to bottom: $Re = 1450$, $Re = 1500$, $Re = 1600$, $Re = 1700$ and $Re = 1800$. The non-dimensional time is $t^* = tU/c$, the non-dimensional frequency is $f^* = c/(tU)$.

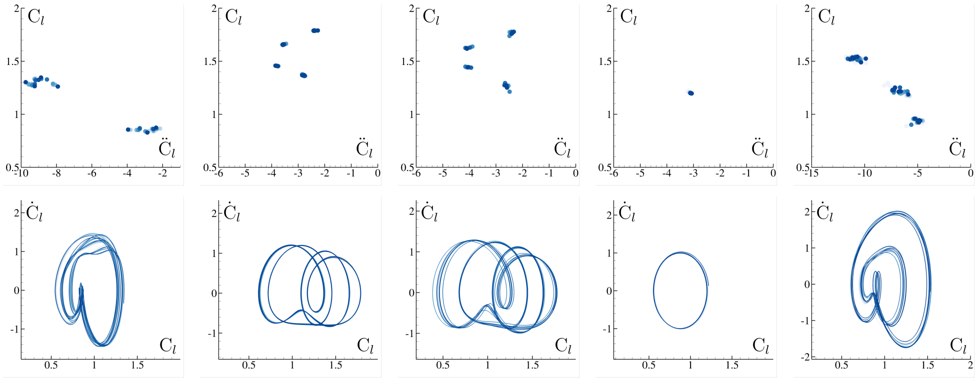

Figure 9.15: Poincaré sections (**top**) and phase maps (**bottom**) for $b/a = 0.1$ and $\alpha = 20°$ at varying Reynolds number. From left to right: $Re = 1450$, $Re = 1500$, $Re = 1600$, $Re = 1700$ and $Re = 1800$. The points, as well as the phase lines, are contoured with non-dimensional time in order to highlight the points and the curves clustering with the time.

groups of points well separated in the plane. The scattering around the two groups is due to the low frequency modulation of the signal. Similarly, the phase map shows a large orbit, corresponding to a periodic signal and a secondary knotted within the first marking the doubling.

For $\mathrm{Re} = 1500$ the signal and Fourier transform show the onset of a period quadrupling and this is also depicted in the Poincaré section where four distinct maxima groups are visible. Unlike the case $\mathrm{Re} = 1450$, the carrier signal is more regular and the phase map reveals four distinct orbits thus remarking the four different maxima found in the time signal period. The case $\mathrm{Re} = 1480$ is more complicated and interesting to discuss, and will be showed in the following paragraph 9.4.4. At $\mathrm{Re} = 1600$ the situation does not change much from the former with a lift signal shape, and coherently the Fourier spectrum, very similar to the $\mathrm{Re} = 1500$ case. The passage to $\mathrm{Re} = 1700$ marks the return to a straight periodic condition with a period halving primarily evidenced in the lift time signal resembling the 1400, a Fourier spectrum with discrete peaks at almost the same frequencies of $\mathrm{Re} = 1400$ (the gap is less than the 3%) and a Poincaré section with one single point. The last Reynolds after which the system is found to become chaotic is $\mathrm{Re} = 1800$ shown in the bottom of figure 9.14. From the time signal, three maxima are distinguishable in the period with one of them significantly lower in amplitude, corresponding to a *period tripling* and three peaks for every one of the carrier appear in the Fourier spectrum. This is confirmed by the Poincaré section and the phase map shown in 9.15.

From the above results it can be seen the importance of the Poincaré sections and phase maps covered for the classification the different bifurcations of the reference time signal.

Summarizing the above, we obtain the following bifurcation sequence:

- Obtained bifurcation sequence: period-2 → period-4 → period-1 → period-3.

CASE RE=1480 The case $\mathrm{Re} = 1480$, previously skipped deserves interest because of a significant instability before reaching periodic condition.

Figure 9.16 depicts different time ranges of the lift force and its spectrum from the initial time of the evolution up to the regime condition which is periodic. As shown in corresponding plot of figure 9.17, the regime condition corresponds to a compact arrangement of the wake (resembling the Mode IV regime of Durante et al. (2020b)) and the periodic behaviour of the lift force to one point in the Poincaré section and one orbit in the phase map.

This regime condition is found to be preceded by numerous bifurcations in time. In the time range $40 \leqslant t^* \leqslant 70$, the signal has two period maxima and a spectrum with the peak frequencies doubled in number with respect to the regime condition. The wake field in figure 9.17 is characterized by large dipoles emanating upwards and bending stream-wise. In the phase map two big orbits are visible and two point clusters in the Poincaré section.

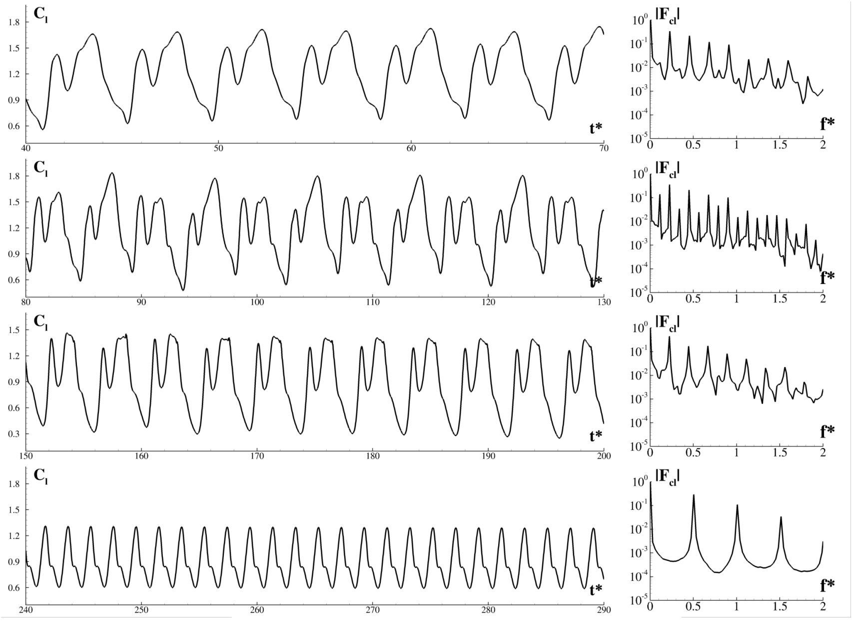

Figure 9.16: Lift signals (**left**) and corresponding Fourier transforms (**right**) for $b/a = 0.1$ and $\alpha = 20°$ at Reynolds number 1480 and different time ranges. The non-dimensional time is $t^* = tU/c$, the non-dimensional frequency is $f^* = c/(tU)$.

In the time interval $80 \leqslant t^* \leqslant 130$ the spectrum shows a period doubling bifurcation and the signal exhibits a period with five maxima, with two of them very close to each other. From the figure 9.17, a qualitative change in the vorticity is observed with large dipoles still emanating upwards but most of them bend in the opposite direction of the stream. Coherently, the Poincaré section shows five point , where two of them are very close in agreement with the time signal and the phase map shows four distinct orbits, doubled with respect to the former time range, in analogy with the Fourier spectrum.

In the time interval $150 \leqslant t^* \leqslant 200$ the behaviour is different where a period halving recasts the spectrum similar to that of the first time range. Two orbits exists in the phase map and two maxima groups in the Poincaré section. The wake transforms again and the dipoles are so bent that the wake becomes more compact. For $t^* > 200$, a new period halving brings the system to its regime condition.

It is worth to stress that, according to our investigation, this condition persists up to $t^* = 300$, but we have not a final proof that it indefinitely does. However, when this compact arrangement of the wake was found in different cases it is very stable (see, for example, the case shown in figure 9.10 or the perturbation study in Durante et al. (2020b)).

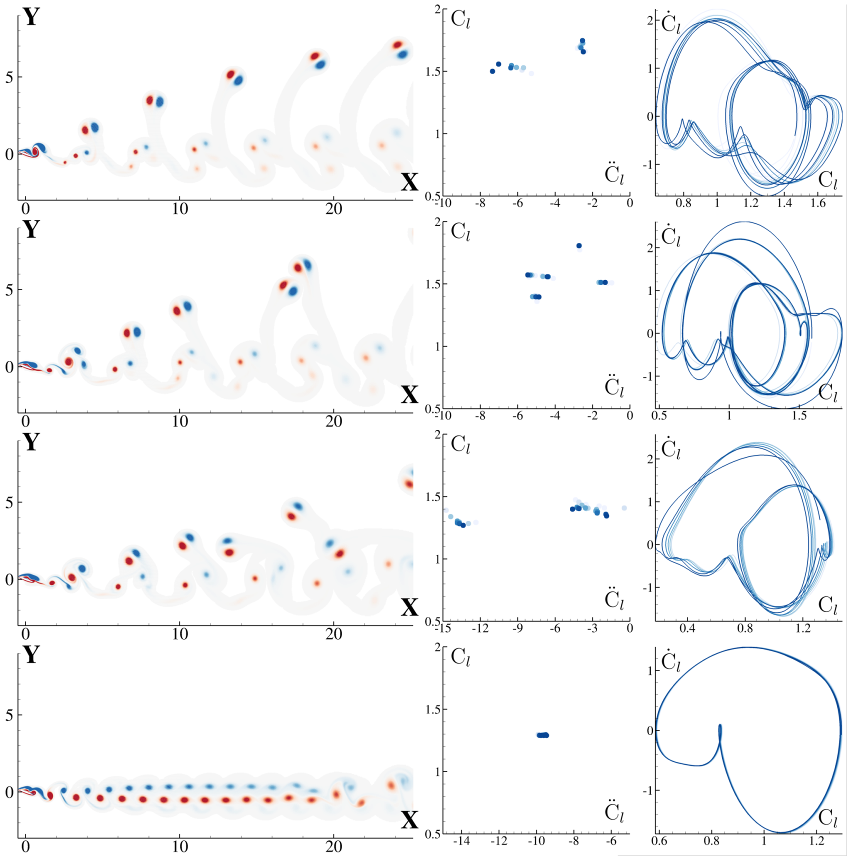

Figure 9.17: Vorticity fields (**left**), Poincaré sections (**center**) and phase maps (**right**) for $b/a = 0.1$ and $\alpha = 20°$ at Reynolds number 1480. From top to bottom: $t^* = 67.5$, $t^* = 150.0$, $t^* = 181.5$ and $t^* = 300.0$. The non-dimensional time is $t^* = tU/c$, the non-dimensional frequency is $f^* = c/(tU)$. The vorticity is contoured from blue to red for $|\omega| \leqslant 5$.

Thick ellipse at $\alpha = 20°$

In order to investigate the effect of the thickness on the onset of sub-harmonic regimes, a comparison with the case $b/a = 0.4$ at the same angle of attack is now presented. As depicted in figure 9.18, by increasing the Reynolds number the time signals shows evident modulations.

Conversely to the $b/a = 0.1$ the signal shape does not show radical changes remaining fairly regular and without bifurcations during the transient.

In the top row of figure 9.18, the lift time signal at $Re = 3000$ is periodic and monochromatic and the spectrum has discrete peaks, each one representing the higher harmonics of the carrier signal. The wake field in figure 9.19, shows a Von Kármán shedding with the vortex patches aligned along the direction connecting the stagnation points on the ellipse and one point in the Poincaré section.

For Re=3200, the signal undergoes to a slight frequency modulation that has no evident effects on the signal but is visible in the Fourier spectrum. The presence of two other peaks between the main ones of the basic signal show a tripling period bifurcation. The vorticity field in figure 9.19 depicts a near wake (up to 3-5 chords from the body) very similar to the former case, but more interacting vortex dipoles for a distance greater than 7 chords from the ellipse. Due to the close values of two lift maxima in the Poincaré section two point clusters are exhibited rather than three.

Increasing the Reynolds number, the tripling period bifurcation becomes more evident with sharp and greater peaks in the Fourier spectrum and a signal modulation in the lift time history. In figure 9.18 this behaviour is found when the Reynolds number passes from 3200, to 3500 and finally to 3800 where numerous frequency peaks lead the system toward a new bifurcation. The wake becomes more unstable with strong dipole interaction just after 5 chords, while in the Poincaré sections the lift maxima assume scattered distributions, not evidencing the bifurcations found in the Fourier transforms.

Higher Reynolds numbers (4000, 4100, 4200 and 4300 are plotted) make the signal even less regular, with a spectrum passing from the numerous discrete peaks to a single leading peak in an almost continuous spectrum as it is seen at the bottom row of figure 9.18). During this passage, the signal first exhibits irregular ranges of tripling period bifurcations alternated to more regular ones (this is the case of $Re = 4000$ and $Re = 4100$), but for highest Reynolds number (4300) the maxima variations during the numerous modulations appear less intense with respect to the time signal. This does not mean that the system assumes a more ordered configuration in terms of vorticity field and, in fact, the wakes becomes more and more irregular and the Poincaré sections become even more scattered.

In the next section, we will see that this mechanism will bring the system into a chaotic regime.

Thus the bifurcation sequence obtained for this case is through period tripling:

- Obtained bifurcation sequence: period-1 → period-3.

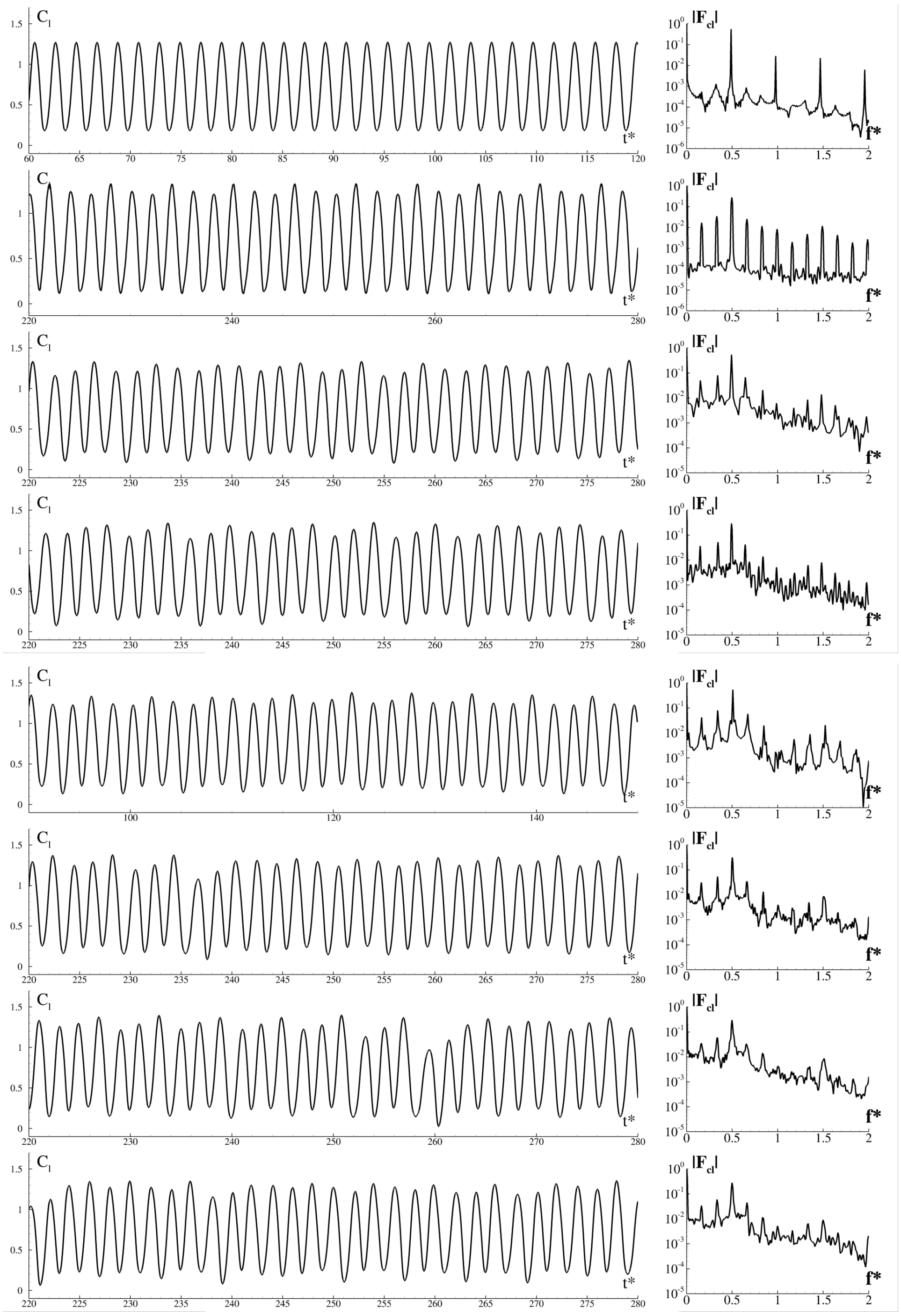

Figure 9.18: Lift signals (**left**) and related Fourier transforms (**right**) for $b/a = 0.4$ and $\alpha = 20°$ at varying Reynolds number. From top to bottom: $Re = 3000$, $Re = 3200$, $Re = 3500$, $Re = 3800$, $Re = 4000$, $Re = 4100$, $Re = 4200$ and $Re = 4300$. The non-dimensional time is $t^* = tU/c$, the non-dimensional frequency is $f^* = c/(tU)$.

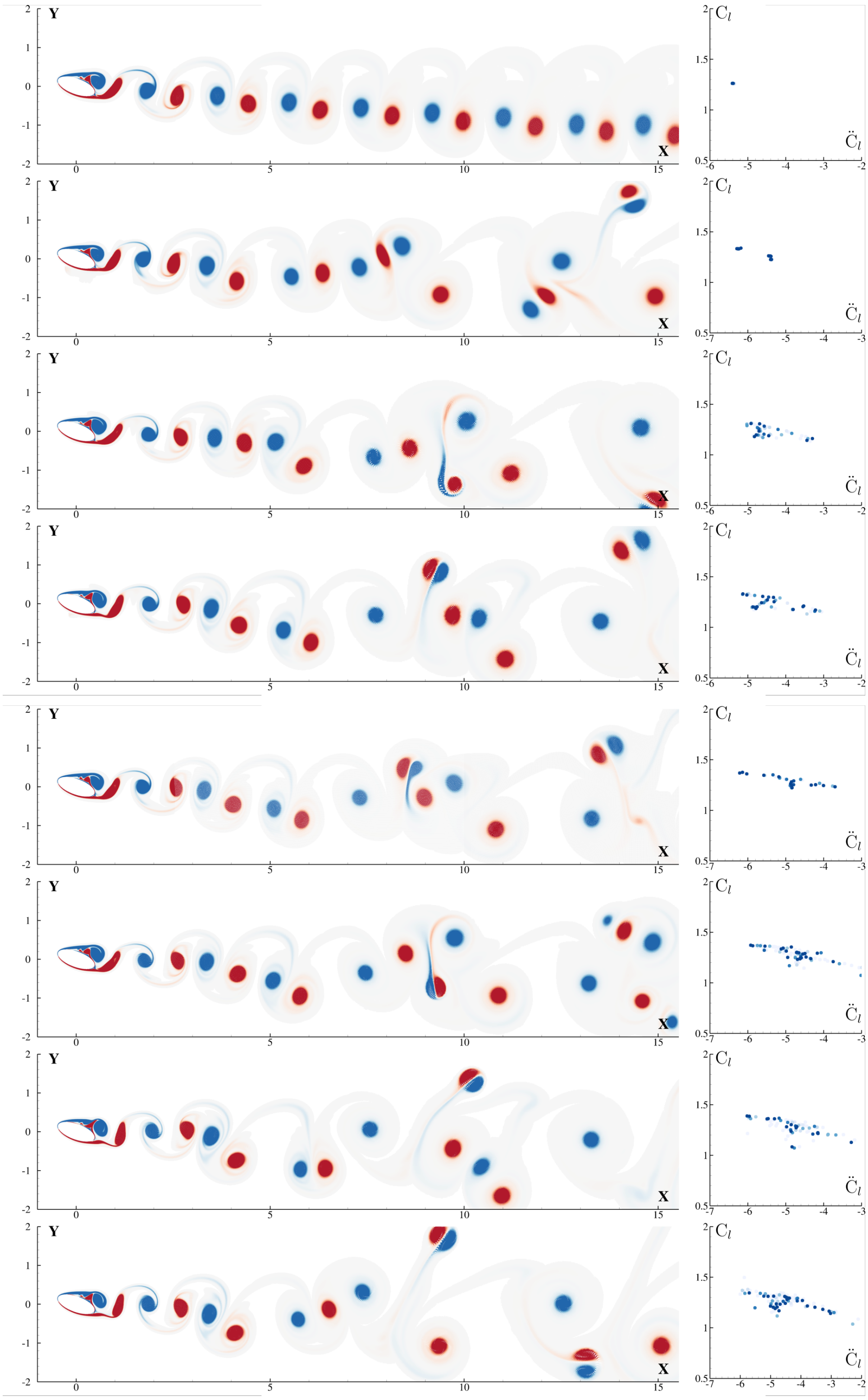

Figure 9.19: Vorticity fields (**left**) and related Poincaré section (**right**) for $b/a = 0.4$ and $\alpha = 20°$ at varying Reynolds number. From top to bottom: $\text{Re} = 3000$, $\text{Re} = 3200$, $\text{Re} = 3500$, $\text{Re} = 3800$, $\text{Re} = 4000$, $\text{Re} = 4100$, $\text{Re} = 4200$ and $\text{Re} = 4300$. The vorticity is contoured from blue to red for $|\omega| \leqslant 5$.

9.5 CHAOTIC REGIME

When dealing with a chaotic regime in the framework of the flows past rigid bodies, many possible conditions can be accomplished by the fluid flow. By looking at the lift time signal, a chaotic regime refers to a condition for which this signal is chaotic, *i.e.* its Fourier transform does not exhibits typical discrete-peaks spectra, as seen in the previous sections, but a continuous spectrum (as stressed in Durante et al. (2017, 2020b)). In the present study, the chaotic condition is achieved or by an unpredictable modulation of a periodic carrier, or by numerous bifurcations toward different regimes or by a completely random signal.

The passage from discrete to continuous of the spectra is the evidence of the route from a periodic regime to a non-periodic one where the frequencies involved belong to a continuous range. In a periodic regime only a numerable set of frequencies are excited, being them related to the scale of the eddies shed in the wake field. Conversely in the non-periodic regime the vorticity is shed through eddies of different scales.

As it was shown the effect of the angle of attack is to lower the Reynolds number at which the transition to chaotic regime occurs. Hence the present section is focused on the effect of the thickness, for which significant differences in the behaviour of the dynamical system appear (see also table 9.2).

Thick ellipse $\alpha = 20°$

This case is depicted in figure 9.20 for the passage from $Re = 4400$ to $Re = 6000$ is shown in terms of the lift signal and its Fourier transform. In the cases $Re = 4400$ and $Re = 4500$ the carrier signal bifurcates randomly toward a different state and this is found also in the Fourier spectra. The long persistence of the system on a regime with a regular lift time signal (see for $Re = 4400$ the time intervals $200 < t^* < 220$ or $250 < t^* < 280$, or for $Re = 4500$ the time intervals $200 < t^* < 230$) causes the presence of an evident peak at the shedding frequency of the carrier signal, but the presence of the bifurcations produces a continuous spectrum.

The Poincaré sections and phase maps in figure 9.21 makes the former discussion more complete and meaningful.

The first and second frame on the top left are characterized by an evident cluster of points, which are the maxima of the carrier signal, and other scattered points representing the bifurcation conditions. At $Re = 4400$ the phase map shows a nearly circular orbit, thus the fundamental regime is periodic. A large number of other orbits representing the time signal bifurcations discussed before allows to classify this behaviour as a strange attractor, according to the classical dynamical system theory.

Conversely, at $Re = 4500$, although the Poincaré section is rather similar to the former one, the phase maps tells something more: the system is basically shifting between two regimes represented by the two orbits visible in the map.

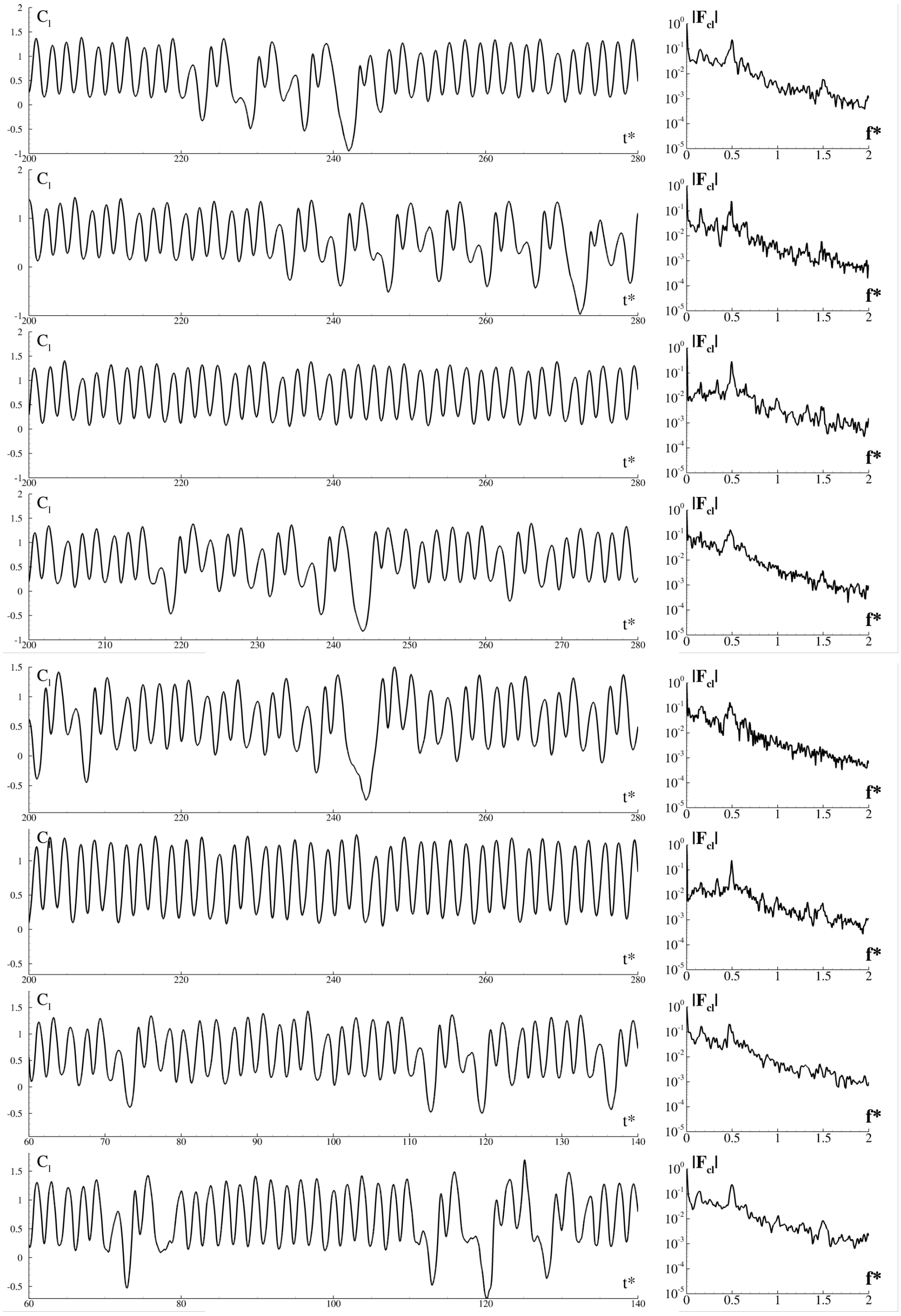

Figure 9.20: Lift signals (**left**) and related Fourier transforms (**right**) for $b/a = 0.4$ and $\alpha = 20°$ at varying Reynolds number. From top to bottom: $Re = 4400$, $Re = 4500$, $Re = 4600$, $Re = 4700$, $Re = 4800$, $Re = 4900$, $Re = 5000$ and $Re = 6000$. The non-dimensional time is $t^* = tU/c$, the non-dimensional frequency is $f^* = c/(tU)$.

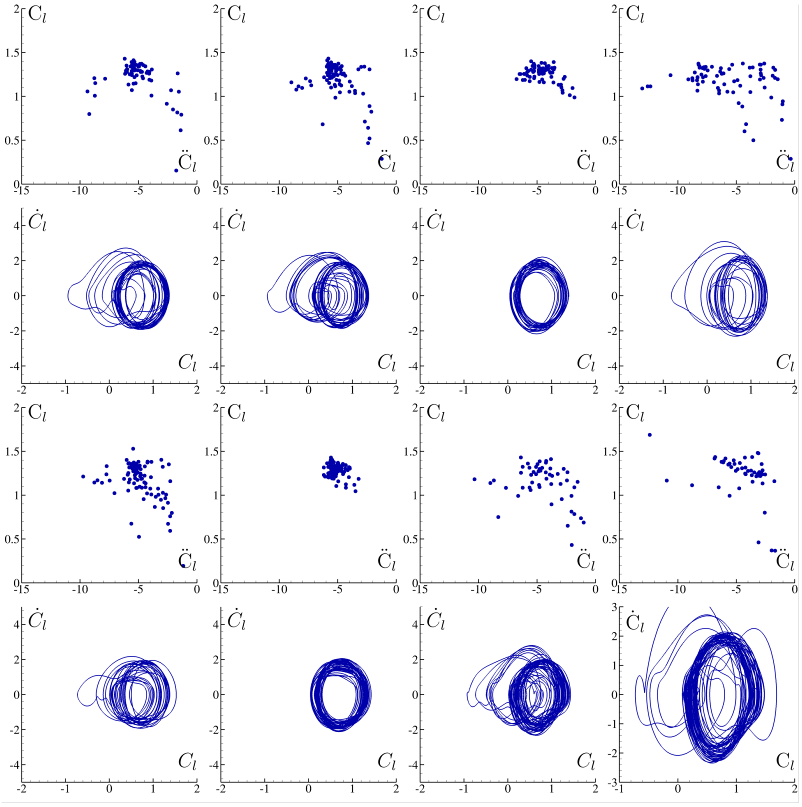

Figure 9.21: Poincaré sections (**dotted**) and related phase maps (**solid lines**) for $b/a = 0.4$ and $\alpha = 20°$ at varying Reynolds number. From top left to bottom right: $Re = 4400$, $Re = 4500$, $Re = 4600$, $Re = 4700$, $Re = 4800$, $Re = 4900$, $Re = 5000$ and $Re = 6000$.

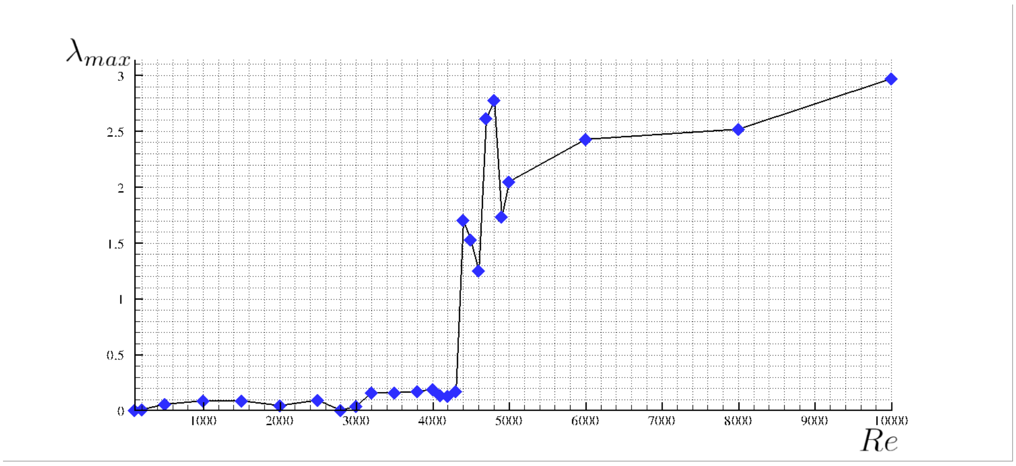

Figure 9.22: Maximum Lyapunov exponents for $b/a = 0.4$ and $\alpha = 20°$ for all the Reynolds number studied.

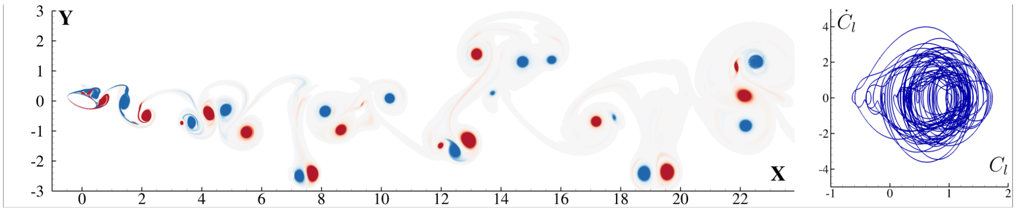

Figure 9.23: Vorticity field for $b/a = 0.4$ and $\alpha = 20°$ at $Re = 10000$ (**left**) and corresponding phase map (**right**). The non-dimensional vorticity contours are in the range $-4 \leqslant \omega^* \leqslant 4$.

When the Reynolds number rises to 4600 the system comes back to a more ordered condition. In this case, the lift time signal is not affected by bifurcations, although random modulations make the Fourier spectrum continuous with one sharp peak (see third frame from top of figure 9.20). Similarly, the Poincaré section and the corresponding phase map depicts a single point cluster and a single orbit, not sharp because of the modulations.

It is interesting to note how the system is moving toward a chaotic condition: the road is not straight with the Reynolds number increasing, but the system experiences direct and inverse routes.

Indeed, increasing further the Reynolds number at 4700 and 4800 the Poincaré sections show again scattered points distributions and numerous orbits in the phase maps (see the corresponding frames in figure 9.21). Similarly, the Fourier spectra of the time signals (shown in figure 9.20) are almost continuous and the main peaks themselves are hardly perceptible, conversely to the former cases. When the Reynolds number rises again, at $Re = 4900$, the system comes back to a more regular lift time signal, with a main evident peak at the shedding frequency in the spectrum and evidently clustered maxima in the Poincaré sections (see the related frame in figure 9.21).

Further increases of the Reynolds number bring the dynamical system to a non reversible chaotic condition, visible in the last frames of figure 9.20 and in the Poincaré sections and phase - space maps of figure 9.21, where a large number of orbits are obtained. In figure 9.23 the case $Re = 10000$ is depicted in terms of the vorticity field and phase - space map showing the chaotic nature of the flow field and of the phase - space map. When the phase - space map appears as intricate as in this case, a chaotic condition is attained.

This behaviour of the system towards the chaotic condition is found also in the values of maximum Lyapunov exponents. These describe the average exponential rate of separation or convergence of initially infinitesimally close trajectories in the phase-space. A positive maximum Lyapunov exponent signifies chaotic dynamics. In order to evaluate them here the algorithm introduced in Wolf et al. (1985) is exploited. In 9.22 the evaluated maximum Lyapunov exponents are shown for this test cases. As expected up to Reynolds 4300 the values are very close to zero. At Re=4400 the exponent attains a large value in accordance to the characterization of

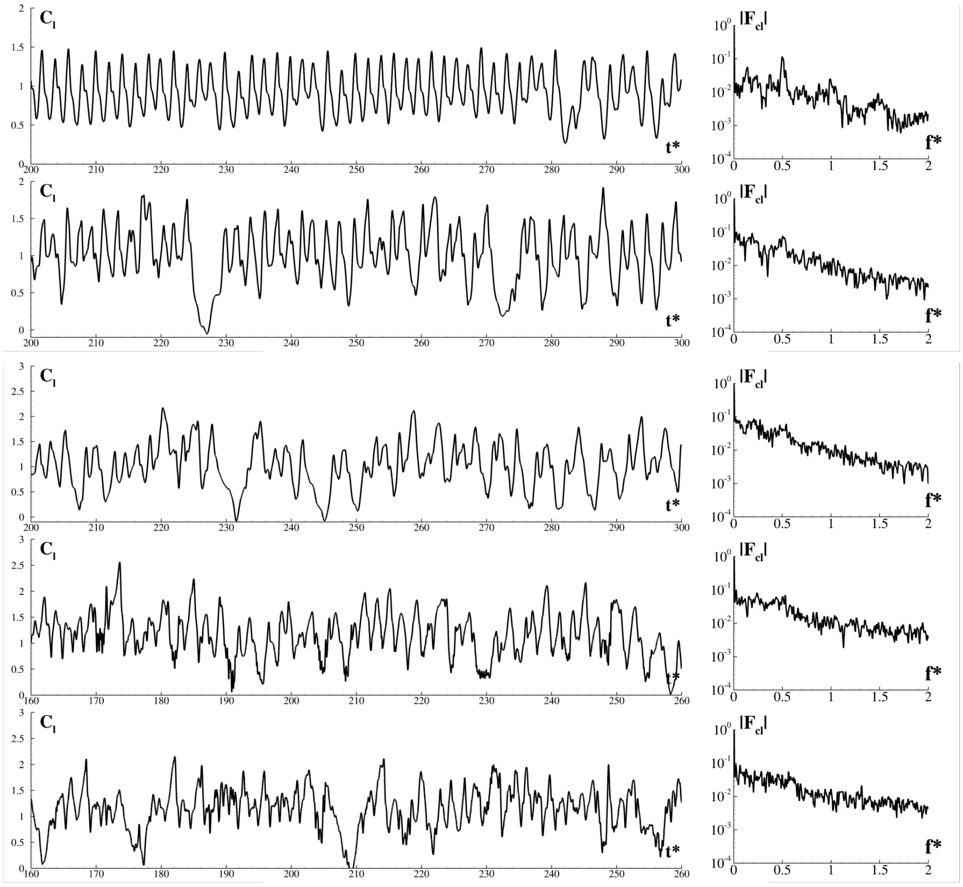

Figure 9.24: Lift signals (**left**) and related Fourier transforms (**right**) for $b/a = 0.1$ and $\alpha = 20°$ at varying Reynolds number. From top to bottom: $Re = 2000$, $Re = 3000$, $Re = 4000$, $Re = 6000$ and $Re = 10000$. The non-dimensional time is $t^* = tU/c$, the non-dimensional frequency is $f^* = c/(tU)$.

the system as chaotic at this Reynolds number. After this, a drop in the value of the exponent is found at Re=4600 as also supported by the corresponding phase-space map and the Poincaré section shown in figure 9.21. Then the value of the exponent again increases up to Re=4800 and drops again when Re=4900. For any other increase of the Reynolds the exponents are increasing. Thus the trend in the chaotic behaviour shown in figure is also found in the maximum Lyapunov exponents.

Thin ellipse $\alpha = 20°$

For the thin ellipse ($b/a = 0.1$) the system presents chaoticity for a significantly lower Reynolds. In the top frame of figure 9.24, the lift time signal at $Re = 2000$ is shown together with its Fourier transform.

The carrier signal is still recognizable and similar to the case $Re = 1450$ (figure 9.14 top) although affected by high noise. The spectrum exhibits an evident peak,

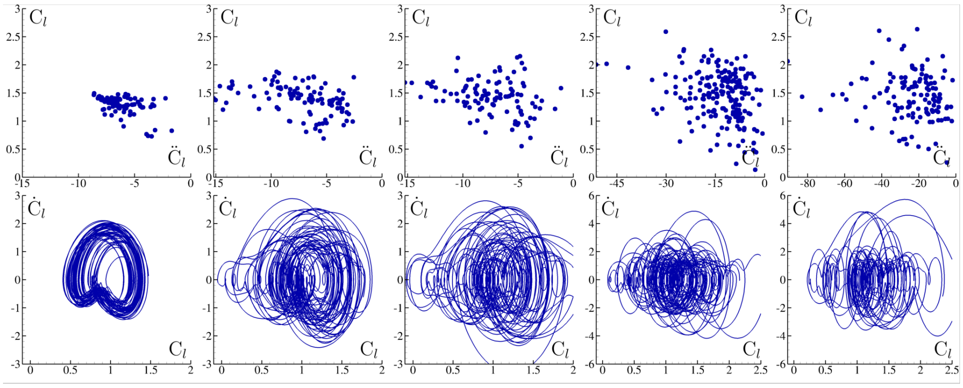

Figure 9.25: Poincaré sections (**top**) and related phase maps (**bottom**) for $b/a = 0.1$ and $\alpha = 20°$ at varying Reynolds number. From left to right: $Re = 2000$, $Re = 3000$, $Re = 4000$, $Re = 6000$ and $Re = 10000$. The plot intervals of Poincaré sections at $Re = 6000$ and $Re = 10000$ are widened in abscissa to cover the whole range of curvatures.

but conversely it does not share any similarity with the $Re = 1800$ (figure 9.14 bottom) shown in the previous section.

As seen before for the thick ellipse, the presence of a peak in the Fourier spectrum translates into a point clustering in the Poincaré section even in this case (see $Re = 2000$ in figure 9.25) and also the phase - space map shows a blurred orbit.

The Poincaré sections, are confined in the C_l range, but are very scattered along $\ddot{C}_l$. This is in coherence with the fact that in chaotic conditions the lift experiences larger variations in curvature rather than in amplitude.

From now on, any other increase of the Reynolds number results in the lift signal having a completely continuous spectrum and at $Re = 10000$ it resembles more to *pink noise*.

This kind of noise is often found in the statistical fluctuations of a wide number of diverse physical and biological systems (see Handel and Chung (1993)) and it is based on a characteristic behaviour of the Power Spectrum Density (PSD) which assumes a trend:

$$S_x(f) \approx \frac{1}{f^\beta}, \quad \text{for} \quad 0 < \beta \leqslant 2. \tag{9.9}$$

The PSD spectrum is a useful tool to analyze a time signal in the frequency domain because it describes the power contained in a frequency. Thus when the signal is periodic low frequencies will emerge from the PSD spectrum. On the contrary, high frequencies will flatten the PSD in chaotic signals which are characterized by continuous spectra. In order to get the PSD spectrum, the autocorrelation functions have been deduced from the time signals of figure 9.27 and

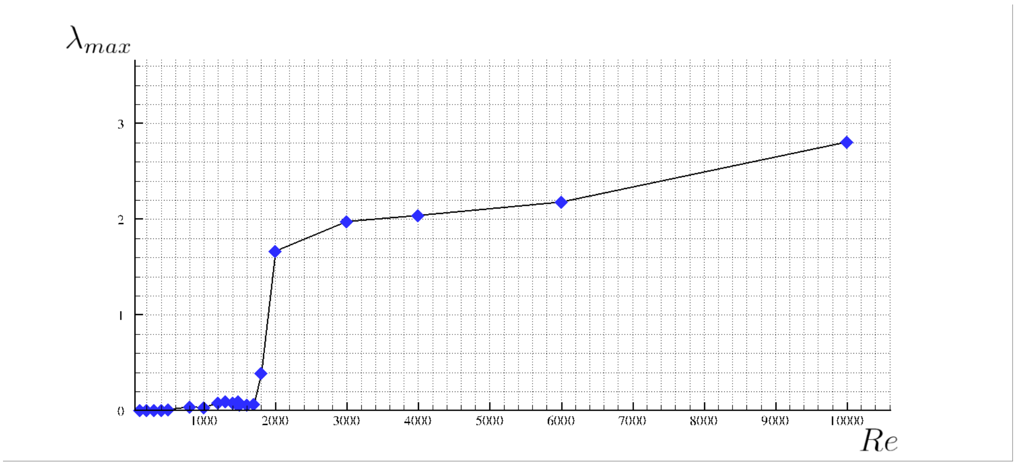

Figure 9.26: Maximum Lyapunov exponents for $b/a = 0.1$ and $\alpha = 20°$ for all the Reynolds number studied.

the Wiener-Khinchin theorem (Wiener, 1964) has been used. The autocorrelation function measures a signal's self-similarity versus delay and is defined as:

$$R_x(T) = \frac{\overline{x(t)x(t+T)}}{\overline{x(t)^2}}, \tag{9.10}$$

where T is the time frame within which the autocorrelation and x refers to the time signal of the lift. The average is evaluated as:

$$\overline{x(t)x(t+T)} = \lim_{T\to\infty} \frac{1}{T} \int_0^T x(T)x(t+T)\,dt \tag{9.11}$$

$$= \lim_{N\to\infty} \frac{1}{N} \sum_{n=1}^{\infty} x(t_n)x(t_{n+1}). \tag{9.12}$$

The PSD is obtained from the autocorrelation function using the Wiener-Khinchin theorem (Wiener, 1964), which is the cross correlation theorem of a function with itself. The PSD is obtained as:

$$S_x(f) = \int_{-\infty}^{\infty} R_x(T)\, e^{-2\pi i f T}\, dT. \tag{9.13}$$

As sketched in figure 9.27, at $Re = 2000$ a periodic signal exists for low frequencies, this being visible from the evident peaks for $f^* < 1$, but it follows a pink noise trend $\approx 1/f^*$ with $\beta = 1$ for higher frequencies, highlighted with dashed lines. A similar situation holds for Reynolds going from 3000 to 6000 where the embedded periodic patterns are even less evident. At $Re = 10000$ the spectrum remains in the trend with $\beta = 1$, but the periodic patterns are rather absent, as expected. As described for the case of the thick ellipse in the chaotic regime, also in this case the maximum Lyapunov exponents depicted in figure 9.26 follow an increasing trend,

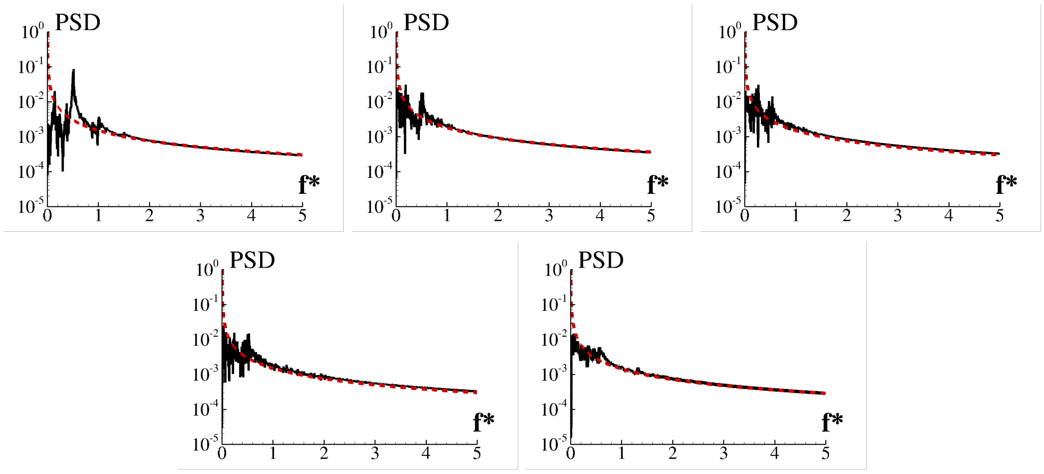

Figure 9.27: Power spectrum densities (solid) and asymptotic behaviours (dashed) for $b/a = 0.1$ and $\alpha = 20°$ at varying Reynolds number. From top left to bottom right: $Re = 2000$, $Re = 3000$, $Re = 4000$, $Re = 6000$ and $Re = 10000$. The non-dimensional frequency is $f^* = c/(tU)$.

consistently with the increasing chaoticity found in the Poincaré section and the phase-space maps as these were shown in figure 9.25.

In order to better understand the chaotic regime in figures 9.28 and 9.29 the Re=6000 and Re=10000 are shown. On the top frame, is the magnification of the lift together with time instants sketched below.

The elliptical airfoil here works in the so called stalled conditions. This is essentially the occurrence of flow separation at the leading edge that causes significant and prolonged reduction of the lift force. The first frame shows at a lift peak large scale eddies (*i.e.* around one fifth of the chord length) are shed in the wake field and a trailing edge vortex patch is bent upstream with a large dipole at 2 chords of distance. The lift drop observed after the first frame is accompanied by an important instability at the trailing edge where a big vortex with positive vorticity (red) forms and remains displaced in correspondence of the suction side (the upper side of the airfoil characterized by high velocity and low static pressure). In frames 3 and 4 it becomes clear that the couple of vortices, coming from the leading edge (negative) and from trailing edge (positive), induces a force normal to the airfoil pushing it downwards, resulting to the observed drop in the lift force. When this vortex moves downstream, the lift rises up again corresponding to the frame and time instant 6. In figure 9.29, the dynamics observed for $Re = 10000$, are the same. However due to the increased Reynolds number the trailing edge vortex is more complex, surrounded by dipoles forming a *necklace* around it. This richness in different scales emerging in correspondence of the airfoil surface are responsible of the corresponding chaotic nature of the lift force.

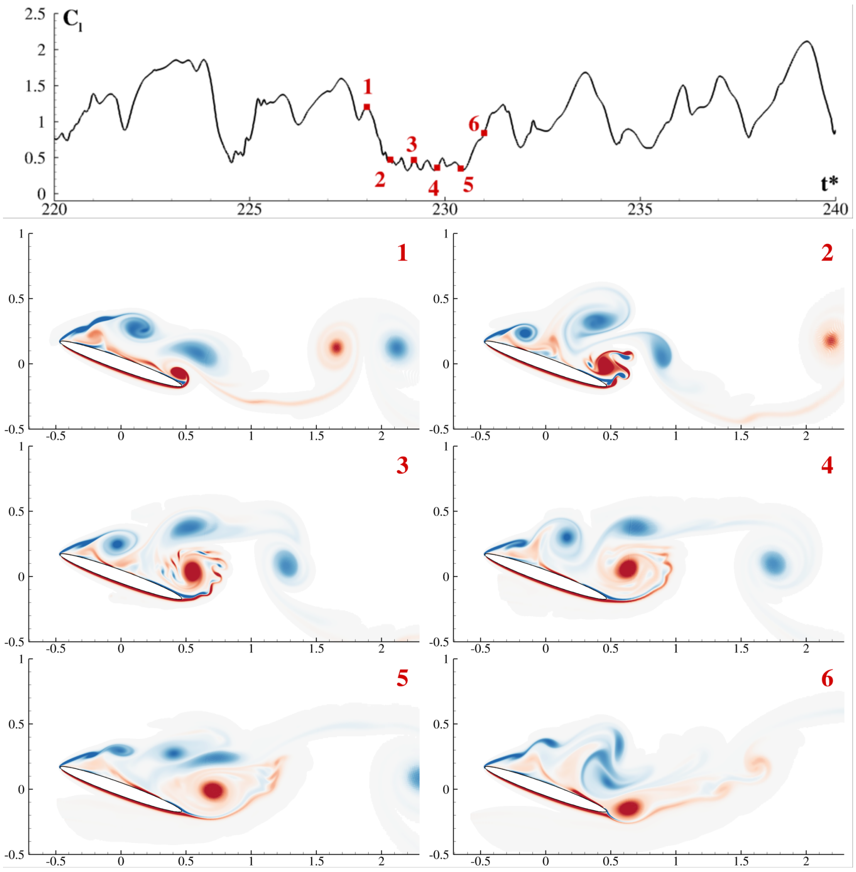

Figure 9.28: Lift signal for $b/a = 0.1$, $\alpha = 20°$ and $Re = 6000$ with the six time instants highlighted. The non-dimensional time is $t^* = tU/c$. The corresponding vorticity fields are depicted below. The non-dimensional vorticity contours (from blue to red) are in the range $-35 \leqslant \omega^* \leqslant 35$.

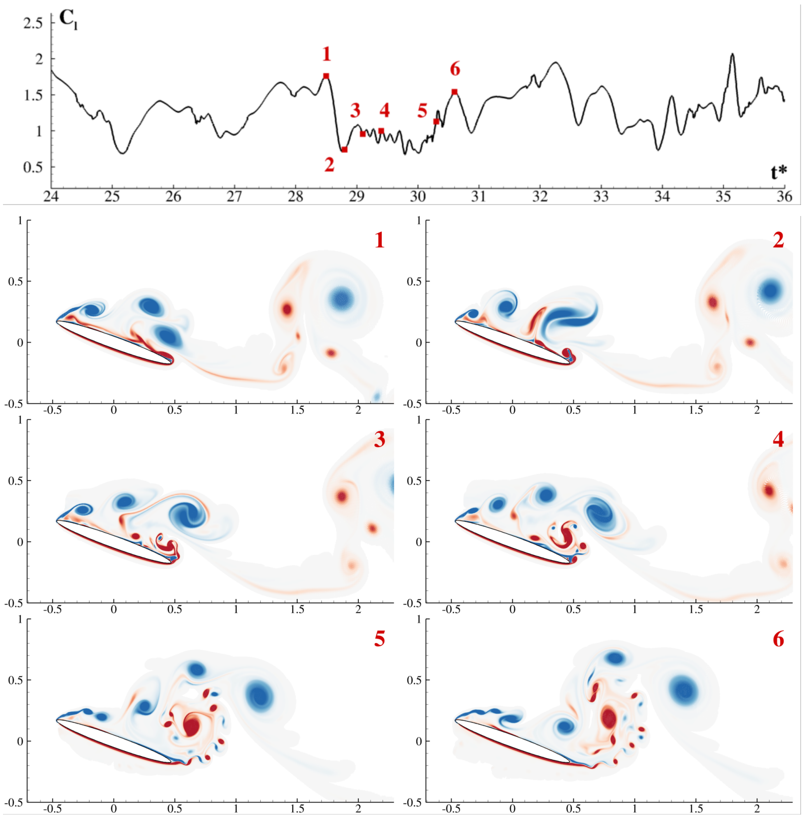

Figure 9.29: Lift signal for $b/a = 0.1$, $\alpha = 20°$ and $Re = 10000$ with the six time instants highlighted. The non-dimensional time is $t^* = tU/c$. The corresponding vorticity fields are depicted below. The non-dimensional vorticity contours (from blue to red) are in the range $-35 \leqslant \omega^* \leqslant 35$.

9.6 GLOBAL BEHAVIOUR

In the present section a general discussion on the mean lift coefficient $\overline{C}_l$ variation related to the Reynolds number or to the angle of attack is carried out and discussed according the simulation matrix presented in section 9.1.

By considering that the mean lift is zero for all the cases at $\alpha = 0°$, the series N1 (thick case) and N3 (thin case) will not be considered.

In figure 9.30, two frames are related to the thick (series N2) and thin (series N4) cases for $\alpha = 20°$ with remarkable differences between them.

As expected, the thick ellipse is less lifting than the thin one with only one maximum around 0.72 for a Reynolds number between 3200 and 4600 and without any clear lifting peak. Conversely, the thin ellipse shows a first maximum of 1.22 at $Re = 1500$, suddenly reached from $Re = 1450$ where the lift value is around 0.9, and a second one near $Re = 8000$ where $\overline{C}_l \approx 1.36$. This behaviour is linked to the period bifurcations observed and discussed in section 9.4.4 and induced by a change in the topology of the wake field which becomes less compact.

Similarly, for the thin ellipse at $\alpha = 30°$ (series N5) bifurcations were also found and a lift increase was shown and discussed in Rossi et al. (2018).

For the thin ellipse at $\alpha = 20°$ (series N4), when the Reynolds number rises to 1700 (fig 9.14), a new change in the wake topology appears that leads to a straight periodic signal and to a drop in the mean lift. At $Re = 1800$ (fig 9.14), as discussed in 9.4.4, the lift signal change again and a new local maximum in the $\overline{C}_l$ is observed (bottom frame figure 9.30). In the chaotic regime of the thin ellipse, the lift assumes a growing trend up to $Re = 8000$, where a maximum is attained. At the present stage, a final explanation of the $\overline{C}_l$ behaviour within the chaotic regime is still lacking and should be further investigated.

In the case of the thick ellipse, top frame of figure 9.30, the trend is more flat and not evident changes in the global behaviour are found in the passage from periodic to chaotic regime. Furthermore, a little drop is observed at $Re = 4700$ although it is not clearly related to a wake change. It is worth to underline that for the thick ellipse, the error bars representing the Root Mean Square (RMS) of the time signal are rather wide, both in the periodic and chaotic regime regions, compared to the thin case. For the thin ellipse, the variance of the signal is more confined in the periodic region, whereas it increases in the chaotic one, as expected. Conversely, the thick ellipse, being more similar to a blunt body, experiences larger amplitudes in the lift signal, this implying more intense load vibrations induced by the shedding.

More clear is the behaviour of the lift with respect to the angle of attack, coming from series N6 and N7 and depicted in figure 9.31, leaving the airfoil shape unaltered ($b/a = 0.1$). At $Re = 2000$ (left frame, related to series N6) the lift grows until a maximum is attained at 15°, after which the separation moves to the leading edge and the profile becomes fully stalled. At this point, the lift manifests a little drop and starts to grow again almost up to 45°, where the drag overcomes the

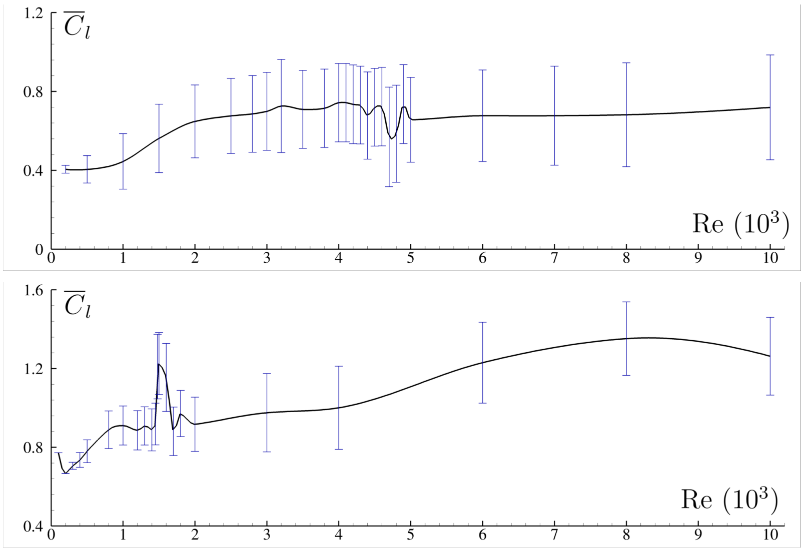

Figure 9.30: Mean lift coefficient behaviour with the Reynolds number for cases of series N2 (**top**) and N4 (**bottom**). With vertical lines the error bars related to the root mean square of the corresponding time signals.

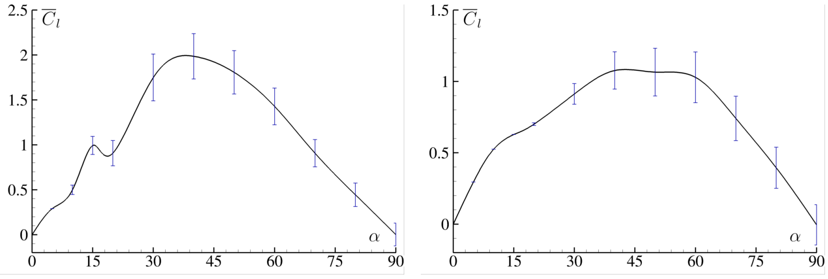

Figure 9.31: Mean lift coefficient behaviour with the angle of attack (in degrees) for cases of series N6 (Re=2000) (**left**) and N7 (Re=250) (**right**). The vertical lines are the error bars related to the root mean square of the corresponding time signals.

lift and the profile behaves actually as an obstacle within the flow field (see also Durante et al. (2020b)). After the maximum is reached, the lift decrease to zero (almost linearly) until $\alpha = 90°$.

For the lower Reynolds number case $Re = 250$ (series N7), the situation is significantly different. The lift trend is bell shaped with a linear behaviour up to 15°. The growing up to 45° is here moderate and the situation does not change evidently up to 60°, where it starts to lower as in the former case.

Concluding, a synoptic table indicating all the regimes found for all the Series investigated is reported in table 9.2.

9.7 COMPUTATIONAL COSTS

The total number of simulations performed for this work is 121 (see table 9.2). The number of vortex particles spans between 150,000 and 2,500,000 from the lowest Reynolds number up to the highest, while the number of time iteration ranges between 7000 to 70,000. The simulations used in this work have been all performed on 8 cluster nodes (2×18-core Intel Xeon E5-2697 v4 2.30GHz). The CPU costs of the implemented algorithm for 2D cases are about 100 μs per vortex particle and per time iteration on a single core. In order to perform the 121 simulations the time requested on the 8 cluster nodes was about 40 days. This cost is inline with other vortex particle solvers and it is grossly affected by the Fast Multipole Method.

N1	**0°**	**B/A=0.4**
Re		**REGIME**
200		Steady
500	***M***	Periodic
1000	***M***	Periodic
1500	***M***	Periodic
2000	***Q-P***	Periodic
2500	***NM***	Periodic
3000	***Q-P***	Periodic
4000	***Q-P***	Periodic
5000	***Q-P***	Periodic
6000	***Q-P***	Periodic
7000	***Q-P***	Periodic
8000	***Q-P***	Periodic
10000	***Q-P***	Periodic

N2	**20°**	**B/A=0.4**
Re		**REGIME**
100		Steady
200	***M***	Periodic
500	***NM***	Periodic
1000	***NM***	Periodic
1500	***NM***	Periodic
2000	***NM***	Periodic
2500	***NM***	Periodic
2800	***NM***	Periodic
3000	***NM***	Periodic
3200	***SH***	Periodic
3500	***SH***	Periodic
3800	***SH***	Periodic
4000	***SH***	Periodic
4100	***SH***	Periodic
4200	***SH***	Periodic
4300	***SH***	Periodic
4400		Chaotic
4500		Chaotic
4600		Chaotic
4700		Chaotic
4800		Chaotic
4900		Chaotic
5000		Chaotic
6000		Chaotic
7000		Chaotic
8000		Chaotic
10000		Chaotic

N3	**0°**	**B/A=0.1**
Re		**REGIME**
500		Steady
1000		Steady
2000		Steady
3000		Steady
4000		Steady
5000		Steady
6000		Steady
7000	***M***	Periodic
8000	***Q-P***	Periodic
10000	***Q-P***	Periodic

N4	**20°**	**B/A=0.1**
Re		**REGIME**
100		Steady
200	***M***	Periodic
300	***NM***	Periodic
400	***NM***	Periodic
500	***NM***	Periodic
800	***NM***	Periodic
1000	***NM***	Periodic
1200	***NM***	Periodic
1300	***NM***	Periodic
1400	***SH***	Periodic
1450	***SH***	Periodic
1480	***SH***	Periodic
1500	***SH***	Periodic
1600	***SH***	Periodic
1700	***SH***	Periodic
1800	***SH***	Periodic
2000		Chaotic
3000		Chaotic
4000		Chaotic
6000		Chaotic
8000		Chaotic
10000		Chaotic

N5	**30°**	**B/A=0.1**
Re		**REGIME**
100	***M***	Periodic
250	***NM***	Periodic
500	***NM***	Periodic
600	***NM***	Periodic
700	***NM***	Periodic
800	***NM***	Periodic
900	***NM***	Periodic
950	***SH***	Periodic
1000	***SH***	Periodic
1100	***SH***	Periodic
1200	***SH***	Periodic
1300		Chaotic
1400		Chaotic
1500		Chaotic
1550		Chaotic
1600		Chaotic
1650		Chaotic
1700		Chaotic
1800		Chaotic
1900		Chaotic
1400		Chaotic

N6	**Re=2000**	**B/A=0.1**
α		**REGIME**
0°		Steady
5°		Steady
10°	***M***	Periodic
15°	***NM***	Periodic
20°		Chaotic
30°		Chaotic
40°		Chaotic
50°		Chaotic
60°		Chaotic
70°		Chaotic
80°	***Q-P***	Periodic
90°	***Q-P***	Periodic

N7	**Re=250**	**B/A=0.1**
α		**REGIME**
0°		Steady
5°		Steady
10°		Steady
15°		Steady
20°	***M***	Periodic
30°	***NM***	Periodic
40°	***NM***	Periodic
50°	***NM***	Periodic
60°	***Q-P***	Periodic
70°	***NM***	Periodic
80°	***NM***	Periodic
90°	***NM***	Periodic

Table 9.2: Schematic diagram of regime transitions for the all the test series. Every regime is highlighted with a different color. The periodic regimes are specified as follows: M - monochromatic, NM - non-monochromatic, Q-P - quasi-periodic, SH - sub-harmonics.

10

CONCLUSION AND PERSPECTIVES

In the present work, the vortex particle method Diffused Vortex Hydrodynamics (DVH) method developed in Rossi et al. (2015a) has been described, numerically investigated and applied to a physical study.

The method was first carefully tested for planar flow around three geometries, with varying Reynolds number. All the test cases considered are unsteady and are all characterized by flow separation and shear layer formation in the wake.

For the first two geometries (a circle and an ellipse at incidence) the simulations correctly capture the separation point and the difficulties increase with the Reynolds number. The geometry for the third test case was instead a triangle and in this case, difficulties arise from the singularities on the boundary, that induce strong and very localized gradients.

For each test case, the flow was computed with different values for the Reynolds number. The accuracy of the method was studied based on derived quantities (forces) by systematic coarsening of the resolution and evaluating the error of the coarsening on the derived quantities. As a reference, the solution obtained with a fine resolution from the mesh-based solver was considered.

For the case of smooth boundaries, the investigation proved that convergence for the derived quantities is achieved for increasing Reynolds. Specifically the error evaluated on the evolution of the forces present a convergence rate of 2. For the last test case, where singularities on the boundary are present, the convergence rate was only 1. This can be attributed to the irregular boundary and also to the splitting algorithm that is first order in time.

The obtained results were validated against identical test cases computed with a completely different method, i.e. a Finite Volume (FV) approach and here the approach introduced in Broglia and Durante (2018) was used. The two methods differ because the DVH is based on a completely meshless Lagrangian discretization, whereas the FV is a mesh–based Eulerian approach. Moreover, DVH is based on the vorticity–velocity formulation of the Navier–Stokes equations, while the FV method uses the formulation in primitive variables (pressure–velocity).

Overall, the comparison of the results from the two methods allowed a satisfactory validation, because the solutions matched always very well, in terms of both local quantities and global forces. Some differences were observed only for the higher Reynolds numbers in the case of the flow past the triangle, in particular in terms of vortex positions in the far wake. This is can be attributed partly to the different resolution in the far wake and partly to the fact that the richer frequency content of the time histories for the forces reveals that the flow is moving toward a chaotic behavior, and therefore minimal differences in the time evolution can lead to visible differences between the solutions. Remarkably also the FVM shows a similar behaviour on the measured convergence rates with respect the DVH one.

After the verification of the method, an application to a physical study was presented, that of the flow past an elliptical cylinder at different Reynolds numbers, aspect ratio and angle of attack. Highly resolved simulations have been performed with the vortex method DVH permitting to carefully study the vorticity dynamics. The goal of this study was to investigate the impact of the variation of these parameters on the different regimes of the flow such as the steady, periodic and chaotic. It was indeed demonstrated that the variations of these parameters impact significantly on the dynamics of each regime.

In physical study we were interested in the transition from periodicity to chaos for the flow past an ellipse. This was studied using Fourier analysis as well as tools from classical dynamical systems such as the phase–space maps, the Poincaré maps and the maximum Lyapunov exponents. In this way it was made possible to obtain also bifurcation sequences for all the different configurations.

Specifically, the onset of doubling period bifurcations was discovered and commented in terms of Fourier spectra, Poincarè sections and phase maps for the case of small aspect ratio (thin ellipse). In the thick case, this mechanism was shown to be less dramatic with the transition to chaos being not direct but taking place through direct *and* inverse routes. Furthermore, in some scenario, time bifurcations before the onset of the regime condition were found.

Different behaviors were documented, based on the analysis of the lift time series such as monochromatic, non-monochromatic, quasi-periodic and sub-harmonics. Significant differences between thin and thick ellipse chaotic regimes were documented and the presence of a "pink noise" behaviour of the lift time signal in the thin case was discovered.

Another important aspect of the present analysis has been the investigation in terms of the vorticity flow fields and it has been connected to the time behaviour of the lift force, where meaningful.

The present investigation maybe extended to the analysis at higher Reynolds numbers at different thickness and different angles of attack. Indeed, at Re of order 10^5 turbulent reattachment of the boundary layer is expected affecting drag and lift forces.

For future perspectives, regarding the numerical development, the extension of the DVH method to three-dimensional configurations is an on-going activity. The main differences arise in the potential flow solver and in the Fast Multiple Method algorithm which must be completely reformulated in a three dimensional framework. Moreover the method can be extended to treat free surface flows close to submerged bodies, by incorporating the presence of the free-surface through its evolution equations and discretize them with Lagrangian particles while another possibility is the extension to handle the presence of multi-component bodies.

From a computational point of view, the 3D extension requires the solver to be parallelized in a very efficient way in order to allow for large scalability on cluster machines with hundreds of millions of vortex particles in a reasonable machine time.

BIBLIOGRAPHY

Agishtein, M. E. and Migdal, A. A. (1989). Dynamics of vortex surfaces in three dimensions: Theory and simulations. *Physica D: Nonlinear Phenomena*, 40(1):91–118.

Appel, A. W. (1985). An efficient program for many-body simulation. *SIAM Journal on Scientific and Statistical Computing*, 6(1):85–103.

Ashurst, W. T. and Meiburg, E. (1988). Three-dimensional shear layers via vortex dynamics. *Journal of Fluid Mechanics*, 189:87–116.

Barba, L., Leonard, A., and Allen, C. (2003). Numerical investigations on the accuracy of vortex methods with and without remeshing. In *16th AIAA Computational Fluid Dynamics Conference*, page 3426.

Barba, L. A. (2007). Spectral-like accuracy in space of a meshless vortex method. In *Advances in Meshfree Techniques*, pages 187–197. Springer.

Barnes, J. and Hut, P. (1986). A hierarchical O (N logN) force-calculation algorithm. *Nature*, 324(6096):446.

Batchelor, G. K. (2000). *An introduction to fluid dynamics*. Cambridge university press.

Beale, J. T. and Majda, A. (1981). Rates of convergence for viscous splitting of the Navier-Stokes equations. *Mathematics of Computation*, 37(156):243–259.

Beale, J. T. and Majda, A. (1982a). Vortex methods. I. Convergence in three dimensions. *Mathematics of Computation*, 39(159):1–27.

Beale, J. T. and Majda, A. (1982b). Vortex methods. II: Higher order accuracy in two and three dimensions. *Mathematics of Computation*, 39(159):29–52.

Beale, J. T. and Majda, A. (1985). High order accurate vortex methods with explicit velocity kernels. *Journal of Computational Physics*, 58(2):188–208.

Benfatto, G. and Pulvirenti, M. (1986). Convergence of chorin-marsden product formula in the half-plane. *Communications in mathematical Physics*, 106(3):427–458.

Benson, M., Bellamy-Knights, P., Gerrard, J., and Gladwell, I. (1989). A viscous splitting algorithm applied to low Reynolds number flows round a circular cylinder. *Journal of Fluids and Structures*, 3(5):439–479.

Birkhoff, G. and Fisher, J. (1959). Do vortex sheets roll up? *Rendiconti del Circolo matematico di Palermo*, 8(1):77–90.

Broglia, R. and Durante, D. (2018). Accurate prediction of complex free surface flow around a high speed craft using a single-phase level set method. *Computational Mechanics*, 62(3):421–437.

Chiron, L., Marrone, S., Di Mascio, A., and Touzé, D. L. (2018). Coupled SPH–FV method with net vorticity and mass transfer. *Journal of Computational Physics*, 364:111–136.

Chorin, A. J. (1967). A numerical method for solving incompressible viscous flow problems. *Journal of Computational Physics*, 2(1):12–26.

Chorin, A. J. (1968). Numerical solution of the Navier-Stokes equations. *Mathematics of Computation*, 22(104):745–762.

Chorin, A. J. (1973). Numerical study of slightly viscous flow. *Journal of Fluid Mechanics*, 57(4):785–796.

Chorin, A. J. (1978). Vortex sheet approximation of boundary layers. *Journal of Computational Physics*, 27(3):428–442.

Chorin, A. J. and Marsden, J. E. (2013). *A Mathematical Introduction to Fluid Mechanics*. Springer Science & Business Media.

Christiansen, I. (1973). Numerical simulation of hydrodynamics by the method of point vortices. *Journal of Computational Physics*, 13(3):363 – 379.

Colagrossi, A., Bouscasse, B., Antuono, M., and Marrone, S. (2012). Particle packing algorithm for SPH schemes. *Computer Physics Communications*, 183(8):1641–1653.

Cottet, G. H. (1991). Particle-grid domain decomposition methods for the Navier-Stokes equations in exterior domains. *Lectures in Applied Mathematics*, 28:103–117.

Cottet, G. H. and Koumoutsakos, P. D. (2000). *Vortex methods: theory and practice*. Cambridge university press.

Durante, D., Giannopoulou, O., and Colagrossi, A. (2020a). Regimes identification of the viscous flow past an elliptic cylinder for reynolds number up to 10000. *Communications in Nonlinear Science and Numerical Simulation (submitted)*.

Durante, D., Rossi, E., and Colagrossi, A. (2020b). Bifurcations and chaos transition of the flow over an airfoil at low Reynolds number varying the angle of attack. *Communications in Nonlinear Science and Numerical Simulation*, page 105285.

Durante, D., Rossi, E., Colagrossi, A., and Graziani, G. (2017). Numerical simulations of the transition from laminar to chaotic behaviour of the planar vortex flow past a circular cylinder. *Communications in Nonlinear Science and Numerical Simulation*, 48:18–38.

Dynnikova, G. Y. (2004). The lagrangian approach to solving the time-dependent Navier-Stokes equations. In *Doklady Physics*, volume 49, pages 648–652. Springer.

Eldredge, J. D. (2007). Numerical simulation of the fluid dynamics of 2d rigid body motion with the vortex particle method. *Journal of Computational Physics*, 221(2):626–648.

Ferziger, J. H., Perić, M., and Street, R. L. (2002). *Computational methods for fluid dynamics*, volume 3. Springer.

Fishelov, D. (1990). A new vortex scheme for viscous flows. *Journal of Computational Physics*, 86(1):211 – 224.

Giannopoulou, O., Colagrossi, A., Mascio, A. D., and Mascia, C. (2019a). Chorin's approaches revisited: Vortex particle method vs finite volume method. *Engineering Analysis with Boundary Elements*, 106:371–388.

Giannopoulou, O., Durante, D., Colagrossi, A., and Mascia, C. (2019b). *Vorticity dynamics past an inclined elliptical cylinder at different re numbers: from periodic to chaotic solutions*, page 185–196. International Centre for Numerical Methods in Engineering (CIMNE).

Goldstein, S. (1948). On laminar boundary-layer flow near a position of separation. *The Quarterly Journal of Mechanics and Applied Mathematics*, 1(1):43–69.

Gotoh, H. and Khayyer, A. (2016). Current achievements and future perspectives for projection-based particle methods with applications in ocean engineering. *Journal of Ocean Engineering and Marine Energy*, 2(3):251–278.

Graziani, G. and Bassanini, P. (2002). Unsteady viscous flows about bodies: Vorticity release and forces. *Meccanica*, 37(3):283–303.

Greengard, C. (1985). The core spreading vortex method approximates the wrong equation. *Journal of Computational Physics*, 61(2):345 – 348.

Greengard, L. and Rokhlin, V. (1987). A fast algorithm for particle simulations. *Journal of Computational Physics*, 73(2):325–348.

Hald, O. H. (1979). Convergence of vortex methods for Euler's equations. II. *SIAM Journal on Numerical Analysis*, 16(5):726–755.

Hald, O. H. (1986). Convergence of a random method with creation of vorticity. *SIAM Journal on Scientific and Statistical Computing*, 7(4):1373–1386.

Hald, O. H. and Del Prete, V. M. (1978). Convergence of vortex methods for Euler's equations. *Mathematics of Computation*, 32(143):791–809.

Handel, P. H. and Chung, A. L. (1993). International conference on noise in physical systems and 1/f fluctuations (12th) held in St. Louis, Missouri on 16-20 August 1993. AIP conference proceedings 285.

Harlow, F. H. and Welch, J. E. (1965). Numerical calculation of time-dependent viscous incompressible flow of fluid with free surface. *The Physics of Fluids*, 8(12):2182–2189.

Hieber, S. E. and Koumoutsakos, P. (2005). A lagrangian particle level set method. *Journal of Computational Physics*, 210(1):342–367.

Jackson, C. (1987). A finite-element study of the onset of vortex shedding in flow past variously shaped bodies. *Journal of Fluid Mechanics*, 182:23–45.

Johnson, S. A., Thompson, M. C., and Hourigan, K. (2004). Predicted low frequency structures in the wake of elliptical cylinders. *European Journal of Mechanics-B/Fluids*, 23(1):229–239.

Kaneda, Y. (1990). A representation of the motion of a vortex sheet in a three-dimensional flow. *Physics of Fluids A: Fluid Dynamics*, 2(3):458–461.

Khayyer, A. and Gotoh, H. (2011). Enhancement of stability and accuracy of the moving particle semi-implicit method. *Journal of Computational Physics*, 230(8):3093–3118.

Koumoutsakos, P. D. (1993). *Direct numerical simulations of unsteady separated flows using vortex methods*. PhD thesis, California Institute of Technology.

Koumoutsakos, P. D., Cottet, G. H., and Rossinelli, D. (2008). Flow simulations using particles-bridging computer graphics and CFD. In *SIGGRAPH 2008-35th International Conference on Computer Graphics and Interactive Techniques*, pages 1–73. ACM.

Koumoutsakos, P. D. and Leonard, A. (1993). Improved boundary integral method for inviscid boundary condition applications. *AIAA Journal*, 31(2):401–404.

Koumoutsakos, P. D. and Leonard, A. (1995). High-resolution simulations of the flow around an impulsively started cylinder using vortex methods. *Journal of Fluid Mechanics*, 296:1–38.

Koumoutsakos, P. D., Leonard, A., and Pepin, F. (1994). Boundary conditions for viscous vortex methods. *Journal of Computational Physics*, 113(1):52–61.

Krasny, R. (1986a). Desingularization of periodic vortex sheet roll-up. *Journal of Computational Physics*, 65(2):292–313.

Krasny, R. (1986b). A study of singularity formation in a vortex sheet by the point-vortex approximation. *Journal of Fluid Mechanics*, 167:65–93.

Kress, R., Maz'ya, V., and Kozlov, V. (1989). *Linear integral equations*, volume 82. Springer.

Kurtulus, D. F. (2015). On the unsteady behavior of the flow around naca 0012 airfoil with steady external conditions at Re = 1000. *International Journal of Micro Air Vehicles*, 7(3):301–326.

Kurtulus, D. F. (2016). On the wake pattern of symmetric airfoils for different incidence angles at Re = 1000. *International Journal of Micro Air Vehicles*, 8(2):109–139.

Kuwahara, K. and Takami, H. (1973). Numerical studies of two-dimensional vortex motion by a system of point vortices. *Journal of the Physical Society of Japan*, 34(1):247–253.

Leonard, A. (1975). Numerical simulation of interacting three-dimensional vortex filaments. In *Proceedings of the Fourth International Conference on Numerical Methods in Fluid Dynamics*, pages 245–250. Springer.

Leonard, A. (1980). Vortex methods for flow simulation. *Journal of Computational Physics*, 37(3):289–335.

LeVeque, R. J. et al. (2002). *Finite volume methods for hyperbolic problems*, volume 31. Cambridge university press.

Majda, A. and Beale, J. (1982). Vortex methods II: Higher order accuracy in two and three dimensions. *Mathematics of Computation*, 39:29–52.

Marrone, S., Mascio, A. D., and Le Touzé, D. (2016). Coupling of smoothed particle hydrodynamics with finite volume method for free-surface flows. *Journal of Computational Physics*, 310:161–180.

Marshall, J. and Grant, J. (1996). Penetration of a blade into a vortex core: vorticity response and unsteady blade forces. *Journal of Fluid Mechanics*, 306:83–109.

Mas-Gallic, S. (1987). *Contribution à l'analyse numérique des méthodes particulaires*. PhD thesis, Paris 6.

Mas-Gallic, S. (2002). The diffusion velocity method: a deterministic way of moving the nodes for solving diffusion equations. *Transport Theory and Statistical Physics*, 31(4-6):595–605.

Mas-Gallic, S. and Raviart, P. (1987). A particle method for first-order symmetric systems. *Numerische Mathematik*, 51(3):323–352.

Mikhlin, S. G. (2014). *Integral equations: and their applications to certain problems in mechanics, mathematical physics and technology*. Elsevier.

Milinazzo, F. and Saffman, P. (1977). The calculation of large Reynolds number two-dimensional flow using discrete vortices with random walk. *Journal of Computational Physics*, 23(4):380–392.

Mimeau, C. and Mortazavi, I. (2021). A review of vortex methods and their applications: From creation to recent advances. *Fluids*, 6(2):68.

Monaghan, J. J. and Lattanzio, J. C. (1985). A refined particle method for astrophysical problems. *Astronomy and Astrophysics*, 149:135–143.

Morse, P. and Feshbach, H. (1953). *Methods of Theoretical Physics*. International series in pure and applied physics. McGraw-Hill.

Muscari, R., Dubbioso, G., and Di Mascio, A. (2017). Analysis of the flow field around a rudder in the wake of a simplified marine propeller. *Journal of Fluid Mechanics*, 814:547–569.

Mycek, P., Pinon, G., Germain, G., and Rivoalen, É. (2013). A self-regularising dvm–pse method for the modelling of diffusion in particle methods. *Comptes Rendus Mécanique*, 341(9-10):709–714.

Ogami, Y. (2000). A vortex method for heat-vortex interaction and fast summation technique. In *Vortex Methods*, pages 145–152. World Scientific.

Ogami, Y. and Akamatsu, T. (1991). Viscous flow simulation using the discrete vortex model—the diffusion velocity method. *Computers & Fluids*, 19(3):433 – 441.

Ould-Salihi, M. L., Cottet, G. H., and El Hamraoui, M. (2001). Blending finite-difference and vortex methods for incompressible flow computations. *SIAM Journal on Scientific Computing*, 22(5):1655–1674.

Palha, A., Manickathan, L., Ferreira, C. S., and van Bussel, G. (2015). A hybrid Eulerian-Lagrangian flow solver. *arXiv preprint arXiv:1505.03368*.

Park, J. K., Park, S. O., and Hyun, J. M. (1989). Flow regimes of unsteady laminar flow past a slender elliptic cylinder at incidence. *International Journal of Heat and Fluid Flow*, 10(4):311–317.

Pasquale, L., Durante, D., and Broglia, R. (2019). Flow separation prevention around a naca0012 profile through multivariable feedback controlled plasma actuators. *Computers & Fluids*, 182:85–107.

Perlman, M. (1985). On the accuracy of vortex methods. *Journal of Computational Physics*, 59(2):200–223.

Proudman, I. and Pearson, J. (1957). Expansions at small Reynolds numbers for the flow past a sphere and a circular cylinder. *Journal of Fluid Mechanics*, 2(3):237–262.

Pulliam, T. H. and Vastano, J. A. (1993). Transition to chaos in an open unforced 2d flow. *Journal of Computational Physics*, 105(1):133–149.

Ramachandran, P. (2004). Development and study of high resolution two dimensional random vortex method. *Doctor of philosophy thesis, Madras, Department of aerospace engineering Indian institute of technology*.

Ranucci, M. (1995). *Effetti del rilascio di vorticitá nell'interazione corpo-fluido*. PhD thesis, Ph. D. thesis, University of Rome "La Sapienza," Rome.

Rehbach, C. (1978). Numerical calculation of three-dimensional unsteady flows with vortex sheets. In *16th Aerospace Sciences Meeting*, page 111.

Riccardi, G. and Durante, D. (2007). *Elementi di fluidodinamica: Un'introduzione per l'Ingegneria*. Springer Science & Business Media.

Roache, P. J. (1997). Quantification of uncertainty in computational fluid dynamics. *Annual review of fluid Mechanics*, 29(1):123–160.

Rosenhead, L. (1931). The formation of vortices from a surface of discontinuity. *Proceedings of the Royal Society of London A*, 134(823):170–192.

Rossi, E. (2014). *2D-vorticity genesis and dynamics studied through particle methods*. PhD thesis, Citeseer.

Rossi, E., Colagrossi, A., Bouscasse, B., and Graziani, G. (2015a). The diffused vortex hydrodynamics method. *Communications in Computational Physics*, 18(2):351–379.

Rossi, E., Colagrossi, A., Durante, D., and Graziani, G. (2016). Simulating 2d viscous flow around geometries with vertices through the diffused vortex hydrodynamics method. *Computer Methods in Applied Mechanics and Engineering*, 302:147–169.

Rossi, E., Colagrossi, A., and Graziani, G. (2015b). Numerical Simulation of 2D-Vorticity Dynamics using Particle Methods. *Computers and Mathematics with Applications*, 69(12):1484–1503.

Rossi, E., Colagrossi, A., Oger, G., and LeTouzé, D. (2018). Multiple bifurcations of the flow over stalled airfoils when changing the Reynolds number. *Journal of Fluid Mechanics*, 846:356–391.

Rossi, L. F. (1996). Resurrecting core spreading vortex methods: A new scheme that is both deterministic and convergent. *SIAM Journal on Scientific Computing*, 17(2):370–397.

Rossinelli, D. and Koumoutsakos, P. (2008). Vortex methods for incompressible flow simulations on the GPU. *The Visual Computer*, 24(7-9):699–708.

Sakajo, T. (2001). Numerical computation of a three-dimensional vortex sheet in a swirl flow. *Fluid Dynamics Research*, 28(6):423.

Serra, M. and Haller, G. (2017). Forecasting long-lived lagrangian vortices from their objective Eulerian footprints. *Journal of Fluid Mechanics*, 813:436–457.

Serra, M., Vétel, J., and Haller, G. (2018). Exact theory of material spike formation in flow separation. *Journal of Fluid Mechanics*, 845:51–92.

Shankar, S. and Van Dommelen, L. (1996). A new diffusion procedure for vortex methods. *Journal of Computational Physics*, 127(1):88–109.

Shintani, K., Umemura, A., and Takano, A. (1983). Low-Reynolds-number flow past an elliptic cylinder. *Journal of Fluid Mechanics*, 136:277–289.

Soh, W. and Goodrich, J. W. (1988). Unsteady solution of incompressible Navier-Stokes equations. *Journal of Computational Physics*, 79(1):113–134.

Speck, R. (2011). *Generalized algebraic kernels and multipole expansions for massively parallel vortex particle methods*, volume 7. Forschungszentrum Jülich.

Temam, R. (1969). Approximation of the solution of the Navier- Stokes equations by the fractional step method(Approximate solution method for Navier-Stokes equations for incompressible viscous fluids). *Archive for Rational Mechanics and Analysis*, 32(2):135–153.

Van Dommelen, L. and Rundensteiner, E. A. (1989). Fast, adaptive summation of point forces in the two-dimensional poisson equation. *Journal of Computational Physics*, 83(1):126–147.

Wiener, N. (1964). *Time Series*. M.I.T. Press.

Wolf, A., Swift, J. B., Swinney, H. L., and Vastano, J. A. (1985). Determining lyapunov exponents from a time series. *Physica D: Nonlinear Phenomena*, 16(3):285–317.

Xu, R., Stansby, P., and Laurence, D. (2009). Accuracy and stability in incompressible SPH (ISPH) based on the projection method and a new approach. *Journal of Computational Physics*, 228(18):6703–6725.

Yokota, R., Sheel, T. K., and Obi, S. (2007). Calculation of isotropic turbulence using a pure lagrangian vortex method. *Journal of Computational Physics*, 226(2):1589–1606.

Zdravkovich, M. M. (1997). *Flow around circular cylinders: Fundamentals*, volume 1. Oxford university press.

Appendices

A

BOUNDARY CONDITION FOR THE DIFFUSION STEP

The splitting into convection and diffusion must provide an appropriate intermediate procedure for the generation of vorticity on the body boundary. This is done by replacing the boundary with a vorticity layer, a vortex sheet.

The introduction and subsequent diffusion of this sheet in the domain will change the total circulation, according to Kelvin's theorem. Assuming that the diffusion of the vortex sheet occurs in the time interval $[t,\ t + \Delta t_d\ ]$, the total circulation will then change according to:

$$\oint_{\partial\Omega_b} \gamma(s)\ ds = \int_t^{t+\Delta t} \frac{d\Gamma}{dt'}\ dt', \tag{A.1}$$

where s is the curvilinear coordinate on the body boundary.

The vortex sheet is directly connected to the flux of vorticity on the boundary. This is because in viscous flow the only way vorticity can enter the fluid is through the boundaries. Thus the variation of the total circulation in the field is equal to the flux of vorticity through the boundary. This can be seen as follows. Using the definition of the total circulation:

$$\int_\Omega \omega\ dV = \Gamma, \tag{A.2}$$

it is possible to write:

$$\frac{d}{dt}\int_\Omega \omega\ dV = \frac{d\Gamma}{dt}. \tag{A.3}$$

Using the vorticity equation:

$$\frac{\partial\omega}{\partial t} + \mathbf{u}\cdot\nabla\omega = \nu\nabla^2\omega, \tag{A.4}$$

leads to:

$$\begin{aligned}\frac{d}{dt}\int_\Omega \omega\ dV = \int_\Omega \frac{D\omega}{Dt}\ dV = \int_\Omega (\nu\nabla^2\omega)\ dV = \int_\Omega \nabla\cdot(\nu\nabla\omega)\ dV \\ = -\int_{\partial\Omega_b} \nu\nabla\omega\cdot\mathbf{n}\ dS = -\int_{\partial\Omega_b} \nu\frac{\partial\omega}{\partial n}\ dS. \end{aligned}\tag{A.5}$$

Using the relations above:

$$\frac{d\Gamma}{dt} = -\nu \oint_{\partial\Omega_b} \frac{\partial \omega}{\partial n}\, ds. \tag{A.6}$$

Substituting in (A.1):

$$\oint_{\partial\Omega_b} \gamma(s)\, ds = \int_t^{t+\Delta t} \left[-\nu \oint_{\partial\Omega_b} \frac{\partial \omega}{\partial n}\, ds \right] dt = -\oint_{\partial\Omega_b} \left[\int_t^{t+\Delta t} \nu \frac{\partial \omega}{\partial n}\, dt \right] ds, \tag{A.7}$$

from which the following expression is derived:

$$\gamma(s) = -\int_t^{t+\Delta t} \nu \frac{\partial \omega}{\partial n}\, dt. \tag{A.8}$$

Assuming that the vorticity flow is constant during the time interval Δt:

$$\nu \frac{\partial \omega}{\partial n}(s) = -\frac{\gamma(s)}{\Delta t_d}, \tag{A.9}$$

which expresses the vorticity flux on the wall in terms of the density circulation γ within the time interval Δt_d, corresponding to the diffusion time step and constitutes the Neumann boundary condition for the diffusion sub-step.